

THESIS
2
2009

**LIBRARY
Michigan State
University**

This is to certify that the
dissertation entitled

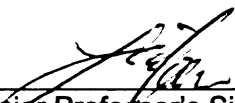
Fabrication of Nanostructures and Nanostructure based
Interfaces for Biosensor Application

presented by

Devsh Srivastava

has been accepted towards fulfillment
of the requirements for the

Doctoral degree in Materials Science



Major Professor's Signature

10/13/08

Date

MSU is an Affirmative Action/Equal Opportunity Employer

PLACE IN RETURN BOX to remove this checkout from your record.
TO AVOID FINES return on or before date due.
MAY BE RECALLED with earlier due date if requested.

DATE DUE	DATE DUE	DATE DUE

**FABRICATION OF NANOSTRUCTURES AND NANOSTRUCTURE BASED
INTERFACES FOR BIOSENSOR APPLICATION**

By

Devesh Srivastava

A DISSERTATION

**Submitted to
Michigan State University
in partial fulfillment of the requirements
for the degree of**

DOCTOR OF PHILOSOPHY

Materials Science

2008

ABSTRACT

FABRICATION OF NANOSTRUCTURES AND NANOSTRUCTURE BASED INTERFACES FOR BIOSENSOR APPLICATION

By

Devesh Srivastava

Nanoparticles have applications from electronics, composites, drug-delivery, imaging and sensors etc. Fabricating and controlling shape and size of nanoparticles and also controlling the positioning of these particles in 1, 2 or 3-d structures is of most interest. The underlying theme of this study is to develop simple and efficient techniques to fabricate nanoparticles from polymers, and also achieve control in shape, size and functionalization of nanoparticles, while applying them in biosensor applications. First part of the dissertation studies the fabrication of nanostructures using anodized alumina membrane as template. It discusses the fabrication design for injecting polystyrene nanoparticles inside the pores of anodized alumina membranes and heating the membrane to coalesce the particles into tapered nanoparticles. Various parameters like temperature and amount of injected particles can vary the size and shape of fabricated nanoparticles. Later it focuses on the fabrication of metallic nanostructures using the alumina membranes without the aid of the injection system. It utilizes the difference in the functionality of the pore edges of cleaved alumina membrane with respect to the pore walls to first deposit charged polymers using layer-by-layer deposition followed by deposition of nickel. Second part of this study involves immobilization of enzymes for biosensor applications. It describes a biosensor interface developed by immobilization of tyrosinase using layer-by-layer (LBL) deposition process. The interface was modified with functional nanoparticles and their influence on the response of biosensor was

studied. Tyrosinase sensor was further extended to develop a novel biosensor which was used to study real time inhibition of NEST, a subunit of the medically relevant membrane protein, neuropathy target esterase. The biosensor was developed to give real time monitoring of dose dependent decrease in activity of NEST. Final part of this study emphasizes on the influence of high shear rate mixer from PRIMIX, Japan on polymer particle formation. This mixer can process specific volume of liquid and subject it to high shear conditions. The mixing geometry consists of concentric cylinders, 52 mm inner turbine diameter and 58 mm vessel diameter, with inner turbine rotating at high peripheral speeds ranging from 10 m/s to 50m/s. The mixing is in turbulent regime at all the speeds. Poly-lactic acid (PLA) nanoparticles were fabricated by nanoprecipitation and emulsion diffusion process. Nanoprecipitation process was independent of shear rate at low mixing speeds and particle size went up at high speeds due to coalescence of PLA particles. Emulsion diffusion was done by making oil in water emulsion. PLA dissolved in ethyl acetate was used as oil phase. It was followed by diffusion of ethyl acetate in excess amount of DI water. It followed expected trend of smaller size at high mixing speeds but was very sensitive to mixing time where particles coalesced at longer time duration. The influence of viscosity was also studied and particles changed shape from spherical nanoparticles to micron sized open shells at high viscosity and high mixing speeds due to heating combined with mixing occurring in viscous turbulent regime.

COPYRIGHT BY

DEVESH SRIVASTAVA

2008

Dedicated To My Parents and Family

Acknowledgments

First of all, I would like to thank my advisor, Dr. Ilsoon Lee, who guided and mentored me throughout the duration of my stay at Michigan State University. He provided useful insights and tips and encouraged me to come up with new ideas. He also provided me plenty of opportunities to travel and present my work in a professional set-up. It was a pleasure working with him for my PhD.

I would also like to thank my committee members, especially Dr. Worden and Dr. Ofoli for their guidance and comments during the course of my PhD especially during the meetings for CNBI. Also like to thank Dr. Worden for letting me have uninterrupted use of facilities in Protein Expression Laboratory. I would also like to thank Dr. Blanchard and Dr. Hogan for agreeing to reside on my committee and mentoring and supporting me through the course of my dissertation.

I would also like to thank PRIMIX Corporation, Japan for providing our lab with the high shear rate mixer which led me conduct the final part of my research. Also like to thank them for the initial training and continuous help throughout the time period. I would also like to thank staff at the Center of Advanced Microscopy for helping me work on microscopes especially Ewa who was more than helpful while I worked on SEM.

Last but not the least, all the lab members of Nanobiotechnology Lab and friends that I made during my stay at Michigan State. I would like to thank Neeraj Kohli for the work we did together and his help initially in the lab. I would also like to thank Sachin and Sumit for helping me in the lab and all the fun time we had outside. I would also extend my thanks to Aaron, Troy, and Srivatsan. Also my roommates Deep C, Deep B

and Ajay over the years and my friends Karuna, Shishir, Tithi, Shreya, Tanmay, Amit, Leena, Sutti for making my 4 years of stay a truly unforgettable one.

Finally I would like to thank my family back home in India and my wife, Ankita. They were constant source of encouragement and wishes which helped me immensely throughout the course of my thesis.

TABLE OF CONTENTS

LIST OF TABLES.....	xi
LIST OF FIGURES.....	xii
ABBREVIATIONS.....	xix
SYMBOLS.....	xxi
1 INTRODUCTION.....	1
1.1 OVERVIEW OF NANOTECHNOLOGY.....	1
1.2 FABRICATION OF NANOSTRUCTURES USING NOVEL NANOINJECTION PROCESS.....	5
1.3 STEP-EDGE LIKE TEMPLATED FABRICATION OF NICKEL NANOWIRES.....	6
1.4 HIGH SENSITIVITY TYROSINASE BIOSENSOR USING LBL DEPOSITION.....	6
1.5 NEUROPATHY TARGET ESTERASE BIOSENSOR.....	7
1.6 FABRICATION OF POLY-LACTIC ACID NANOPARTICLES USING HIGH SHEAR RATE NANOMIXER.....	8
2 FABRICATION OF NANOSTRUCTURES USING NOVEL NANOINJECTION PROCESS.....	11
2.1 INTRODUCTION.....	11
2.2 EXPERIMENTAL SECTION.....	13
2.2.1 Materials.....	13
2.2.2 Experimental Details.....	14
2.3 RESULTS AND DISCUSSIONS.....	17
2.4 CONCLUSIONS AND FUTURE WORK.....	26
3 STEP-EDGE LIKE TEMPLATED FABRICATION OF NICKEL NANOWIRES.....	27
3.1 INTRODUCTION.....	27
3.2 EXPERIMENTAL SECTION.....	28
3.3 RESULTS AND DISCUSSIONS.....	31
3.4 CONCLUSIONS AND FUTURE WORK.....	40
4 HIGH SENSITIVITY TYROSINASE BIOSENSOR USING LBL DEPOSITION.....	41
4.1 INTRODUCTION.....	41
4.2 EXPERIMENTAL SECTION.....	44
4.2.1 Materials.....	44
4.2.2 Preparation of Au Nanoparticles.....	44
4.2.3 Modification of multiwalled carbon nanotubes.....	44
4.2.4 Enzyme loading onto gold slides and silver membranes.....	45
4.2.5 Amperometric i-t curves.....	46
4.2.6 Cyclic Voltammetry.....	47

4.2.4	Enzyme loading onto gold slides and silver membranes.....	45
4.2.5	Amperometric i-t curves	46
4.2.6	Cyclic Voltammetry	47
4.2.7	UV-vis absorbance spectroscopy.....	47
4.2.8	Microscopy	47
4.3	RESULTS AND DISCUSSIONS	50
4.3.1	Layer-by-Layer of Poly-L-Lysine and Tyrosinase.....	50
4.3.2	Incorporation of Multiwalled Carbon Nanotubes.....	52
4.3.3	Silver membrane as electrode.....	57
4.4	CONCLUSIONS AND FUTURE WORK.....	65
5	NEUROPATHY TARGET ESTERASE BIOSENSOR	66
5.1	INTRODUCTION	66
5.2	EXPERIMENTAL SECTION.....	68
5.2.1	Materials	68
5.2.2	NEST expression and purification.....	68
5.2.3	Preparation of gold electrode for NEST biosensor.....	69
5.2.4	Preparation of phenyl valerate solution	71
5.2.5	Ellipsometry.....	71
5.2.6	Potential step voltammetry and other measurements	72
5.3	RESULTS AND DISCUSSION.....	72
5.3.1	Ellipsometry.....	72
5.3.2	Dependence of current response on working potential and pH.....	73
5.3.3	Measurement of esterase activity using NEST biosensor	75
5.3.4	Inhibition of esterase activity	78
5.3.5	Higher sensitivity NEST biosensor	82
5.3.6	Significance of NEST biosensor.....	86
5.4	CONCLUSIONS AND FUTURE WORK.....	87
6	FABRICATION OF POLY-LACTIC ACID PARTICLES USING A HIGH SHEAR RATE.....	88
6.1	INTRODUCTION	88
6.2	THEORETICAL BACKGROUND	91
6.2.1	Nanoprecipitation	91
6.2.2	Emulsion Diffusion.....	92
6.3	EXPERIMENTAL SECTION.....	98
6.3.1	Materials	98
6.3.2	Experimental Details	98
6.3.3	Dynamic Light Scattering (DLS)	99
6.3.4	Microscopy	99
6.3.5	UV-vis absorbance spectroscopy.....	99
6.3.6	Zeta Potential.....	100
6.3.7	Differential Scanning Calorimetry	100
6.3.8	Thermogravimetric Analysis	100
6.4	RESULTS AND DISCUSSION.....	100
6.4.1	Nanoprecipitation	100

6.4.2	Emulsion Diffusion.....	108
6.4.3	Effect of addition of glycerol.....	124
6.5	EFFECT OF ELECTRON BEAM ON PLA PARTICLES.....	138
6.5.1	Poly-Lactic Acid and Beam Damage	138
6.5.2	Deformation of PLA Particles By Electron Beam.....	139
6.5.3	Effect Of Gold Coating On The Poly-Lactic Acid Deformation.....	143
6.5.4	Effect Of Structure Of Poly-Lactic Acid On Deformation.....	149
6.6	CONCLUSIONS AND FUTURE WORK.....	153
7	REFERENCES.....	155

LIST OF TABLES

<i>Table 3.1</i>	30
<i>Table 4.1 Zeta potential of polyelectrolyte coated multiwalled carbon nanotubes</i>	53
<i>Table 6.1 Effect of surfactant type on the surface charge and surface potential on nanoparticles formed.</i>	104
<i>Table 6.2 Beam penetration depth for PLA and gold as a function of accelerating voltage.</i>	143
<i>Table 6.3 Fraction of beam transmitted at different gold film thicknesses</i>	144

LIST OF FIGURES

Images in this dissertation are presented in color

- Figure 2.1: A system of solvent-aided nano-injection of nanospheres.....14
- Figure 2.2: Schematic illustration of solvent-aided nano-injection molding process using alumina membranes having cylindrical nanopores.16
- Figure 2.3: SEM images of novel tapered nanorods. A) Nanorice (small aspect-ratio (~2) tapered nanorods). B) Higher magnification image of Nanorice. C) Nanospears made of PS nanospheres (aspect ratio ~10). D) Nanospear bundles formed by pumping 50 nm PS particles into a single membrane that has 20 nm and 200 nm pore sizes at either ends. The nanospheres were pumped into 200 nm pore side. ...19
- Figure 2.4: Schematic representation of tapered nanorods and nanospears forming due to partial wetting of alumina by polystyrene.20
- Figure 2.5: SEM images of incomplete nanorods using nanospheres. A) Incomplete nanotubes were observed after sintering of 140 nm PS nanoparticles inside a 200 nm pore size membranes. B) A half open nanotube formed inside a 200 nm pore size membrane. C) A small aspect ratio nanotube. D) Broken nano-doughnuts using 140 nm particles in a single 200-20 nm pore size membrane. E) Nanodiscs formed using 100 nm PS spheres in a single 200-20 nm membrane without ultrasonication. F) An intermediate structure with incomplete melting of the polymer nanospheres.....21
- Figure 2.6: Energy dispersive spectrum (EDS) of fabricated nanoparticles is shown above. The black spectrum is the background and the line is the spectrum of the fabricated nanoparticles. The difference in the count of carbon content shows the presence polystyrene which is composed of carbon and rest of the elements do not show any increase.....23
- Figure 2.7: SEM image of epoxy nanotubes prepared using A) and B) 200 nm & C) and D) 100 nm pore sized alumina membranes.24
- Figure 2.8: Cross sectional SEM of alumina membrane. Its pores are decorated with the gold nanoparticles.....25
- Figure 3.1: A) Schematic representation of the template formation process including top and side views of alumina membranes before and after the cleavage. A side view SEM image after the fluorosilane treatment and cleavage is shown, the scale bar is 500nm. The actual membranes have quasi-hexagonally packed nanopores, but hexagonally packed nanopores were assumed for the determination of the cleaved edges in which nickel nanowires grow. B) Schematic illustration of each step of the nanowire formation process, deposition of PEM layers selectively on the freshly cleaved hydrophilic edge area and then selective nickel deposition followed.32

Figure 3.2: of nickel nanowires after dissolution of alumina membrane. C) Fuzzy nanostructure showing polyelectrolyte base as support for nickel growth. D) A nickel nanowire with spreading ends showing possible deposition of polyelectrolytes on the top surface of alumina membranes.	35
Figure 3.3: Rate of nickel deposition determined from Quartz crystal microbalance.....	36
Figure 3.4: SEM image showing the two regions where EDS spectra were obtained, on the sample and on the background. The sample spectrum as shown in next page has nickel and carbon peaks, showing presence of nickel from electroless deposition and carbon as polyelectrolytes, which were absent in background spectrum (continued).	38
Figure 3.4 continued: Spectrum of nickel nanowires and background. Ni peak are visible in sample but are absent in background spectrum.....	39
Figure 4.1: Different architectures for catechol sensor: (a) Thioctic acid modified gold electrode and layer-by-layer (LBL) deposition of tyrosinase and poly-lysine, (b) same as (a) but functionalized multiwalled carbon nanotubes instead of poly-lysine (continued).....	48
Figure 4.1: (c) Polymer nanospars drop coated and cross-linked onto cystamine modified electrode and then a layer of tyrosinase adsorbed over it, and (d) Scanning electron micrograph of silver membranes used for tyrosinase and poly-lysine deposition using LBL deposition.....	49
Figure 4.2: Tyrosinase biosensor for catechol as substrate, the electrode was maintained at -0.1V vs Ag/AgCl as reference electrode. Each step is aliquot of catechol added to achieve final concentration of 8 μ M in bulk.	50
Figure 4.3: Bilayer versus Current sensitivity plot for PLL-Tyr biosensor. The sensitivity with different number of bilayers increased till 6 bilayers and then dropped and stabilized.....	51
Figure 4.4: FTIR spectra after each layer: 1665 cm^{-1} (C=O stretching of amide group), 1540 cm^{-1} for N-H bending mode and 3300 cm^{-1} for N-H stretching mode.....	52
Figure 4.5 a) TEM of pure multiwalled carbon nanotube and b) polyelectrolyte coated MWCNTs.	54
Figure 4.6: Comparative plot of sensitivity for PLL coated MWCNTs and pure PLL tyrosinase LBL system.	55
Figure 4.7: (a) Comparative response curve for 3 bilayers of PDAC coated MWCNTs/Tyrosinase and pure PDAC/Tyrosinase (Control) system, the difference in sensitivity was significant, (b) SEM image of LBL fMWCNTs on electrode.	56

Figure 4.8: (a) Cyclic voltammogram of a silver planar as a control electrode and porous silver membrane as electrode in 0.5M Na ₂ SO ₄ purged with nitrogen at scan rate of 100 mV/s from -0.35V to +0.15V. (b) Amount of equivalent active enzyme loading on planar electrodes per unit area until 8 bilayers and on porous silver membrane. The amount of enzyme increased as number of bilayers increased.	59
Figure 4.9: Comparative response curve for 6 Bilayer PLL-Tyr and catechol biosensor on porous silver membrane.....	61
Figure 4.10: Comparative sensitivity plot for different architectures.	61
Figure 4.11: (a) Diffusion of quinone (P) through the enzyme layer on a planar electrode. The distance for quinone to diffuse to the electrode surface is much larger. (b) As compared to the other electrode, which has higher enzyme loading due the higher surface area while keeping the diffusion distance small (b).....	62
Figure 4.12: Sensitivity plots for a) 6 bilayers of PLL-Tyr on planar gold and b) 1 layer of PLL-Tyr on porous silver electrode.....	64
Figure 5.1: Molecular architecture of NEST biosensor.....	71
Figure 5.2: Ellipsometric thicknesses after the successive addition of following layers: thioctic acid (point a), PLL-Tyr first bilayer (point b), PLL-Tyr second bilayer (point c), PLL-Tyr third bilayer (point d), and PLL and NEST final bilayer (point e).....	73
Figure 5.3: (a) Effect of working potential on the response current of the enzyme electrode in 0.1 M phosphate buffer (pH 7.0) with (i) and without (ii) 12 μM phenyl valerate solution, in 0.1 M phosphate buffer at an applied potential of -0.1 V (vs Ag/AgCl). (b) Effect of pH on the response current of the electrode, in the presence of 12 μM phenyl valerate solution, in 0.1 M phosphate buffer at an applied potential of -0.1V (vs Ag/AgCl).....	74
Figure 5.4: (a) Current time response of the NEST biosensor to the addition of aliquots of 4 μM phenyl valerate, in 0.1 M phosphate buffer, pH 7.0, at an applied potential of -0.1V (vs Ag/AgCl). (b) Calibration plot.....	76
Figure 5.5: Control experiment: Current time response on an electrode containing only tyrosinase. The electrode was assembled in exactly the same way as NEST biosensor, except that the final NEST layer was not deposited.....	77
Figure 5.6: Current time response of NEST biosensor to the addition of phenyl valerate in phosphate buffer (0.1 M, pH 7.0) to obtain a final phenyl valerate concentration of 8 μM followed by the addition of NEST inhibitor PMSF to obtain a final PMSF concentration of 10 μM.	79
Figure 5.7: Current time response of NEST biosensor to the addition of phenyl valerate in phosphate buffer (0.1 M, pH 7.0) to obtain a final phenyl valerate concentration of 8	

μM followed by the addition of NEST inhibitor PMSF to obtain a final PMSF concentration of 100 μM	80
Figure 5.8: Current time response of NEST biosensor to the addition of phenyl valerate in phosphate buffer (0.1 M , pH 7.0) to obtain a final phenyl valerate concentration of 8 μM followed by the addition of NEST inhibitor PMSF to obtain a final PMSF concentration of 1000 μM	81
Figure 5.9: Current time response of NEST biosensor with 6 bilayers of PLL-Tyr underneath the NEST layer. The sensor was tested in phosphate buffer (0.1M) with electrode maintained -0.1V vs Ag/AgCl reference electrode. In control the electrode was prepared in exactly the same manner but NEST layer was not added.	83
Figure 5.10: Current response of NEST biosensor with 6 layers of PLL-Tyr and followed by inhibition of NEST by addition of 0.1 mM PMSF. First phenyl valerate was added to get the final concentration of 8 μM in bulk solution. The current response was allowed to achieve steady state before addition of an aliquot of PMSF to get final concentration of 0.1 mM.	84
Figure 5.11: Current response of NEST biosensor with 6 layers of PLL-Tyr and followed by inhibition of NEST by addition of 1 mM PMSF. First phenyl valerate was added to get the final concentration of 8 μM in bulk solution. The current response was allowed to achieve steady state before addition of aliquot of PMSF to get final concentration of 1 mM.	85
Figure 6.1: (a) Schematic of mixing chamber of the nanomixer. It has cylindrical turbine which rotates at peripheral speed of 10m/s to 50m/s. (b) A cross-sectional cartoon, it can have one or two injection port with continuous processing.	90
Figure 6.2: Turbine peripheral speed and equivalent Reynolds number for Couette-Taylor geometry flow.	91
Figure 6.3: Emulsification is carried out in the nanomixer by adding water with surfactant and polymer in oil (solvent). This was followed by diffusion step in which emulsion was added to excess amount of water for solvent phase to diffuse out.	93
Figure 6.4: (a) Rate of energy dissipation as a function of peripheral speed and (b) Plot of eddy diameter, λ and droplet diameter for inertial turbulent regime d_{KH} , for each mixing speed assuming ethyl acetate and water system.	97
Figure 6.5: SEM image of PLA particles prepared at 50m/s mixing speed.	101
Figure 6.6: As can be seen in the SEM image the larger particles are heated above glass transition temperature and colliding and coalescing into larger particles.	102
Figure 6.7: Zeta potential of PLA particles (a) CTAB as surfactant; (b) Pluronic F68 as surfactant; as a function of varying ionic strength in DI water. Increasing the ionic strength decreases the zeta potential of the particles.	105

Figure 6.8: Mean particle size of PLA particles with Pluronic F68 and CTAB as surfactant. It also shows the temperature in the vessel at each mixing speed.	106
Figure 6.9: Decrease in the peak intensity at 540 nm after mixing gold nanoparticles inside the nanomixer.....	107
Figure 6.10: It shows the signature shift in the peak intensity from 540nm to 700 nm after agglomeration of gold nanoparticles.	107
Figure 6.11: Mean particle size as obtained by dynamic light scattering for particles prepared at different mixing speeds in Nanomixer.	110
Figure 6.12: Emulsions were made at different speeds and then added to excess amount of water for particle formation.....	110
Figure 6.13: Scanning electron micrographs at 7500X of PLA nanoparticles obtained by emulsifying a) 10 m/s and b) 20m/s for 10 minutes.	112
Figure 6.14: Higher magnification (15000X)scanning electron micrographs of PLA nanoparticles obtained by emulsifying a) 10 m/s and b) 20m/s for 10 minutes. Illustrates PLA particles at 10m/s are more polydisperse than particles at 20m/s. .	113
Figure 6.15: Scanning electron micrographs (15000X) of PLA nanoparticles obtained by emulsifying at a) 30 m/s for 10 minutes and b) 40m/s for 2 minutes.....	115
Figure 6.16: Scanning electron micrographs (65000X) of PLA nanoparticles obtained by emulsifying a) 30 m/s for 10 minutes and b) 40m/s for 2 minutes.....	116
Figure 6.17: TEM (a) and SEM image (b) of PLA nanoparticles obtained by emulsifying at 50m/s for 1 minute.....	117
Figure 6.18: Mean diameter of the particles as obtained from DLS and as calculated from SEM images.....	118
Figure 6.19: The particle sizes can be divided into two categories as large and small. The mean diameter of each categories is plotted at mixing speeds of 10m/s to 30m/s..	119
Figure 6.20: The mean diameter of particles at the different mixing times. Hollow legends are used to mark the large particle diameter and small particle diameter as observed in SEM images.	121
Figure 6.21: Illustrates the fluid motion inside the mixer and how emulsion droplet can encounter different turbulent conditions giving rise to difference in stable droplet size.	121
Figure 6.22: a) Optical image of fluorescent particles: PLA emulsion prepared at 50m/s for 1 minute followed by addition of 1 micron fluorescently tagged pure polystyrene particles and further mixing for 2 minutes at 50m/s. b) Pure 1 micron fluorescently	

tagged pure polystyrene particles mixed at 50m/s for 2 minutes. The length of scale bar in both the images is 20 μm	123
Figure 6.23 :The mean particle size as a function of glycerol volume fraction at mixing speed of 50 m/s.	124
Figure 6.24: The above figure illustrates how the eddy diameter increases and is greater than both d_{KH} and d_{KV} at glycerol volume percentage greater than 35%. The mean diameter of particles for emulsion prepared at 50m/s for 1 minute also increased beyond 40%.	126
Figure 6.25: Mean particle size as a function of glycerol percentage. The mixing time at 50% glycerol was brought down to 20 seconds to avoid heating of the emulsion to 78 $^{\circ}\text{C}$	127
Figure 6.26: Effect of time on the particle size and shape at 50% glycerol at 50m/s mixing speed. Particles changed from solid nanospheres to micron sized hollow hemispherical shells.....	128
Figure 6.27: a) SEM image of particles formed at 40% glycerol when the internal temperature was raised to 78 $^{\circ}\text{C}$. b) Particles formed by adding emulsion prepared at 20m/s for 10 minutes to water/glycerol (50% v/v) mixed in a beaker at 78 $^{\circ}\text{C}$	130
Figure 6.28: a. TEM image of PLA nanoparticles showing that the particles are not hollow. b) Illustrating the mixing condition in inertial and viscous turbulent regimes, in inertial turbulent regime droplets are outside eddies and in viscous turbulent regime they are trapped inside the eddies.....	131
Figure 6.29: Scheme of the fabrication of bowl-shaped polymer particles in a turbulent eddy. At a short mixing time emulsion droplets caught in an eddy. Flow induced self-assembly of nanoparticles in an eddy. (B) At a long mixing time, emulsion droplets start coalescing in an eddy. (C) Solid form after loss of solvent. (D) Bowl shaped polymer particle.....	133
Figure 6.30: Scanning electron micrograph of poly-lactic acid open shells obtained by mixing at 40m/s at 60% glycerol by volume for 4 minutes.....	134
Figure 6.31: Effect of mixing speed on particle size at 50% glycerol volume percent. At all the speeds it is in viscous turbulent regime and the droplet size achieves a stable size at 30m/s. The mean particle size also reached minima at 30m/s and slightly increased at 50m/s.	135
Figure 6.32: TEM images of PLA nanoparticles prepared at 30 m/s with 50% glycerol. A) Shows the particles images with relatively larger particles. B) PLA nanoparticles with mean diameter around 30 nm. The scale bar in both the images is 100 nm....	137
Figure 6.33. Polylactic acid (a) before and (b) after exposure to 10KeV electron beam.	140

Figure 6.34: The effect electron beam damage on PLA film dried on a glass slide coated with 7 nm gold film. (a) and (b) is an image of PLA film before damage and (c) and (d) are the images of same area after electron beam damage. The length of scale bar in each image is 5 μm 142

Figure 6.35: SEM image of PLA particles coated with 7 nm of gold film (a) before damage and (b) after damage by 10KeV electron beam..... 145

Figure 6.36: SEM image of PLA particles coated with 35 nm of gold film (a) before damage and (b) after damage by 10KeV electron beam. 146

Figure 6.37: SEM image of PLA particles coated with 70 nm of gold film (a) before damage and (b) after damage by 10KeV electron beam. 147

Figure 6.38: a) Illustrates how beam damage is reduced with increasing thickness of gold film over polylactic acid particle. b) Illustrates the shrinking of particles during electron beam damage. 148

Figure 6.39: DSC curves for poly-lactic acid: a) Crystalline and b) Amorphous. 150

Figure 6.40: SEM images of PLLA particles coated with 7 nm of gold film a) before and b) after damage. 151

Figure 6.41: Thermogravimetric Analysis of crystalline and amorphous poly-lactic acid revealed that there was not significant mass loss in the PLA particles fabricated in the nanomixer and the shape change is due to the beam damage caused by the electron beam..... 152

ABBREVIATIONS

AFM: Atomic Force Microscopy

AuNPs: Gold Nanoparticles

CHAPS: 3-[(3-cholamidopropyl) dimethylammonio]-1-propanesulfonate

CNTs: Carbon Nanotubes

CTAB: Cetyl Trimethylammonium Bromide

Cys: Cystamine

DI: De-ionized

DLS: Dynamic Light Scattering

DMAB: Dimethylamine Borane

DMF: Dimethylformamide

DSC: Differential Scanning Calorimetry

EDS: Energy Dispersive X-ray Spectroscopy

fMWCNTs: Functionalized Multi-Walled Carbon Nanotubes

FTIR: Fourier Transform Infra-Red Spectroscopy

IPTG: Isopropyl Thiogalactoside

LB: Langmuir Blodgett

LBL: Layer-by-Layer

MWCNTs: Multi-Walled Carbon Nanotubes

NTE: Neuropathy Target Esterase

OPs: Organophosphorus Esters

OPIDNs: (OP)-induced delayed neuropathy

PAH: Polyallyl amine Hydrochloride

PDAC: Poly(Diallyl) Dimethyl Ammonium Chloride

PEM: Polyelectrolyte Multilayers

PLA: Poly-Lactic Acid

PLL: Poly-l-Lysine

PMSF: Phenyl Methyl Sulfonyl Fluoride

PSNPs: Polystyrene Spherical Nanoparticles

PV: Phenyl Valerate

QCM: Quartz Crystal Microbalance

SAM: Self-assembled Monolayer

SEM: Scanning Electron Microscopy

SPR: Surface Plasmon Resonance

SPS: Sulfonated Polystyrene

STM: Scanning Tunneling Microscopy

TEM: Transmission Electron Microscopy

TGA: Thermogravimetric Analysis

Tyr: Tyrosinase

UV: Ultra-Violet

SYMBOLS

S: Catechol

P: Quinone

ΔH : Heat of vaporization

R: Gas Constant

ζ : Zeta Potential

k: Boltzmann Constant

Ψ : Surface Potential

κ : Reciprocal thickness of diffuse layer

T: Temperature

ϵ_0 , ϵ_r : Permittivity

σ_0 : Surface Charge Density

Δ : Distance to the plane of zeta-potential from the surface

n: number concentration of each ion in the bulk

δ : Solubility Parameter

J: Joules

K: Kelvin (Temperature Unit)

m: Length (Meter)

s: Second (Time)

kg: Kilogram

Pa: Pascal

N: Newton

mol: Mole of substance

λ : "Kolmogorov Scale" Smallest Eddy Diameter

ϵ : Rate of Energy Dissipation

η_c : Viscosity of Continuous Phase

ρ_c : Density of Continuous Phase

σ : Interfacial Tension

d_{KH} : Inertial Regime Droplet Diameter

d_{KV} : Viscous Regime Stable Droplet Diameter

ΔU : Difference in rotational speeds of inner cylinder and outer cylinder in Couette-Taylor flow

Δr : Difference in radii of inner and outer diameter

γ : Surface tension

Z: Atomic Number

A: Atomic Weight

E_0 : Electron Beam Energy

ξ : Thickness of Material

f_A : Fraction of electron beam absorbed

f_B : Fraction of electron beam back scattered

f_T : Fraction of electron beam transmitted

1 INTRODUCTION

1.1 OVERVIEW OF NANOTECHNOLOGY

Nanotechnology is emerging as one of the greatest tool in advancement of fields from engineering, chemistry, physics and biology. Nanotechnology defines the fabrication and control of particles and molecules on nanoscale. One of the biggest challenges scientists face today is control over shape, size and placement of these particles for fabrication of large scale structures [1, 2]. Till now, most commercial nanotechnology based devices are made from “top-down approach”, but these technologies are soon expected to encounter fabrication size limitations. Hence bottom up approaches is gaining widespread interest and is considered to be a fore-runner in developing nanoscale fabrication tools which can either replace or assist existing nanofabrication tools.

“Bottom-up” methods for fabrication of nanoparticles vary from, spontaneous without constraints to directed or templated self-assembly processes. Spherical polymer nanoparticles can be prepared in solution by precipitation and solvent evaporation [3, 4]. Polymer spherical nanoparticles are readily fabricated and are commercially available. Metallic nanoparticles can also be readily produced by reduction of metal salts in solution phase chemistry and also the assembly of metal atoms in solution can be controlled to fabricate anisotropic structures. Various kinds of nanostructures using organic, inorganic and metals are prepared by researchers [5, 6]. Gold and silver nanoparticles are very popular because color of light they scatter can vary from visible to near infrared by varying their aspect ratio [7, 8].

In template assisted fabrication using the membranes, the pores can be filled by electrodeposition, sol-gel materials, polyelectrolytes or biomolecules to form wide range of multi-functional nanorods and nanotubes [9, 10]. Other fabrication techniques involve step-edge like fabrication or using biomolecules as templates. Allotropes of carbon like fullerenes, carbon nanotubes, and exfoliated graphite nanoplatelets have also been studied widely for possible applications in composites, biotechnology and electronics. Carbon nanotubes are considered to be one the strongest and highly conducting form of matter [11]. Graphite nanoplatelets can achieve very high surface area to weight ratio and are studied widely for enhancement in polymer composites. They also offer advantage to being electrically and thermally conducting [12, 13].

Carbon nanotubes also offer semi-conductor properties to be exploited in electronics and also for using them as biosensors [14]. Their small size also makes them a possible candidate for as a carrier for therapeutics. One of their biggest drawbacks in biological applications is lack of solubility in water. There has been a considerable effort to functionalize fullerenes, carbon nanotubes and graphite nanoplatelets, which can be essentially classified in two categories. One is using non-covalent attachments using surfactants, polymers, nucleic acids, peptides etc [15]. Other is by covalently functionalizing the surface by oxidizing surface carbon atoms to carboxylic groups and attaching other molecules or by directly attaching the moieties on the surface.

Other biggest challenge in the field of nanotechnology is arranging these nanostructures in a ordered form or creating nanopatterns for various applications. Conventional methodology for fabricating nanopatterns involves photolithography [16], scanning beam lithography [17]. Researchers have developed techniques based on

scanning probe methods where surface patterns can be manipulated and imaged simultaneously at atomic scale precision. It essentially comprises of using scanning tunneling microscopy [18] (STM) and atomic force microscopy (AFM) [18]. A number of different other procedure have also been developed to obtain nanoscale patterns using molding, printing and embossing. The techniques that are developed using these are microcontact printing [19, 20], replica molding [21], and nanoimprint lithography [22-24] etc.

Self-assembly is considered as one of the greatest tools in arranging these nanostructures and also achieving nanopatterns. Self-assembly is based on co-operative efforts of small molecules and nanostructures to organize themselves in predefined manner to form large scale 2 or 3 dimensional structures. Templated self-assembly is developing as a major tool that can fabricate periodic or patterned nanosize features. Assembly of colloids and other particles using magnetic or electric field has been used to pattern or arrange these nanoparticles and nanorods. Block co-polymers are also a well-known type of self-assembling polymers where immiscible blocks form micro-domains so as to minimize interfacial energy and maximize chain conformational entropy. This self-assembly can be control by template to obtained ordered orientation of the micro-domains to form nanopatterns [25, 26].

Other important self-assembly technique, that was developed in early 90s, is known as layer-by-layer (LBL) self assembly process [27]. It was initially developed using charged polyelectrolytes that can be adsorbed on a charged substrate and a charge reversal takes place. Then a layer to oppositely charged polyelectrolyte can be adsorbed to form a polyelectrolyte bilayer. This process can be repeated to form nanoscale thin

polymer films. Previous techniques like Langmuir-Blodgett (LB) films and self-assembled monolayer (SAM) can also form ultra thin films. But LB, though an elegant technique, requires expensive equipments and is not applicable to a wide range of molecules. SAMs can be formed only on limited substrates. LBL self-assembly process offers a much simpler and inexpensive technique for deposition of multilayer as well as allows incorporating different kinds of materials in those thin films [28]. LBL is not just limited to charged polymers, like polyelectrolytes. It has been shown that LBL self-assembly process can be extended to proteins, viruses, DNA and charged oligosaccharides. They are also been used to deposit inorganic materials like functionalized nanoparticles like carbon nanotubes, charged colloidal nanoparticles, nanosheets, and modified zeolite crystals [29].

Polymer nanoparticles are also gaining widespread interest in various fields of photonics, semi-conductors, optoelectronics, biocatalysis and drug delivery. Fabrication polymer nanoparticles in quick and efficient way are really important especially for targeted drug delivery. Nanoprecipitation and emulsion diffusion are some of the commonly used methods to fabricate polymer nanoparticles using various biodegradable nanoparticles for drug delivery applications.

The study of this thesis is based on two aspects of nanotechnology. One is finding simple and efficient ways to fabrication of polymer-based nanoparticles and controlling shape and size of the nanoparticles fabricated. Nanoparticles were prepared by using commercially available alumina membrane as templates. In other development poly-lactic acid nanoparticles where prepared by nanoprecipitation and emulsion diffusion process in a high shear rate nanomixer obtained from PRIMIX, Inc, Japan. This mixer

has a turbine rotating inside a cylinder and the particles are subjected to high shear rates. The affect of high shear rate on particles was studied using the nanomixer. Another aspect of this thesis involves assembling nanoparticles like carbon nanotubes along with proteins onto an interface to develop electrochemical biosensors to have real time detection of analyte of interest and also to couple two enzymes, namely Tyrosinase and NEST, onto an interface to study the inhibition of NEST which is a medically relevant protein.

1.2 FABRICATION OF NANOSTRUCTURES USING NOVEL NANOINJECTION PROCESS

Chapter 2 discusses a novel fabrication technique to make tapered nanorods from polymeric nanospheres [30]. Polystyrene spherical nanoparticles (PSNPs) are commercially available and were purchased from Polysciences, Inc. These spherical nanoparticles were used as the starting material for fabrication of nanorice and nanospears. Alumina membranes with cylindrical pores were used as the template for fabrication of nanorice and nanospears. An injection system was built to inject PSNPs suspended in DI water into the pores of the alumina membranes and once the required amount was injected. The membranes were taken out and heated to temperature slightly above the glass transition temperature of polystyrene. At that temperature the polystyrene partial wets the alumina membrane and as PSNPs are sitting adjacent to each other the combine to form nanorice or nanospears. Incomplete polystyrene nanotubes were also fabricated by heating membranes to temperature well above the glass transition temperature where polystyrene completely wets the alumina surface. Complete nanotubes can also be readily prepared and was demonstrated by fabricating epoxy nanotubes by complete wetting of pores of alumina membranes.

The injection system could also be used to decorate the inside of alumina membranes with gold nanoparticles. This was done by first functionalizing the inside of alumina membrane with silane-amines and then injecting colloidal gold nanoparticle solution. Gold nanoparticles are known to attach themselves to amine groups by chemisorption. Hence the channels inside the membranes can be functionalized using the same injection system.

1.3 STEP-EDGE LIKE TEMPLATED FABRICATION OF NICKEL NANOWIRES

Chapter 3 discusses a novel and simple method to form polyelectrolyte supported nickel nanowires [31]. Again alumina membranes were used as a template and instead of using the pores as the template pore wall edges were used as the template. In the method, first the whole membranes were treated with fluorosilanes. Fluorosilanes makes the whole membrane hydrophobic. Then these membranes were cleaved and in the process exposing the freshly cleaved pore edges. These edges are hydrophilic in nature and alumina membranes are positively charged at the pH of 7. These edges were used as templates to grow polyelectrolyte multilayers using LBL deposition. Then these films on the edges were used to deposit nickel using an electroless deposition bath. The thickness of nickel nanowires can be controlled by varying the deposition time. Hence a simple technique to make polyelectrolyte supported nickel nanowires is demonstrated.

1.4 HIGH SENSITIVITY TYROSINASE BIOSENSOR USING LBL DEPOSITION

Chapter 4 discusses the fabrication of catechol biosensor using a LBL deposition technique to immobilize enzymes onto an interface. LBL deposition is done on gold electrode or silver electrode by first functionalizing the surface of electrode by forming a self-assembled monolayer of thiol terminated compounds. This gives a surface charge on

the electrodes that can be further used to immobilize tyrosinase. Tyrosinase catalyzes the reaction of oxidizing catechol to quinone. The electrode is maintained at the potential of -0.1 V vs Ag/AgCl electrode and the quinone produced is reduced back to catechol at this potential.

Tyrosinase has isoelectric point of $\text{pH}=4.7-5$ and is negatively charged at a pH of 7. LBL is done using tyrosinase as one charged species and positively charged species used were different types of polyelectrolytes like poly-l-lysine (PLL) and poly(diallyl)dimethyl ammonium chloride (PDAC). Instead of polyelectrolytes functionalized nanoparticles like carbon nanotubes and polystyrene nanospheres were also used. The effect of different types of polyelectrolytes and functionalized nanoparticles on biosensor response was also studied. Addition of nanoparticles was advantageous in PDAC system; whereas it did not influence the biosensor response in PLL system. It showed the response of biosensor is a function of enzyme loading as well as substrate diffusion through the enzyme layer. Silver membrane were also used which increased the surface area to much greater extent and hence increased the sensitivity of the biosensor.

1.5 NEUROPATHY TARGET ESTERASE BIOSENSOR

In the chapter 5 a new design for fabrication of NEST biosensor is proposed [32]. NEST is a subdomain of a medically relevant protein called Neuropathy Target Esterase (NTE). NTE is a membrane protein which plays a critical role in nervous system of vertebrates and inhibition of this protein can cause delayed neuropathy and other motorneuron diseases. NTE is a difficult protein to express and purify, so the research is focused on a subdomain of NTE called NEST which maintains the same catalytic activity

as NTE. NEST when active catalyzes the hydrolysis of phenyl valerate (PV) to give phenol. Tyrosinase which is a poly-phenol oxidase oxidizes phenol to catechol and then catechol to quinone. Quinone is detected electrochemically at the electrode interface which is maintained at -0.1 V vs Ag/AgCl reference electrode.

NEST is immobilized on the electrode by LBL deposition along with tyrosinase. Gold electrode is first functionalized with thioctic acid which gives it a negative charge. PLL and tyrosinase bilayers were first added followed by addition of a layer of NEST. NEST is also negatively charged at the pH=7.0 and can be used as a negatively charged species in LBL deposition. The electrode with both the enzymes was maintained at a potential of -0.1 V and the aliquots of PV were added and the response of the NEST biosensor was measured. As the concentration of PV was increased there was increase in the current measured at the electrode.

The inhibition of NEST was studied by addition of chemical species like phenyl methyl sulfonyl fluoride (PMSF) to the bulk solution and the magnitude of current measured from the NEST biosensor went down as the concentration of PMSF was increased. Hence it demonstrated the real time detection of inhibition of NEST electrochemically.

1.6 FABRICATION OF POLY-LACTIC ACID NANOPARTICLES USING HIGH SHEAR RATE NANOMIXER

Chapter 5 studies the effect of high shear rate nanomixer on the formation of poly-lactic acid (PLA) particles formed by nanoprecipitation and emulsion diffusion. Nanoprecipitation requires a solvent to dissolve poly-lactic acid and a non-solvent of polymer. It also requires the solvent phase and non-solvent phase for polymer to have high miscibility that causes polymer to precipitate out readily as solvent diffuses into

non-solvent case. A surfactant can also be added to stabilize the polymer particles once they are formed and further prevent them from agglomerating or aggregating.

Nanoprecipitation was carried out by dissolving poly-lactic acid in acetone and a surfactant, Pluronic F68 in de-ionized (DI) water. Pluronic F68 is co-polymer of polyethylene and polypropylene glycol and it stabilizes the nanoparticles formed by precipitation. It was followed by injection of PLA solution in DI water with surfactant in the nanomixer. The affect of mixing speed was studied by adding same amount of PLA solution in fixed amount of DI water with surfactant. The affect of a different surfactant was also studied by using cetyl trimethylammonium bromide (CTAB) which has a positive charge on it. Zeta-potential was measured for both kinds of particles. CTAB stabilized particles had stronger charge in magnitude as compared with Pluronic F68 stabilized particles. CTAB stabilized particles showed similar trend as in the case of Pluronic F68.

Emulsion diffusion was carried out by using immiscible solvent-non-solvent system of ethyl acetate and water. Poly-lactic acid was dissolved in ethyl acetate and Pluronic F68 in DI water. 20 ml of PLA solution was added along with 60 ml of Pluronic F68 solution and emulsified in nanomixer at different mixing speeds and different time duration. The emulsion was collected and added to excess amount of pure DI water for ethyl acetate to diffuse into water. This causes PLA particles to form and they were stabilized by the surfactant present in surrounding water. The particles size went down with increasing mixing speeds but it was also a function of mixing time. The effect of viscosity of continuous phase was also studied by using water-glycerol mix. The viscosity also influenced the particle shape as higher viscosity changes the mixing regime

in the nanomixer. Finally it discusses the influence of electron beam while imaging the nanoparticles. As the beam has strong energy the PLA particles deformed under the influence of electron beam. It also describes the effect of thickness of gold film on the polymer particle deformation and how electron beam used of imaging can damage particles.

2 FABRICATION OF NANOSTRUCTURES USING NOVEL NANOINJECTION PROCESS

2.1 INTRODUCTION

Nanosized functional particles are attractive for optical, electrical, magnetic, and biological applications. Recently, in addition to nanosize, the shape of nanoparticle is reported to be crucial, for example, in how it interacts with light by Halas and coworkers [33]. They found that rice-shaped nanoparticles made of gold and iron oxide is the most sensitive surface plasmon resonance (SPR) nanosensor yet devised. They hope to get a far clearer picture of proteins and unmapped features on the surface cells by attaching them to scanning probe microscopes.

Although there are tremendous potential advantages of using anisotropic nanoparticles like nanorice instead of conventional spherical nanoparticles, the development of controlling such shape on the nanoscale is in its early stage. Some controlled growths of the end shape of nanorods with specific equipment at specific conditions have been reported for inorganic or metallic nanoparticles [34, 35]. Even though polymer nanorods and nanotubes have commonly been produced, since the fabrication was introduced by Wehrspohn and coworkers [36], terminal contour control of polymer nanoparticles like nanorice or nanospears has remained as one of challenging tasks. If functional polymer nanoparticles can be shaped in the desired forms on the nanoscale, they can easily be functionalized to have far enhanced multifunctional properties using them as templates or substrates. In the fabrication of nanorods and nanotubes, template-assisted fabrication is gaining widespread interest because of its simplicity. Such novel nanostructures are expected to provide new functions in

optoelectronic and biological applications that can not be attained with conventional spherical nanoparticles. Researches have used various kinds of membranes such as polycarbonates and anodized alumina membranes as templates for the fabrication of nanotubes and nanorods [37-41]. However, no report of polymer nanorods has shown control of both aspect ratio and terminal contour. Additionally, no polymer nanospheres have been incorporated into the production of nanorods. Mostly, monomers, polymer melts or solutions are introduced into the nanopores for the production of nanorods and nanotubes. Other template assisted techniques use the step-edge [42] and other methods involving template molecules in solution [43]. Other nanorods production techniques which do not require templates include the electrospinning of nanofibers [44, 45] and also using biomolecules and self-assembly processes [46, 47].

The techniques that use membranes as templates include electrodeposition [48], layer-by-layer deposition [10, 49, 50] and methods using commercially available metal plating solutions [51, 52]. Zheng *et. al.* have fabricated copolymer nanotubes and nanowires by having polymerizing copolymers inside the pores of alumina membranes [53]. Anisotropic metallic nanoparticles like conical nanotubes rather than cylindrical nanotubes and nanorods have also been fabricated. Such anisotropic nanoparticles were fabricated using either a complex chemical vapor deposition set-up [54] or a tapered pore that is coated with gold [55]. However, in this work for the first time we report the fabrication of tapered nanorods of varying aspect ratio and controlled terminal-contour (e.g., nanorice to nanospears) using a simple method. First, our method exploits the injection of a controlled amount and size of nanospheres into the cylindrical nanopores of an alumina substrate. Second, the resulting nanostructures are controlled during the non-

uniform heating of the polymer nanospheres by capillary forces, and wetting (or dewetting) onto the cylindrical alumina walls.

To achieve faster production and also obtain subtle variation in the shape, size, and aspect ratio of nanoparticles, we have created a fabrication method using polymer nanospheres and anodized alumina membrane templates that control the structure of the resulting nanoparticles. Our system for fabricating novel nanorice and nanospears is easy to set-up and perform on a laboratory bench top. Nanoscale fabrication was made without the hassle of an elaborate set-up involving vacuum chambers or expensive equipment that are normally required for lithography based fabrication. The cost of running the experiment was very low and the fabrication of different types of nanostructures was easily performed by changing key parameters, such as the particle size, template pore size, length of ultrasonication and changing temperature or heating time. The same step is also used to illustrate the versatility and the pores of alumina membranes where decorated with gold nanoparticles by using the same system.

2.2 EXPERIMENTAL SECTION

2.2.1 Materials

Alumina membranes were purchased from Whatman with different pore sizes 20nm, 100nm and 200nm. Polystyrene nanoparticles from Polysciences with mean diameter as 140 nm, 50 nm and 100 nm. Sodium Hydroxide, 3 methoxy aminosilanes, gold chloride trihydrate, NaOH, hydroxylamine and sodium citrate from Sigma Aldrich.

2.2.2 Experimental Details

In this work, we used commercially available alumina membranes (Whatman Anodized Alumina Membrane) as templates and polystyrene (PS) nanospheres (neutral, carboxylated, or sulfated polystyrenes from Polysciences, Inc.) for the fabrication of controlled aspect-ratio and terminal contour controlled nanoparticles (i.e., nanorice and nanospears). The pores of these membranes were filled with nanospheres by a solvent aided injection. Subsequent heat treatments then allowed the nanoparticles to coalesce and wet (or dewet) from the alumina nanopore walls and form nanoparticles with a controlled aspect-ratio and an interesting terminal curvature (i.e., round to sharp or pointed). We assembled a small solvent-aided nano-injection unit for injecting materials into the cylindrical alumina nanopore membranes as shown in Figure 2.1.

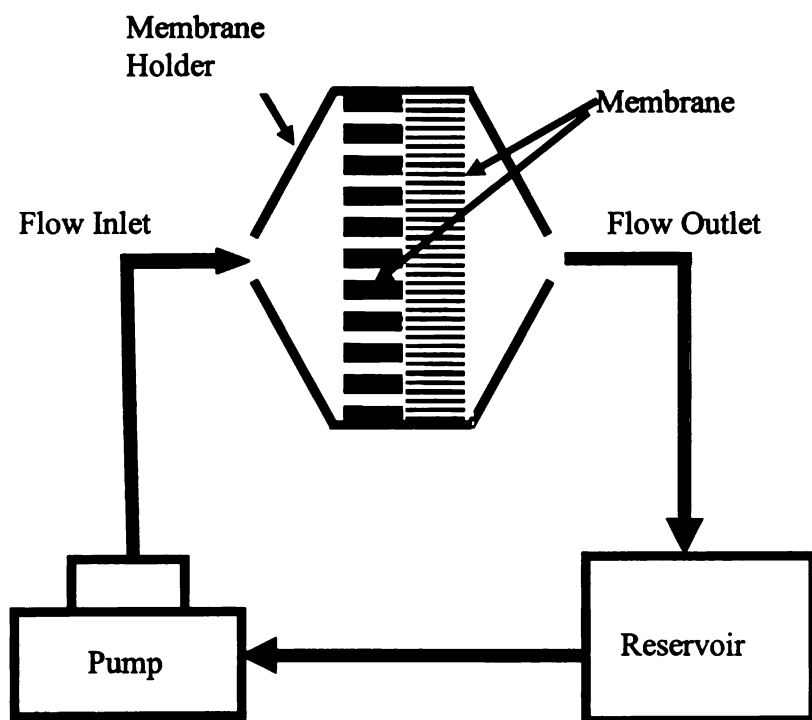


Figure 2.1: A system of solvent-aided nano-injection of nanospheres.

Figure 2.2 illustrates the overall process. A specific amount of PS nanosphere suspension was put in the reservoir and then it was pumped through the membranes with desired pore sizes in series (first large and then small pores) or a membrane having both large and small pores at each side. The size of nanospheres was in between the large and the small pores so that the nanospheres are trapped only in the large pores. Once the large pore membrane was filled with the desired amount of nanospheres it was carefully taken out, heated at 120°C (above the glass transition temperature of the polymer) for various amount of time, and then placed in a 3 M NaOH aqueous solution where the alumina membranes dissolved. Then the remaining polymer nanoparticles were filtered using a centrifuge and washed several times in deionized (DI) water to remove any residual NaOH. To image the resulting structure of nanoparticles, a drop of the sample suspension was put on a glass slide and then dried. The dried samples on a glass slide were sputtered with gold (around 5 nm thick) for scanning electron microscopy (SEM) analysis. SEM used for high resolution imaging was JEOL 6300F with field emission.

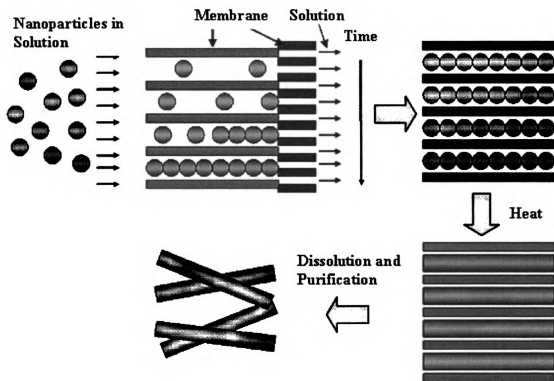


Figure 2.2: Schematic illustration of solvent-aided nano-injection molding process using alumina membranes having cylindrical nanopores.

Gold Nanoparticles were prepared by the standard procedure of reduction of gold salt by sodium citrate. 500 mL of 1 mM HAuCl₄ was brought to a rolling boil with vigorous stirring. Rapid addition of 50 mL of 38.8 mM sodium citrate to the vortex of the solution resulted in a color change from pale yellow to burgundy. Boiling was continued for 10 min; the heating mantle was then removed, and stirring was continued for an additional 15 min [56]. The gold nanoparticle suspension was cooled to room temperature and then stored at 4°C for further use.

The membranes were decorated with gold nanoparticles using the same injection molding system. Alumina membrane of 200nm pore size diameter was placed inside the membrane holder. Instead of pumping polystyrene nanoparticles, ethanolic solution of

5mM amino-silanes was first injected through the membrane for 20 mins. Then pure ethanol was injected for 10 mins to flush the membranes. The membranes were carefully taken out from the holder and were placed in oven preheated to 60°C for 4 hours. This would cause the silanes to crosslink with alumina membrane which has hydroxyl groups on its surface. Once crosslinked, the membrane was taken out and placed back in the membrane holder. Gold nanoparticle suspension, prepared as described in previous section, was injected through the membranes. Gold nanoparticles are known to chemisorb on amine terminated self-assembled monolayers [57]. The membranes then were flushed with pure water, taken out and cleaved for imaging under SEM.

2.3 RESULTS AND DISCUSSIONS

Figure 2.3A shows tapered nanorods of smaller aspect-ratio (i.e., nanorice) that were fabricated by limiting the amount of nanospheres injected through the membrane. Figure 2.3B shows a higher magnification image of the nanorice. Figure 2.3C shows the nanorods tapered at the ends were made of (8.1 mg of 140 nm PS nanoparticles in 200 ml of water) PS nanospheres in 200 nm pore-size alumina membrane stacked against 20 nm pore-size membrane. A unique and peculiar terminal contour was observed of these polymer nanorods (i.e., nanospears). As far as we know, there has been no report on such sharp-pointed polymer nanorods that were fabricated with a uniform size at the nanometer scale. In addition, we used smaller nanospheres and a smaller membrane. This membrane has two pore sizes at each end, 20 nm and 200 nm. Both pores are cylindrical and they meet at around 2 μm from the 20nm end. The concentration for 50

nm PS nanospheres was 2.3 mg in 200 ml of DI water. 100 ml of this suspension was injected from the large pore side to the small side and then was heated at 120 °C for 2 hours. Since these nanospheres (50 nm) were much smaller than the large pore (200 nm) in size they must have been closely packed and this case we observed much longer and sharper tapered nanowires, as shown in Figure 2.3D.

A possible explanation for the formation of the tapered tip is illustrated in Figure 2.4. When the cylindrical pore diameter of the membrane was 200 nm and the PS nanospheres were 140 nm in diameter, nanospheres align themselves in the cylindrical pores. Pore diameter was larger than the nanosphere diameter. Hence all the nanospheres (140 nm case) had only a small contact area with the pore wall as shown in the left side of Figure 2.4. This illustrates an exaggerated effect of non-uniform heating and resulting on the coalescence of nanospheres, and the shape change caused by wetting (or dewetting) and capillary force.

As the nanospheres-filled membrane was heated above the glass transition temperature of the polymer used, there would be two main heating mechanisms, conduction through the alumina wall and convection through air. The radiation would be negligible because of the low temperature.

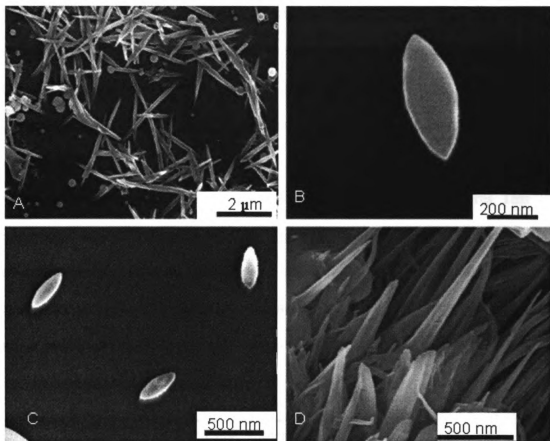


Figure 2.3: SEM images of novel tapered nanorods. A) Nanorice (small aspect-ratio (~2) tapered nanorods). B) Higher magnification image of Nanorice. C) Nanospears made of PS nanospheres (aspect ratio ~10). D) Nanospear bundles formed by pumping 50 nm PS particles into a single membrane that has 20 nm and 200 nm pore sizes at either ends. The nanospheres were pumped into 200 nm pore side.

As the pore wall is a better heating source than air. There would be more heat transfer through the small contact area between the wall and nanospheres than through air. Hence the nanospheres would start to partially deform and wet at the pore wall. As polymers are being softened in the cylindrical nanodomain, capillary forces come to play an important role in moving and shaping the softened polymer parts [36, 58].

Capillary force can allow these softened polymers to flow slowly onto the nanopore walls, thus adjacent nanospheres coalesce to form continuous shape. The

nanosphere at the end just stretches further along the cylindrical nanopores. Because the end nanosphere did not have another nanosphere to coalesce with, it forms a tapered end as illustrated in Figure 2.4.

During the solvent-aided nanoinjection process, the nanospheres tend to stay separated from each other rather than sitting adjacently. Intermediate ultrasonication of the membrane is required to tightly pack the nanospheres into the membrane pores. This intermediate step of ultrasonication after pumping the certain amount nanosphere suspension also helped remove excess particles which tend to stay on the membrane surface. These particles could prevent further nanospheres from being delivered to the membrane pores and reduce the aspect ratio of nanorods.

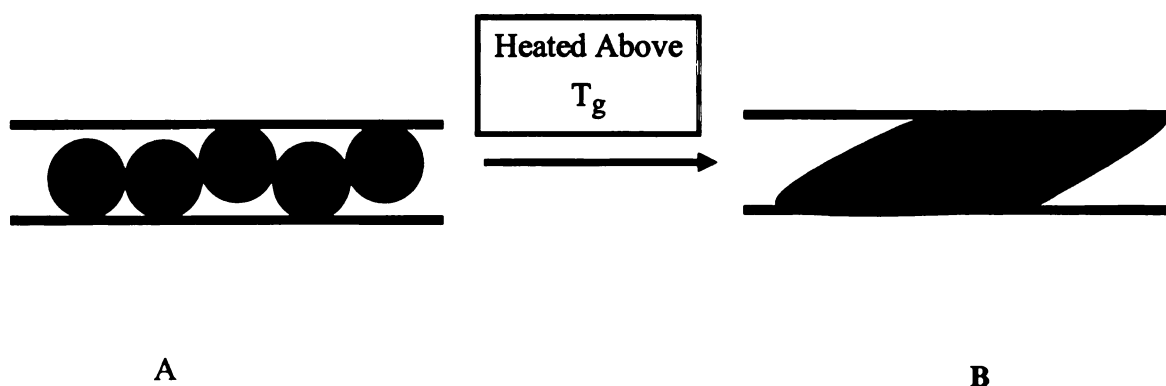


Figure 2.4: Schematic representation of tapered nanorods and nanospears forming due to partial wetting of alumina by polystyrene.

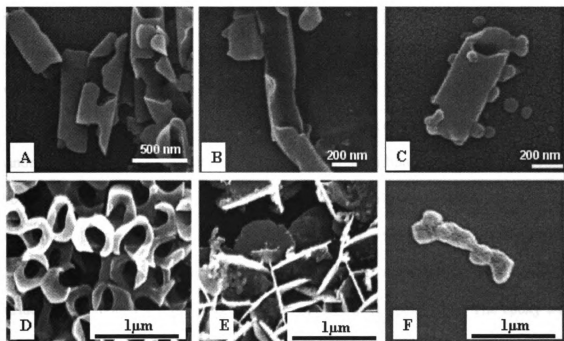


Figure 2.5: SEM images of incomplete nanorods using nanospheres. A) Incomplete nanotubes were observed after sintering of 140 nm PS nanoparticles inside a 200 nm pore size membranes. B) A half open nanotube formed inside a 200 nm pore size membrane. C) A small aspect ratio nanotube. D) Broken nano-doughnuts using 140 nm particles in a single 200-20 nm pore size membrane. E) Nanodiscs formed using 100 nm PS spheres in a single 200-20 nm membrane without ultrasonication. F) An intermediate structure with incomplete melting of the polymer nanospheres.

As shown in Figure 2.5, we also observed various other nanostructures like incomplete nanotubes (i.e., perforated nanotubes) (A, B, and C), broken nanodoughnuts (D), and nanodiscs (E). These nanostructures show evidence for the thermal wetting of PS onto the cylindrical alumina nanopore walls as heat transfers to PS nanospheres through the wall. As the temperature is increased well above the glass transition temperature the PS completely wets the surface of alumina nanopores and due to limited supply of polymers forms incomplete nanotubes [59]. It is expected that further variation of the PS nanospheres packing, heating temperature, and time would allow the fabrication of novel nanostructures. Figure 2.5F illustrates the intermediate step in the coalescence

of the particles. Due to a short heating time, the spherical particles have not completely lost their structure. The nanospheres towards the middle can be seen merging together whereas the nanospheres at the end are tending to form a slightly tapered shape.

The energy dispersive spectroscopy was also carried out for the nanospheres and nanorice. It showed that the particles comprise of mainly carbon. EDS is shown in Figure 2.6 with small peak for carbon which was absent in the spectrum obtained for background. This confirms the presence of carbon as main constituent of nanoparticles.

Complete nanotubes can be readily prepared by using a polymer that completely wets the surface was demonstrated by using commercially available epoxy-resin. The epoxy was mixed with the cross-linking agent in the ratio of 1:1 as specified by the manufacturer. Alumina membranes were smeared with the epoxy and the epoxy which completely wets the membrane went inside to form nanotubes. Epoxy was allowed to cure inside oven at 80°C for 1 hour. The alumina membranes were dissolved in 3M sodium hydroxide and the nanotubes were imaged under SEM as shown in Figure 2.7.

The same system was used to decorate the pore walls of anodized alumina membranes. The membranes were functionalized by crosslinking silanes which have amine functional groups. The gold nanoparticles pumped through the membranes chemisorbed on the amines to form a fine dispersion of gold nanoparticles along the length as shown in Figure 2.8. It is an SEM image of gold nanoparticle decorated pore of cleaved alumina membrane.

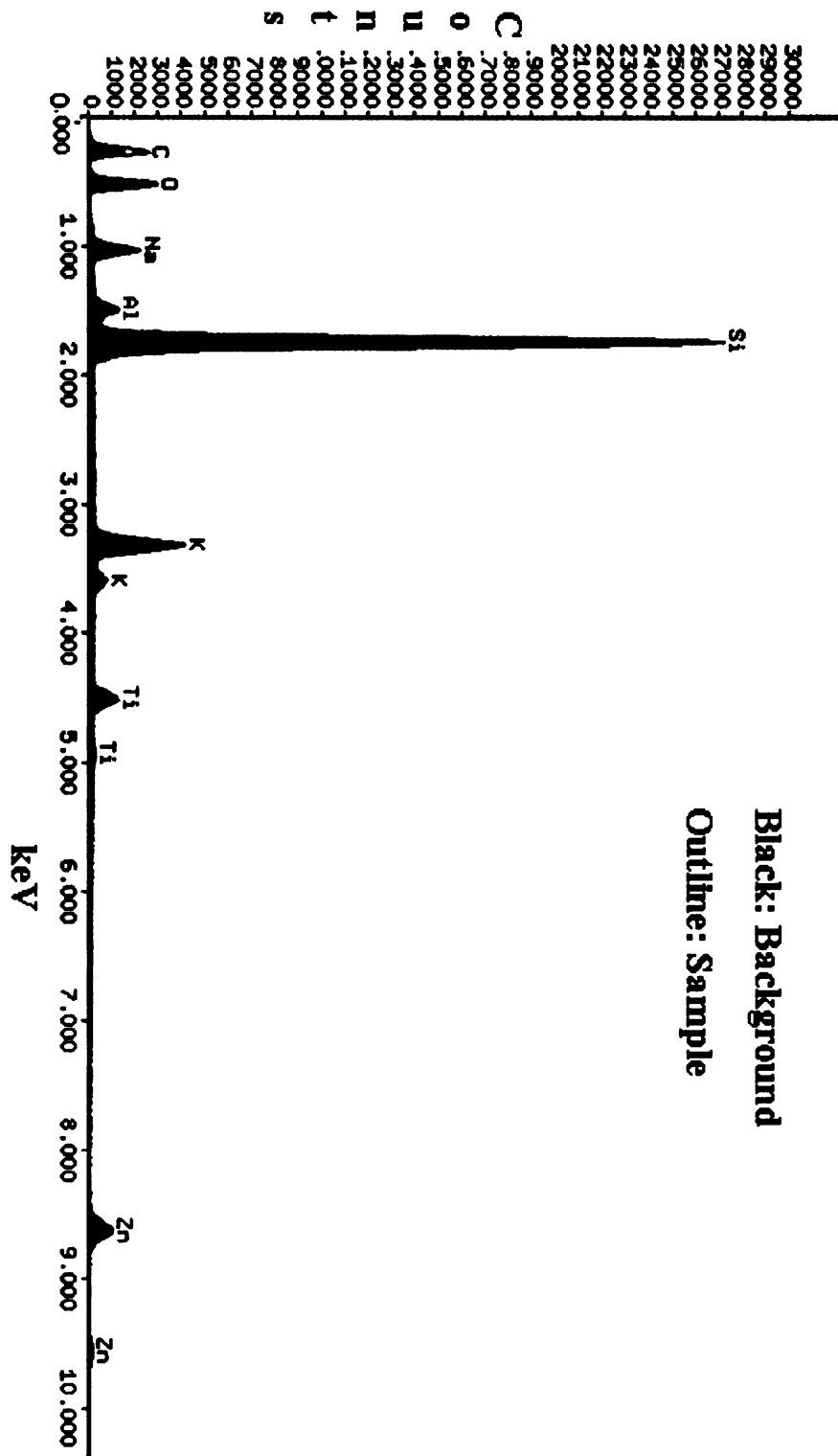


Figure 2.6: Energy dispersive spectrum (EDS) of fabricated nanoparticles is shown above. The black spectrum is the background and the line is the spectrum of the fabricated nanoparticles. The difference in the count of carbon content shows the presence polystyrene which is composed of carbon and rest of the elements do not show any increase.

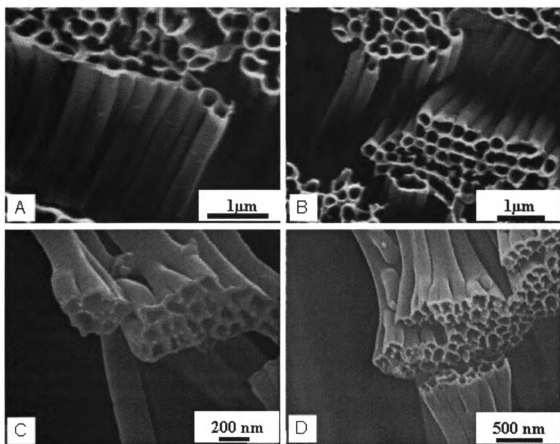


Figure 2.7: SEM image of epoxy nanotubes prepared using A) and B) 200 nm & C) and D) 100 nm pore sized alumina membranes.

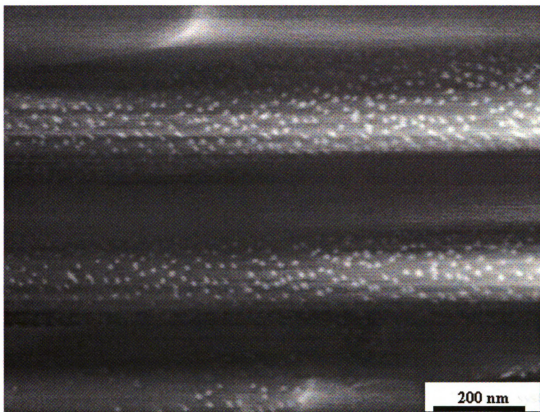


Figure 2.8: Cross sectional SEM of alumina membrane. Its pores are decorated with the gold nanoparticles.

2.4 CONCLUSIONS AND FUTURE WORK

In conclusion, we present a very versatile and effective approach for shaping nanoscale structures using ordered nanopored membranes and a simple solvent-aided nano-injection molding process of polymer nanospheres. By exploiting non-uniform heating and resulting wetting or capillary forces of nanospheres filled inside the cylindrical nanopores of membranes we obtained novel nanostructured, anisotropic nanoparticles such as nanorice and nanospears. As far as we know, these nanostructures are unique and have not been prepared using other methods. This method is very easy to implement without any complicated chemistry or expensive equipments. Therefore, after obtaining spherical nanoparticles of any materials, this method can easily change the symmetrical nanoparticle into other geometries with less symmetry. The same system was used to functionalize the alumina membrane with amino-silanes and was further decorated with gold nanoparticles.

The same system can be used to pump other kind of solutions like enzymes and polyelectrolytes to form nanotubes. It can also be used to make chains of nanoparticles by stacking them inside the pore and then cross-linking them to form nanochains.

3 STEP-EDGE LIKE TEMPLATED FABRICATION OF NICKEL NANOWIRES

3.1 INTRODUCTION

One of the biggest challenges in the field of nanotechnology is the cost-effective fabrication of nanowires. To date there are many methods that use top-down approaches or involving elaborate equipments to form nanowires like dip-pen [60] and electron beam lithography [61], but both are expensive and slow. Cost effective methods such as soft-lithography [62, 63] and nanoimprint lithography [22-24] are also being developed. The bottom-up approach involves the self-assembly of molecules based on various interactions like electrostatic, hydrogen bonding or covalent bonding. It offers a more cost effective method for the fabrication of nanostructures. It also provides more control over the variety of nanostructures that can be fabricated. Nanowires and nanotubes of various materials have also been fabricated using template assisted techniques like filling the membrane pores of anodized alumina [10, 30, 36, 38, 48, 58], track etched polymer membranes [49, 55] and decoration of step-edges [42, 64, 65]. Most methods using membranes as a template involve electrodeposition. This is done by coating one side with a metal to make it conductive, followed by electrodeposition of the metal inside the pores. Electroless methods are slightly more difficult, especially in depositing metal inside the pores, as the process is hindered by the slow diffusion of metal ions into pores. There are a variety of metals that are being used to make nanowires such as gold [40], copper [66, 67] and silver [68, 69]. Nickel nanowires are also finding great interest among researchers due to their unique magnetic properties. Also at the nanometer scale, quantum confinement leads to unique properties. For example, the band gap of nanowires

varies as the inverse square of its diameter [70]. Biological molecules can also be attached to nanowires to form nano-machines [71]. Most fabrication methods for nickel nanowires and nanotubes involve filling pores of membranes [72, 73], step-edge [74] and also using biomolecules like DNA [75].

In this work, we report a step-edge like methodology for the fabrication of polyelectrolyte supported nanowires. Polyelectrolytes provide flexible support to metallic nanowires and prevent them from falling apart. Our method is simple, can be performed on lab-bench top and does not require any equipment for metal deposition. In our method an alumina membrane is functionalized with hydrophobic molecules and then broken to expose freshly cleaved hydrophilic edges along the broken pore walls. Then, polyelectrolyte multilayers (PEMs) were built on the hydrophilic edge of the pore membrane and an electroless nickel bath was used for the deposition of nickel onto the multilayers to form nickel nanowires. After dissolving the membrane, free standing nickel nanowires were obtained.

3.2 EXPERIMENTAL SECTION

Anodized alumina membranes of 200 nm pore size were purchased from Whatman. The fluorosilanes (tridecafluoro-1,1,2,2-tetrahydrooctyl)-1-methyldichlorosilane) were purchased from United Chemical Technologies Inc. 16-mercaptohexadecanoic, positively charged polyelectrolyte, poly(diallyldimethylammonium chloride) (PDAC), ($M_w \sim 100,000-200,000$) and negatively charged polyelectrolyte, poly(styrene) sulfonate (SPS) ($M_w \sim 70,000$ g/mol), were purchased from Sigma Aldrich. The bath for electroless deposition was prepared

using nickel sulfate, sodium hydroxide, sodium citrate, lactic acid and dimethylamine borane (DMAB); all purchased from Sigma Aldrich. The palladium catalyst ($\text{Na}_2[\text{PdCl}_4]$) was purchased from Strem Chemicals, More details on electroless nickel deposition can be found from our previous work in which selective nickel plating was made on the particle arrays deposited on patterned polyelectrolyte templates [76].

In this work, alumina membranes were first treated with fluorosilanes by chemical vapor deposition. Both the fluorosilanes and the membranes were placed under vacuum for 30 mins. This was followed by two hours of heating at 120°C which allows the silanes to cross-link with alumina membrane both inside the pores and on outer surface. The fluorosilane treated surfaces are extremely hydrophobic. This was followed by breaking the membrane which exposes the freshly cleaved alumina surface that is hydrophilic [32], unlike the other surfaces of the membrane.

These fresh hydrophilic edges now act as templates for deposition of PEM and nickel. The alumina membrane is positively charged at a pH of 7 because the isoelectric point of alumina is at around pH 8-9 [77]. Polyelectrolyte multilayers were selectively built on the hydrophilic edges by dipping broken membrane in (1) SPS and (2) PDAC solutions for 30 minutes each. Intermediate washing steps were carried out using de-ionized (DI) water. Two bilayers of $(\text{SPS}/\text{PDAC})_2$ were built leaving a positively charged polyelectrolyte (PDAC) at the top.

The PEM coated membranes were then immersed in a negatively charged palladium catalyst for 15 seconds and rinsed with DI water at pH of 3.0. The palladium catalyst is necessary to reduce Ni^{2+} to metallic Ni. With out the catalyst, nickel will not plate on any surface. The Pd catalyst was adsorbed onto the PEM surface through

electrostatic interactions and is the location where the reduction of Ni ions to Ni metal occurs. This gives rise to the nanowires structure supported by polyelectrolytes. The nickel reduction occurred when samples were placed in a 100 mL nickel bath whose composition is summarized in Table 3.1. Before use, the pH of the nickel bath was adjusted to 6.5 ± 0.1 by adding small amounts of 1.0 M NaOH. Electroless deposition times of up to 10 minutes were used.

Table 3.1: Chemical composition of a 100 ml nickel bath used for electroless deposition

Nickel Sulfate	4.0 g
Sodium Citrate	2.0 g
Lactic Acid	1.0 g
DMAB	0.2 g

Once nickel was deposited, the membrane was dissolved in 3M NaOH to extract the nickel nanowires. Nickel nanowires were filtered and washed in DI water using a centrifuge. Nickel nanowires were imaged using a scanning electron microscope (SEM, JEOL 6300F) by drop coating a glass slide with a suspension containing nickel nanowires which were sputter coated with 7 nm of gold before imaging. Energy dispersive spectroscopy (EDS) was also done to analyze the composition of the nanowires.

Quartz crystal microbalance (QCM) crystals (5 MHz, Maxtek, Inc., Santa Fe Springs, CA) with gold electrodes were cleaned in piranha solution (7 parts concentrated sulfuric acid and 3 parts 30% hydrogen peroxide) for thirty seconds followed by rinsing with an excess of DI water and drying by a steam of nitrogen. A self-assembled monolayer (SAM) of 16-mercaptohexadecanoic acid was formed on the surface of the

QCM crystals by immersion in a 5 mM ethanol solution for one hour followed by rinsing with ethanol and drying with nitrogen. Then ten and a half bilayers of (PDAC/SPS)_{10.5} were formed on the –COOH terminated SAM. The QCM crystals were then immersed into a palladium catalyst solution for 30s, rinsed with DI water and dried with nitrogen.

3.3 RESULTS AND DISCUSSIONS

Figure 3.1 illustrates the scheme for the formation of the nickel nanowires. Here the fabricated nanowires have two different materials interwoven along their length. The side of the nanotubes that was in contact with the alumina membrane is polyelectrolyte whereas the other side is metal. Hence this simple technique can impart two different functionalities on the same wire. The thickness of each side can be controlled by changing the number of PEM bilayers and the electroless deposition time.

The initial width of the edges can be estimated theoretically from the data given by the manufacturer. The surface density of the 200 nm diameter pores in the membrane is approximately 10^9 pores cm^{-2} . The linear pore density can be approximated to 3.1×10^4 pores cm^{-1} . Hence, the average spacing between the pores can be estimated as:

$$d_{\text{avg}} = \frac{(1 - 31,000 \times 200 \times 10^{-7})}{31,000} \text{ cm} = 125 \text{ nm} \dots\dots\dots(3.1)$$

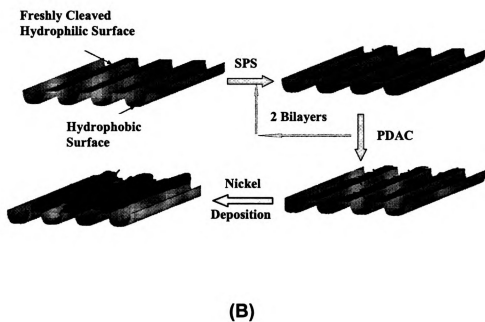
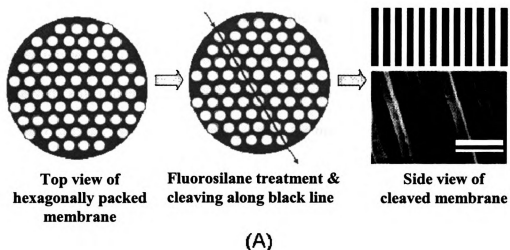


Figure 3.1: A) Schematic representation of the template formation process including top and side views of alumina membranes before and after the cleavage. A side view SEM image after the fluorosilane treatment and cleavage is shown, the scale bar is 500nm. The actual membranes have quasi-hexagonally packed nanopores, but hexagonally packed nanopores were assumed for the determination of the cleaved edges in which nickel nanowires grow. B) Schematic illustration of each step of the nanowire formation process, deposition of PEM layers selectively on the freshly cleaved hydrophilic edge area and then selective nickel deposition followed.

We also observed the cross-sectional of the alumina membrane using a SEM. From these images, we estimated edge size which to be approximately 101.5 ± 32.4 nm. This observed value is consistent with the estimated value.

The PEMs act as adhesion layers between the membrane and the metal. Without the PEM layers the nickel would not grow. Also the polyelectrolytes are hydrophilic molecules so after treating membranes with fluorosilanes, the treated part repels the adsorption of polyelectrolytes. Hence, once the membrane is broken, the polyelectrolytes are selectively deposited on the new exposed region which is hydrophilic.

The purpose of polyelectrolytes is two fold. First it provides a surface adhesion layer for the negatively charged catalyst to deposit followed by the growth of metal. It also helps to form a continuous support on the edge of the membrane. Since polyelectrolytes are fuzzy structures (i.e., layers of polymer which are intertwined), it can compensate for the irregularities on the edges, hence providing a smoother support for metal wire. Also the electrostatic interactions among the polyelectrolyte layers provide a strong adhesion layer for metal growth. The polyelectrolytes used were strong polyelectrolytes hence the charge on them is independent of the surrounding pH environment. So these bilayers maintain their structure and strength in the low pH condition, while washing of catalyst, which it encounters during the growth of the metal.

We did not deposit more than two bilayers since a larger number of bilayers may cause multilayers on adjacent edges to merge as the diameter of nanowires for 2 bilayers of polyelectrolytes was approx. 200 nm. The thickness of the multilayers grows with the number of bilayers and in this case the polyelectrolytes are growing on an edge. Our

previous work on this system shows that each bilayer of PDAC/SPS is 3.4 nm in thickness [78].

We investigated whether the PEM were required to form nanowires. The role of polyelectrolytes was confirmed by a control experiment. As before the alumina membrane was treated with fluorosilanes and then broken. However the PEM were not deposited. The membrane was then dipped into the negative catalyst solution and nickel was electrolessly deposited directly on the edges of the alumina membrane. This was followed by filtering and washing. This resulted in no nanowires structures being formed. A second control experiment was performed where the membrane was not treated with fluorosilanes and broken. This time nickel growth occurred at the top and bottom surfaces as well and not exclusively on the pore edge of the membrane. Again no nanowires were obtained.

Nickel nanowires were obtained by the dissolution of the alumina membrane and further purified by repeated washing and filtering using a centrifuge and DI water. The samples were imaged using SEM. The images obtained are shown in Figure 3.2. The length of the resulting nanowires was 2-4 μm though the membranes are 60 μm in thickness. The shorter than expected length could be due to breaking of wires during repeated filtering process. Figure 3.2A shows nickel nanowires growing on the pore edges in an alumina membrane. Figure 3.2B is an image showing a collection of nickel nanowires.

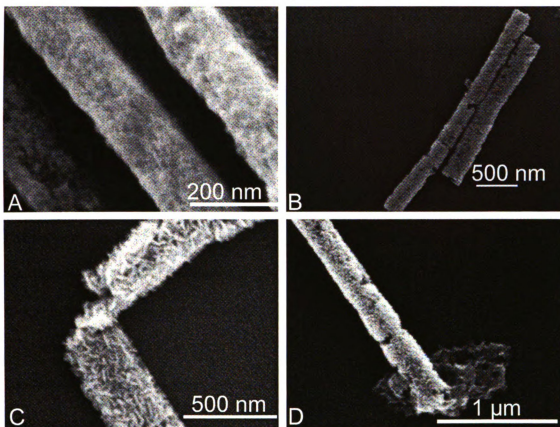


Figure 3.2: of nickel nanowires after dissolution of alumina membrane. C) Fuzzy nanostructure showing polyelectrolyte base as support for nickel growth. D) A nickel nanowire with spreading ends showing possible deposition of polyelectrolytes on the top surface of alumina membranes.

of the nanowire. This fuzzy surface structure is caused by the presence of the supporting polyelectrolytes layers. Hence the fabricated nanostructures can be considered more like metal nanocactuses (desert plants) supported by a nanofilm of polyelectrolytes. Figure 3.2D shows the end of a nanowire where the metal end is spreading out. This is probably due to the metal film forming at the end of a pore where polyelectrolytes might have deposited at the top surface of the membrane and not in the pore of the membrane.

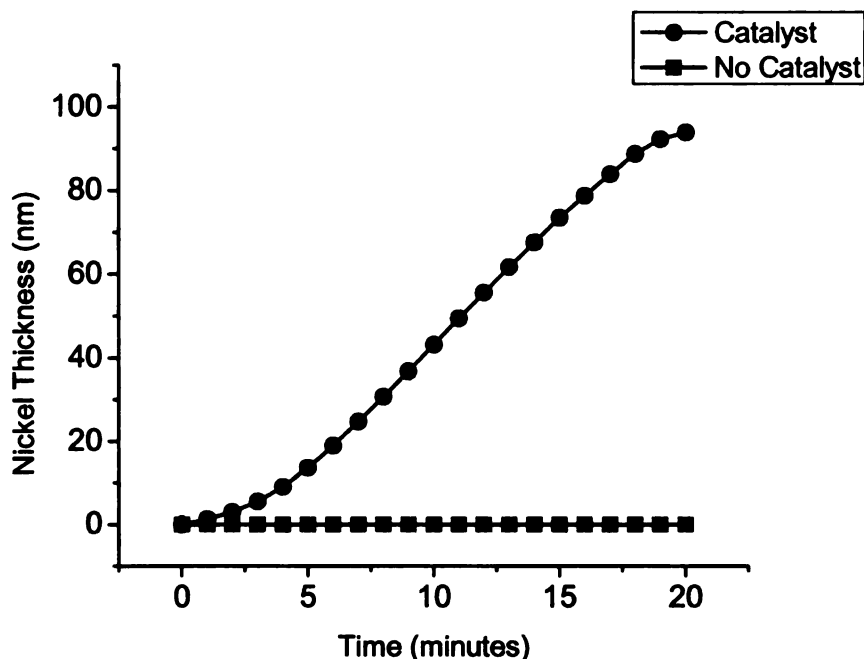


Figure 3.3: Rate of nickel deposition determined from Quartz crystal microbalance.

We estimated the thickness of nickel film growing on polyelectrolytes by using QCM. This was done by, adsorbing a $-\text{COOH}$ terminated SAM onto gold coated QCM crystals. Next polyelectrolytes are deposited on to the SAM followed by the deposition of nickel. The weight of nickel deposited causes a shift in the resonance frequency of the quartz crystal. Hence the rate of nickel deposition was calculated by measuring the change in frequency of the quartz crystal. The thickness of nickel is plotted as a function of time and is shown in Figure 3.3. We have also created homogeneous nickel films on planar substrates. Measurement of these thin metal films shows that they are conductive. However, we have not independently measured the conductivity of the nickel nanowires. Samples with no catalyst showed no controlled nickel deposition. Samples with the palladium catalyst showed initial non-linear growth as the nickel agglomerated on the surface and as time passed coalesced into a uniform coating. Once the surface is uniform the deposition became linear at a rate of 5.9 nm per minute for plating times between five

minutes to fifteen minutes. At about 20 minutes the plating rate slowed and became non-linear before the nickel started delaminate and peel off due to the buildup of internal stresses.

Based on the QCM data shown in Figure 3.3 and our previous work on the PEMs [78], the PEM-nickel nanowire has a thickness of around 47 nm, 7 nm from the PEMs and 40 nm from the nickel. Each thickness can be adjusted by changing the number of PEM bilayers and metal deposition time. In addition, the width of nanowires can be changed by using membranes with different sized pores.

Elemental analysis of the wires was done using energy dispersive spectroscopy (EDS). The EDS spectra, in Figure 3.4, showed a strong nickel peak, along with other elements from background. There was also a small carbon peak showing the presence of the polyelectrolytes. For comparison a background spectrum was also taken where both the nickel and copper peaks were absent. Also the control experiments gave indirect evidence for the presence of carbon, in the form of polyelectrolytes that support the nickel nanowires. Since there were no nanowires observed without polyelectrolytes bilayer deposition step.

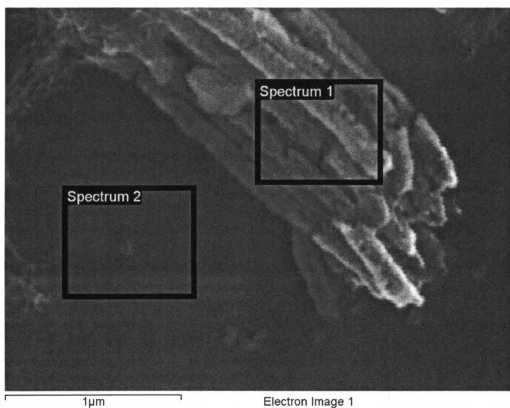


Figure 3.4: SEM image showing the two regions where EDS spectra were obtained, on the sample and on the background. The sample spectrum as shown in next page has nickel and carbon peaks, showing presence of nickel from electroless deposition and carbon as polyelectrolytes, which were absent in background spectrum (continued).

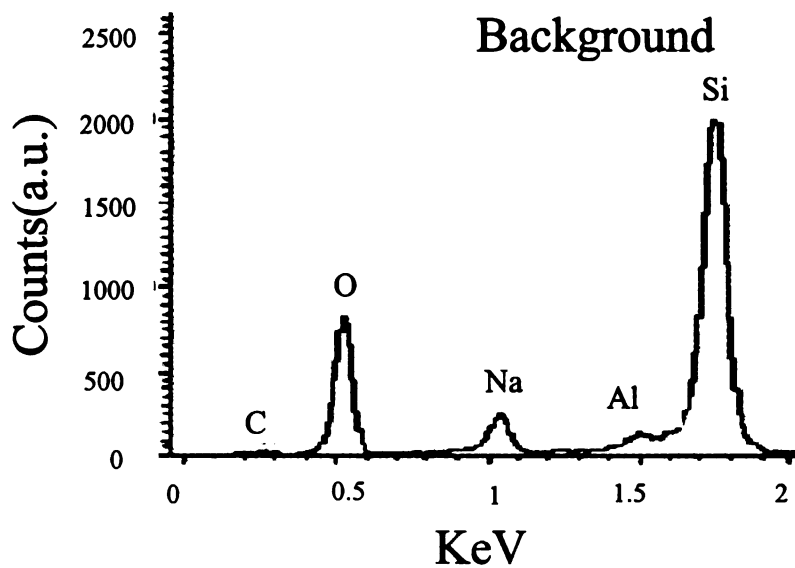
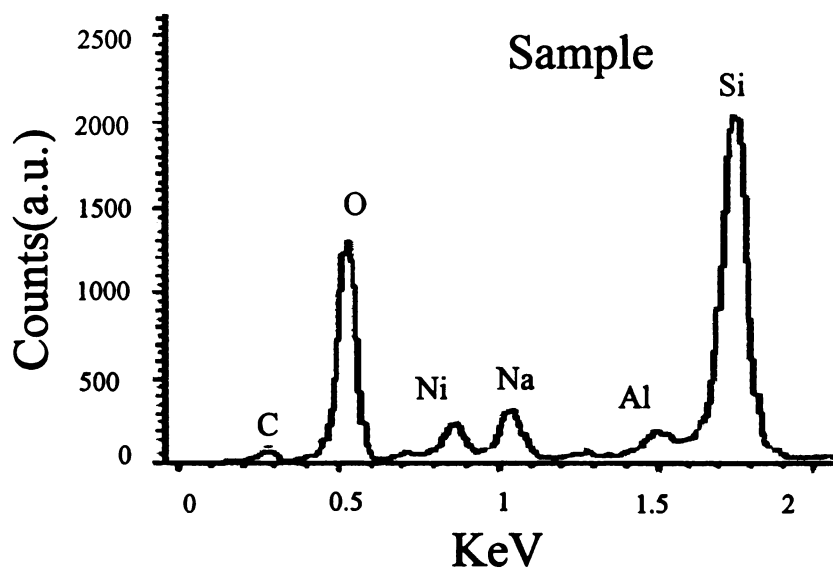


Figure 3.4 continued: Spectrum of nickel nanowires and background. Ni peak are visible in sample but are absent in background spectrum.

3.4 CONCLUSIONS AND FUTURE WORK

Here we have demonstrated the step-edge like fabrication of nickel nanowires. This is an easy technique to produce nanowires that does not require an elaborate set-up and with a large amount of equipment. It can readily be extended to different metals which can be electrolessly deposited. These nanowires are supported by polyelectrolyte bilayers as base which makes these wires flexible as they have polyelectrolytes multilayers as support. These nanowires can possibly be printed on polymeric substrates to achieve a printed nanowire array structure. Also it imparts functional anisotropy to the composition of wires where one side is metal and other side polymer.

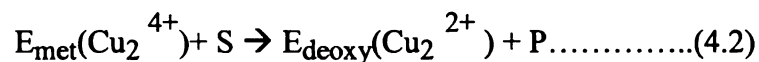
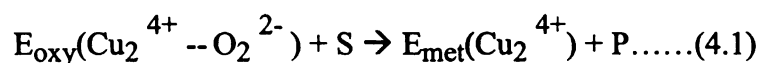
This has the added advantage of the ability to have two different molecules adsorbed on single nanowires by functionalizing different sides of the nanowires. Additionally bimetallic nanowires can easily be created by depositing a second metal on top of the first.

4 HIGH SENSITIVITY TYROSINASE BIOSENSOR USING LBL DEPOSITION

4.1 INTRODUCTION

Tyrosinase is a multi-copper oxygenase and is derived from *Streptomyces glaucescens*, the fungi *Neurospora crassa* and *Agaricus bisporus*. Tyrosinase contains a coupled binuclear copper active site and it catalyzes both the ortho-hydroxylation of monophenols and the two-electron oxidation of o-diphenols to o-quinones. The fungal tyrosinase is not a membrane protein unlike the human tyrosinase that is a membrane protein. Tyrosinase has adapted itself to various physiological conditions, in fungi and humans it catalyzes the first step for formation of melanine from tyrosine. Whereas in plants it causes oxidation of various phenolic derivatives [79, 80].

Tyrosinase in its native form occurs in inactive *met*-form where the binuclear copper site is in the wrong oxidation state [Cu(II)] to bind dioxygen. Two-electron reduction by a catechol converts *met*-tyrosinase to *deoxy*-tyrosinase, which then binds with dioxygen to give *oxy*-tyrosinase. Oxidation of a catechol leads to *met*-tyrosinase, which cannot bind oxygen to regenerate *oxy*-tyrosinase. Only in the presence of a second catechol molecule is the *met*-tyrosinase reduced to *deoxy*-tyrosinase which then regenerates the *oxy* form [81]. The catecholase activity of Tyrosinase can thus be described as



Where S is catechol molecule and P is quinone molecule.

Tyrosinase from *A. bioprus* is a heterotetramer with heavy and light chains with molecular weight of around 120 kDa. Tyrosinase enzyme has three domains, of which the central domain contains two Cu binding sites, called Cu_A and Cu_B. After comparing sequences from different sources, the only conserved domain seems to be the central copper-binding domain, which also shares sequence homology with hemocyanins (Hcs). Six conserved histidine residues which bind with a pair of copper ions in the active site of the enzyme tyrosinase. This active side interacts with both molecular oxygen and its phenolic substrate. The stability of protein is also determined by the location of cysteine (cys). The number of Cys residues varies from one organism to another, as along the N-terminal and central part of the protein, human and mouse tyrosinases have 17 Cys residues and plants have 11, whereas the C-terminal domain contains 1 Cys residue [82].

Immobilization is the most important step in application of biocatalyses and biosensors. There exists several paper discussing methodology to immobilize tyrosinase in active conformation and then measure its activity. Further such methods are mainly based on chemical and physical mechanisms [83]. One of the most commonly used methods is by modifying electrode surface to impart amine groups and then using glutaraldehyde to immobilize tyrosinase on it. This is an efficient method to immobilize enzymes without making it loose much of its activity [84-86]. Other method involves

using sol-gel method [87, 88] and also by forming pellets of graphite-teflon and Tyrosinase [89].

In this chapter we utilize layer-by-layer deposition technique [27], commonly abbreviated as LBL deposition technique, to deposit multilayers of tyrosinase. LBL deposition technique, developed by Decher in early nineties, used electrostatic interaction between oppositely charged surface and the polyelectrolytes in solution for layer by layer adsorption of polyelectrolytes on the surface. It is done on a surface having certain charge, positive or negative, and it is followed by dipping in solution containing oppositely charged species. This oppositely charged species adsorbs itself onto the surface and also leads to the charge reversal. Loosely bound molecules are removed by washing in water and then it is followed by dipping the surface with one adsorbed species into a solution containing oppositely charged species. This process is repeated to form multilayer of these polyelectrolytes. We exploit net negative charge on the enzymes for its adsorption on positively charged surface. As LBL deposition does not have any covalent attachments so it should lead to more active immobilization onto the surface. Also due to the versatility of LBL deposition technique we were able to fabricate various architectures which in turn led to very high sensitivity for catechol sensor.

4.2 EXPERIMENTAL SECTION

4.2.1 Materials

Thioctic acid, poly-L-lysine (PLL) (molecular weight ~ 15,000), tyrosinase (Tyr), sodium phosphate (monobasic and dibasic), cystamine, gold chloride trihydrate, hydroxylamine, sodium citrate dihydrate, sulfonated polystyrene (Mw~70,000), Poly(dimethyldiallyl amonium chloride (PDAC, Mw~100,000) were purchased from Sigma. Polyallyl amine hydrochloride (PAH, Mw~60000) were purchased from Polysciences, Inc. Silver membranes and copper grid for Transmission Electron Microscopy (TEM) were purchased from SPI supplies. Multiwalled carbon nanotubes (8-15 nm diameter, 0.5-2 μ m in length) from Cheaptubes, Inc. Ultrapure water (18.2M Ω) was supplied by a Nanopure-UV four-stage purifier (Barnstead International, Dubuque, IA); the purifier was equipped with a UV source and a final 0.2 μ m filter.

4.2.2 Preparation of Au nanoparticles

Gold nanoparticles were prepared by the standard procedure of reduction of gold salt by sodium citrate. 500 mL of 1 mM HAuCl₄ was brought to a rolling boil with vigorous stirring. Rapid addition of 50 mL of 38.8 mM sodium citrate to the vortex of the solution resulted in a color change from pale yellow to burgundy. Boiling was continued for 10 minutes; the heating mantle was then removed, and stirring was continued for an additional 15 minutes [56].

4.2.3 Modification of multiwalled carbon nanotubes

Multiwalled carbon nanotubes (MWCNTs) are hydrophobic in nature. Consequently to disperse them in aqueous solution, 1 mg/ml of MWCNTs was tip-

sonicated in 1 mg/ml of sulfonated polystyrene (SPS) for 30 minutes. The suspension was filtered through 220 nm membranes and filtrate was collected and redispersed in de-ionized water. This process of washing was repeated twice to get rid of free and loosely bound polyelectrolyte. Then 0.5 mg/ml of poly-lysine was added and again sonicated for 30 minutes followed by three washings. The polyelectrolyte coating were characterized by Transmission Electron Microscopy and by measuring the zeta potential of coated nanotubes. PDAC coated MWCNTs were prepared by dispersing SPS coated MWCNTs in 10 mM solution of PDAC sonicated for 30 minutes and followed by 3 washings.

4.2.4 Enzyme loading onto gold slides and silver membranes

Commercially available evaporated gold coated silicon wafers were cleaned in Piranha (70% Sulfuric Acid and 30% Hydrogen Peroxide) solution for 20 seconds. This was followed by thorough washing of gold with copious amount of de-ionized (DI) water and ethanol. After cleaning the gold slides were dipped in 5mM amine terminated alkanethiol (cystamine) in ethanol for 30 mins. Monolayer of cystamine molecules forms on the gold surface. These amine groups impart positive charge over which negatively charged tyrosinase (Tyr) was adsorbed by dipping modified gold slides into a solution of tyrosinase in deionized water (0.25mg/ml). In other case before dipping cystamine (Cys) modified gold electrode in the tyrosinase solution; the electrode was dipped in gold nanoparticle (AuNPs) solution for 30 mins, washed and then dipped in tyrosinase solution.

For other architectures, Piranha cleaned gold slides were dipped in 10 mM Lipoic acid in ethanol for 30 mins. This was followed by layer-by-layer (LBL) deposition of 0.2 mg/ml of poly-L-lysine (PLL) in phosphate buffer (pH=8.4) and tyrosinase (Tyr) in

deionized water. LBL was done by alternative dipping of thioctic acid modified gold electrode in as shown in Figure 4.1a. Instead of using polyelectrolytes, PLL coated MWCNTs (fMWCNTs) were used for layer-by-layer self assembly using enzyme and fMWCNTs as shown in Figure 4.1b. In another immobilization scheme polymer nanospears, as fabricated in chapter 2, were coated with polyallyl amine hydrochloride (PAH) to impart positive charge. A self assembled monolayer of cystamine was formed on the gold slide. PAH coated nanospears were dropped on the cystamine modified gold electrode and crosslinked onto the surface using glutaraldehyde. Over this a monolayer of Tyr was adsorbed by electrostatic interaction by dipping nanospears modified gold electrode in a solution of Tyr. The whole procedure is illustrated in Figure 4.1c

In final architecture instead of gold slides, commercially available silver membrane with pore size of 5 μm was used. Silver membrane behaves similar to gold electrode with respect to self-assembled monolayers formed by thiol terminated compounds. Silver membranes were cleaned by plasma cleaner for 10 mins. They were dipped in 10 mM lipoic acid in ethanol. The membranes was washed with ethanol and dried with nitrogen. This was followed by LBL deposition of PLL and Tyr. A Scanning electron micrograph of the silver membrane is shown in Figure 4.1d.

4.2.5 Amperometric i-t curves

Amperometric i-t studies were done using CHI-instruments. The enzyme loaded gold electrodes were used as working electrode and it was maintained at -100 mV against an Ag/AgCl reference electrode. A three electrode system was used and all the electrodes were dipped in 125 ml of 100mM phosphate buffer at pH=7. Then catechol was used as a

analyte and a step current was observed for each addition of 8 μ M of catechol in bulk. The current response was studied for various architectures.

4.2.6 Cyclic Voltammetry

Silver electrodes used were porous structure with larger surface area per unit projected area. So to determine the effective surface area cyclic voltammetry was carried out in nitrogen purged 0.5M sodium sulfate solution in DI water. Scans were obtained at scan rate of 0.1 V/s and range of scan was -0.35V to +0.15 V.

4.2.7 UV-Vis absorbance spectroscopy

UV-vis absorbance spectroscopy was used to determine the enzyme loading onto the electrode. Different enzyme concentration was added to 5 mM catechol solution in 100 mM sodium phosphate buffer at pH=6.5 and reaction was allowed to continue for 10 minutes and then the absorbance was measured at 380 nm. This was used to make calibration plot. Amount of enzymes onto electrode was determined by immersing electrodes in 5 mM catechol for 10 minutes and measuring absorbance at 380 nm. SP-890 UV-Vis Turner Spectrophotometer was used for the experiment.

4.2.8 Microscopy

Scanning Electron Microscopy (SEM) was done on LBL deposited modified carbon nanotubes on gold electrode and as received silver membrane. No sputter coating with gold or osmium was needed and SEM used for high resolution imaging was JEOL 6300F with field emission. TEM was done by coating copper grid with holey carbon film and drying small amount of suspended pure or functionalized carbon nanotubes. Microscope used was JEOL 2200FS 200 kV field emission TEM. The above mentioned microscopes were located at Centre of Advanced Microscopy, MSU.

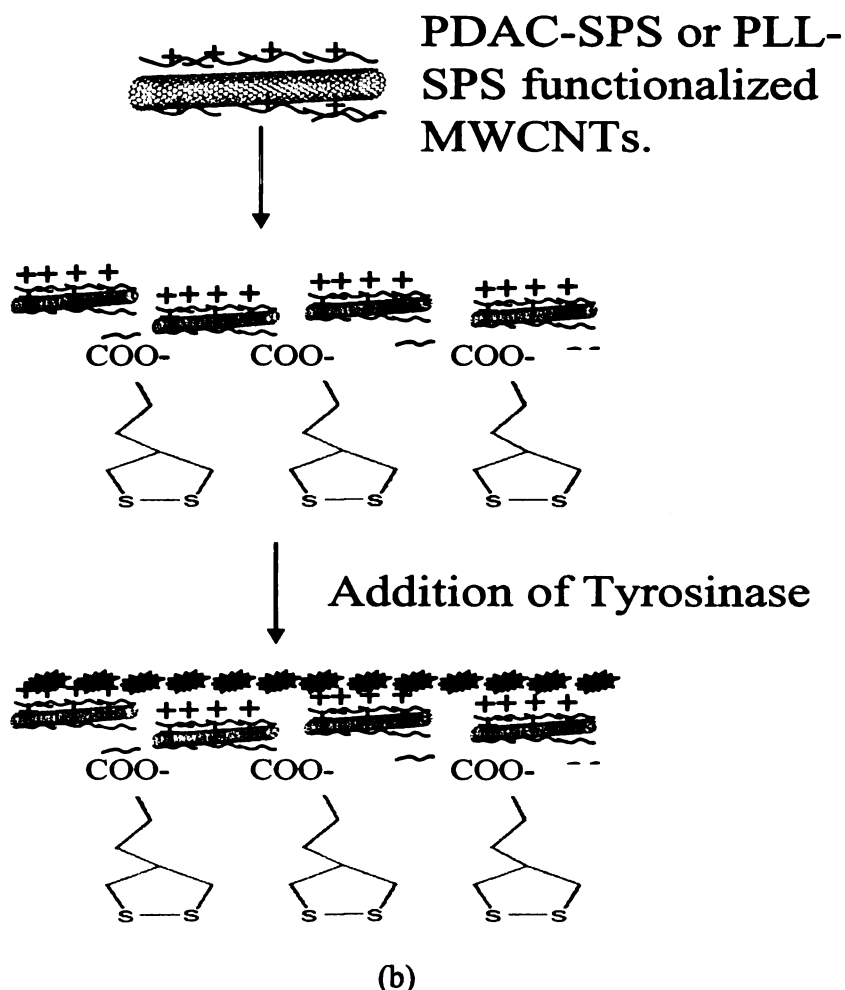
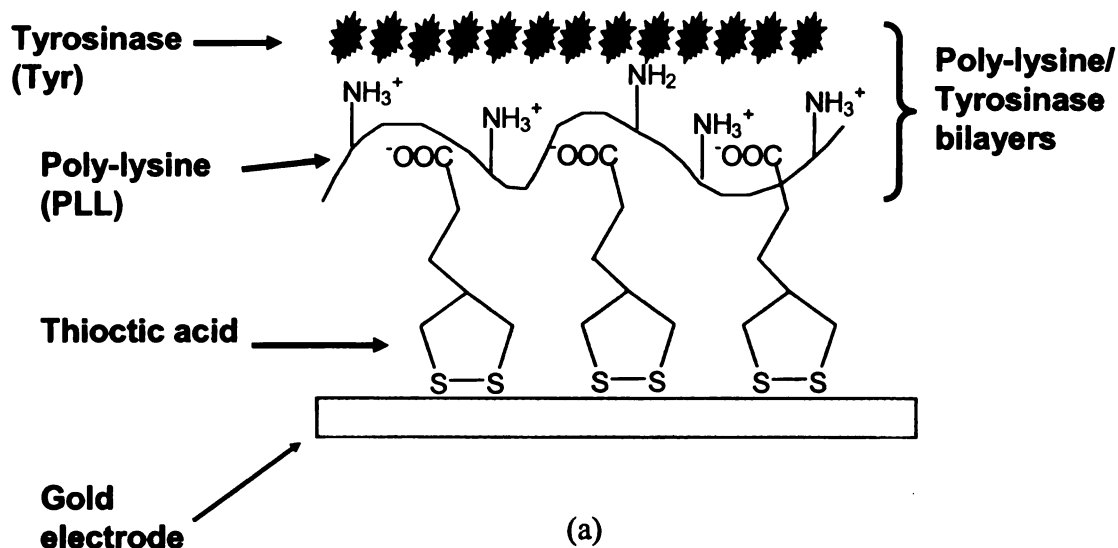
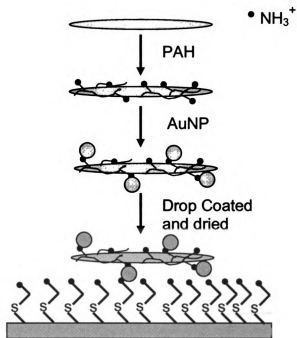
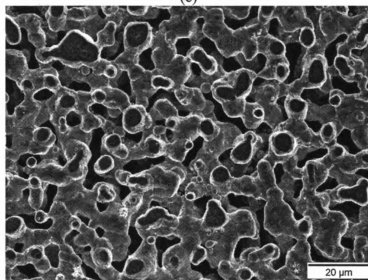


Figure 4.1: Different architectures for catechol sensor: (a) Thioctic acid modified gold electrode and layer-by-layer (LBL) deposition of tyrosinase and poly-lysine, (b) same as (a) but functionalized multiwalled carbon nanotubes instead of poly-lysine (continued).



(c)



(d)

Figure 4.1: (c) Polymer nanospheres drop coated and cross-linked onto cystamine modified electrode and then a layer of tyrosinase adsorbed over it, and (d) Scanning electron micrograph of silver membranes used for tyrosinase and poly-lysine deposition using LBL deposition.

4.3 RESULTS AND DISCUSSIONS

4.3.1 Layer-by-Layer of Poly-L-Lysine and Tyrosinase

The current response for the biosensor showed very less reaction time with almost a step response on the addition of catechol as shown in Figure 4.2.

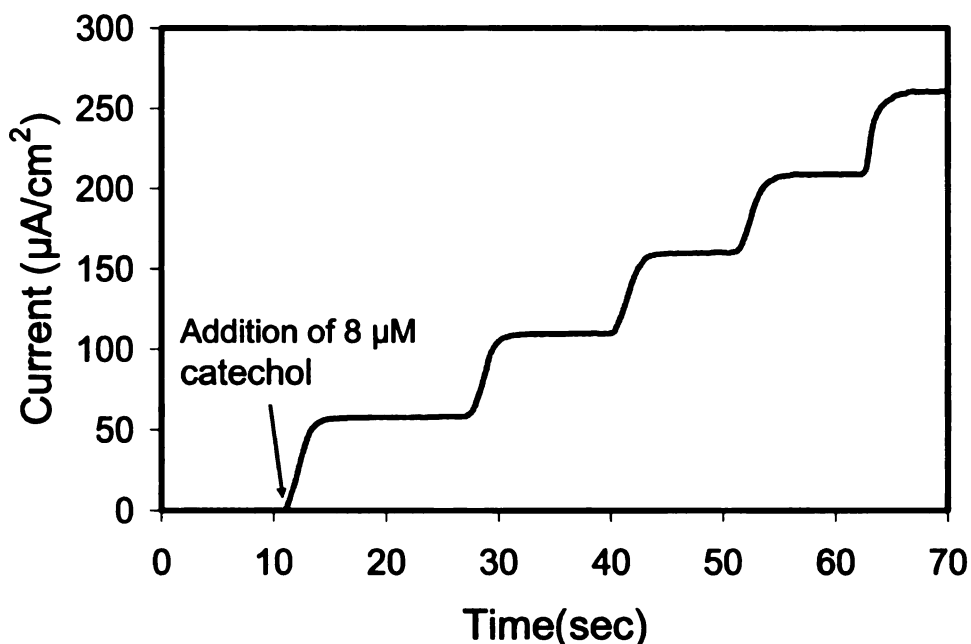


Figure 4.2: Tyrosinase biosensor for catechol as substrate, the electrode was maintained at $-0.1V$ vs $Ag/AgCl$ as reference electrode. Each step is aliquot of catechol added to achieve final concentration of $8 \mu M$ in bulk.

On the architectures based on gold slides, the best response was observed for PLL- Tyr bilayer system. As shown in Figure 4.3 the sensitivity increased as the number of bilayer increased but after 6 bilayers it reached a plateau. This is due to the process now becoming diffusion limited as additional number of layer of enzymes does not enhance the sensitivity. This implies that the process is now limited by flux of quinone to the electrode through the enzyme layer, rather than the kinetics of the system. The build up of bilayers was also characterized by Fourier transform infrared (FTIR) spectroscopy.

The addition of each layer increased the peaks of strong absorption at 1665 cm^{-1} (C=O stretching of amide group), 1540 cm^{-1} for N-H bending mode and 3300 cm^{-1} for N-H stretching mode as shown in Figure 4.4.

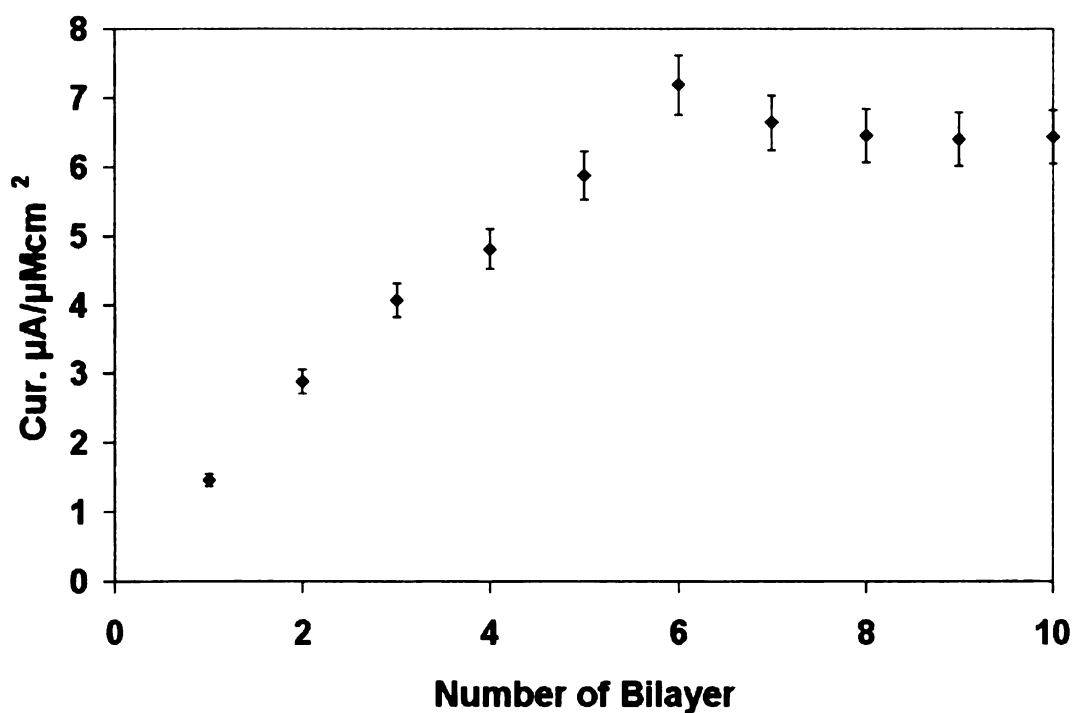


Figure 4.3: Bilayer versus Current sensitivity plot for PLL-Tyr biosensor. The sensitivity with different number of bilayers increased till 6 bilayers and then dropped and stabilized.

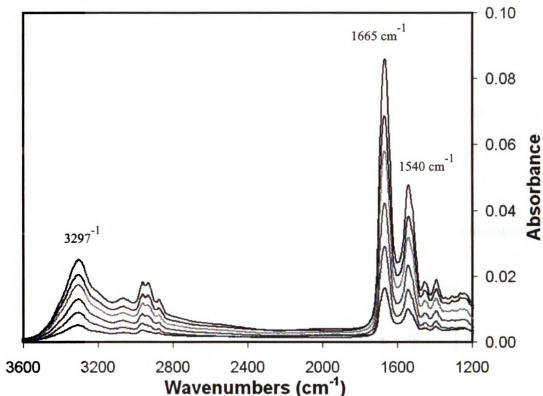


Figure 4.4: FTIR spectra after each layer: 1665 cm^{-1} (C=O stretching of amide group), 1540 cm^{-1} for N-H bending mode and 3300 cm^{-1} for N-H stretching mode.

4.3.2 Incorporation of Multiwalled Carbon Nanotubes

As the process became diffusion limited at higher number of bilayers, a scheme was developed where MWCNTs were functionalized with polyelectrolytes. We postulated that if we can incorporate a conducting path by putting MWCNTs through the enzyme layer it might increase the sensitivity or shift the saturation of biosensor to higher number of bilayers. Functionalization was necessary as pure nanotubes are inherently hydrophobic. So it is required to modify carbon nanotubes to achieve two properties. Firstly, to make the carbon nanotubes hydrophilic as enzymes and hence, biosensors work in aqueous media. Secondly, we needed a way to deposit nanotubes on the surface of the electrode using LBL deposition technique. Hence, Sulfonated polystyrene (SPS)

was used as first layer as SPS adsorbs readily on the carbon nanotubes and also imparts strong negative charge on the surface.

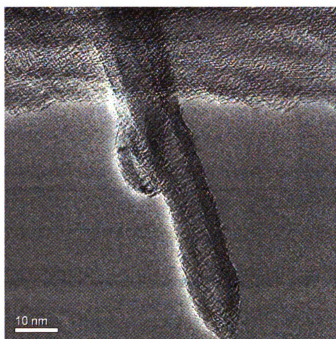
Therefore, MWCNTs were coated with SPS and its zeta potential shifted to a negative value. Then these SPS-MWCNTs were coated with PLL to get positively charged fMWCNTs for layer by layer self assembly. The shift in zeta potentials is given in Table 4.1.

Table 4.1 Zeta potential of polyelectrolyte coated multiwalled carbon nanotubes

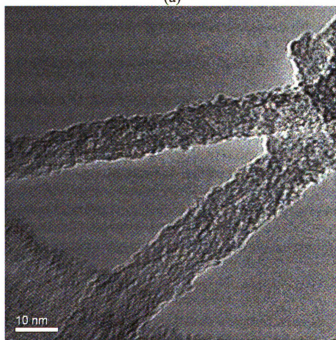
MWCNTs	Zeta Potential (mV)
SPS coated	-49.00 ± 89
PLL-SPS-coated	46.36 ± 1.68
PDAC-SPS-Coated	53.85 ± 1.31

TEM was also done to qualitatively show the coating of MWCNTs. Figure 4.5a is a TEM micrograph of pure MWCNTs and Figure 4.5b shows the micrograph of coated fMWCNTs. As it can be seen the surface of fMWCNTs is much rougher than pure MWCNTs. The comparative sensitivities for initial system and new system at high number of bilayers are shown in Figure 4.6. As seen in figure there is not significant difference in the sensitivity. It was also studied for the response at lower number of bilayers and response was similar (data not shown). As it can be seen the sensitivity does not increase with addition of carbon nanotubes with PLL-Tyr system. Hence addition of CNTs is not advantageous in this system. One of the possible reasons for this is that the diffusional resistance for initial PLL-Tyr system is already reduced due to the porous bilayer structure of PLL-Tyr system. This was observed by Katz et al, where they showed

PLL forms porous bilayers and hence offers less resistance for the redox species diffusing through the bilayers [90].



(a)



(b)

Figure 4.5 a) TEM of pure multiwalled carbon nanotube and b) polyelectrolyte coated MWCNTs.

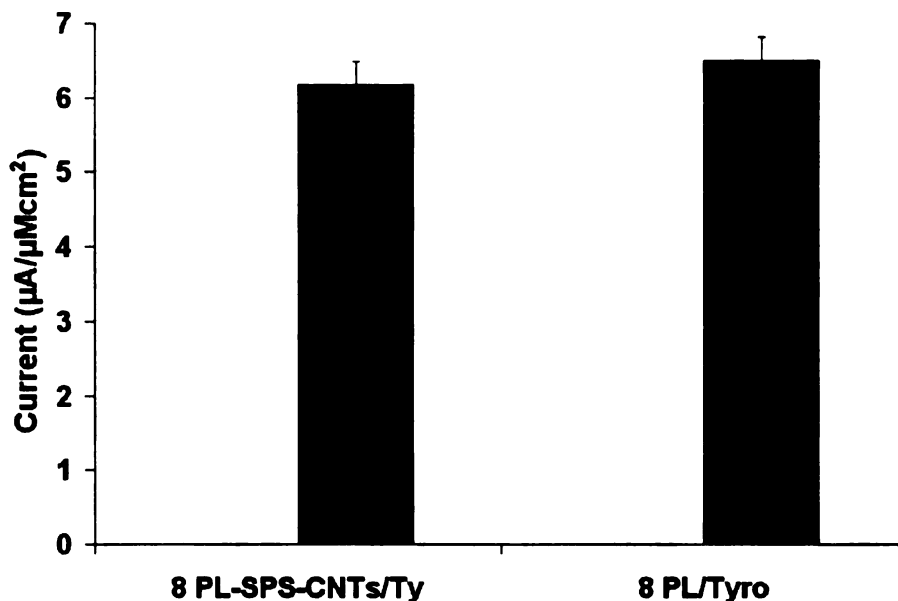
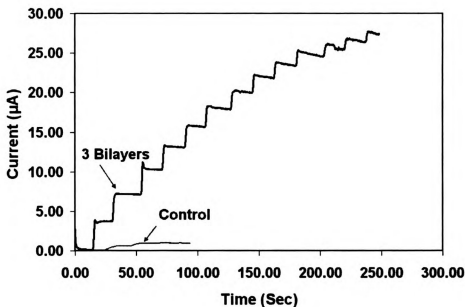
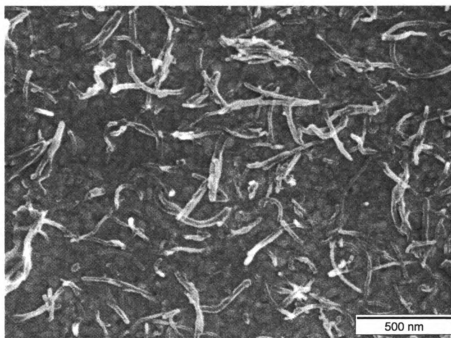


Figure 4.6: Comparative plot of sensitivity for PLL coated MWCNTs and pure PLL tyrosinase LBL system.

Additional experiment were also carried out, where a strong polyelectrolyte, Poly(diallyl dimethyl ammonium chloride) (PDAC) was used instead of PLL. PDAC is a strong polyelectrolyte and should form a uniform layer on the surface and should offer more diffusional resistance to diffusion of quinone to the electrode. In comparison a similar system with PDAC-SPS coated MWCNTs were prepared and their zeta potentials are tabulated in Table 3.1. Architectures of both, PDAC-Tyr bilayers and PDAC-MWCNTs-Tyr were studied for their sensitivities and response as shown in Figure 4.7a. Figure 4.7b is a SEM image of PDAC-MWCNTs deposited by LBL technique.



(a)



(b)

Figure 4.7: (a) Comparative response curve for 3 bilayers of PDAC coated MWCNTs/Tyrosinase and pure PDAC/Tyrosinase (Control) system, the difference in sensitivity was significant, (b) SEM image of LBL fMWCNTs on electrode.

In this case, PDAC-MWCNTs containing biosensor yielded higher sensitivity as compared to PDAC-Tyr system, though the overall sensitivity was much lower when compared to other systems that were studied. The architecture with immobilized polymer nanospheres also showed lesser sensitivity as compared to PLL-Tyr system as there was not sufficient enzyme loading and polymer nanoparticles do not enhance conductivity of the bilayers as well.

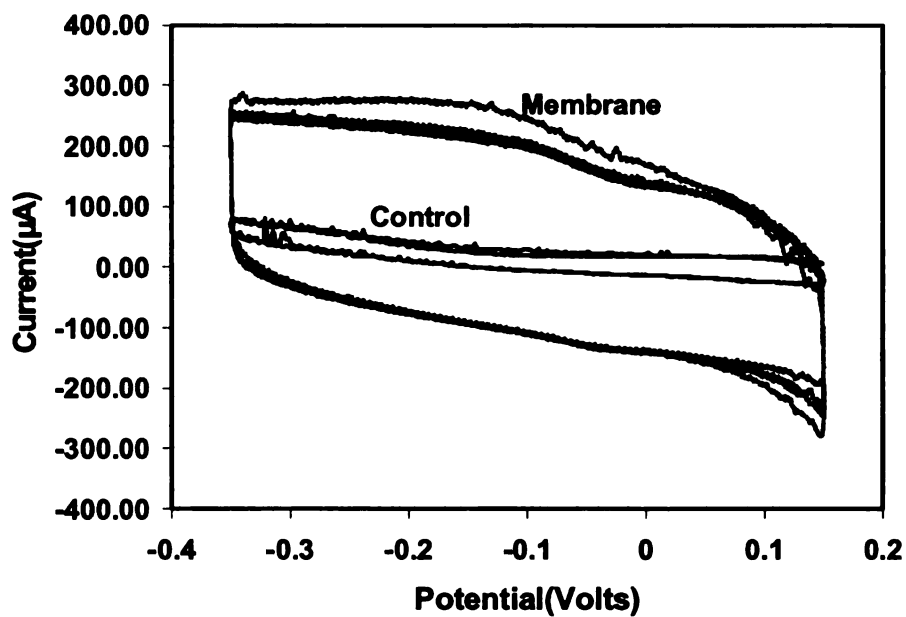
4.3.3 Silver membrane as electrode

Another architecture used a commercially available porous silver membrane as electrode. As gold and silver has similar behavior towards the self-assembled thiol-terminated monolayers. The same scheme was used as the one used for gold electrode. The silver electrode are stable at the potential and pH range we test the electrode for biosensor. As the silver electrode has porous structure, the amount of electroactive area for a unit projected area is greater than the planar electrode. The effective electroactive area was estimated by obtaining a cyclic voltammogram of porous silver electrode and a planar silver electrode in 0.5M sodium sulfate at a scan rate 0.1V/s. The voltammogram was obtained for blank silver porous electrode and planar electrode is shown in Figure 4.8a. As the charging current is directly proportional to the product of the area of the electrode and the scan rate, it can be used to determine the surface area of porous electrode. The ratio of average charging current for a porous and planar electrode gives the ratio of area of porous and planar electrode. It was approximately 3. So there is 3 times more active surface area in a porous electrode as compared to planar electrode.

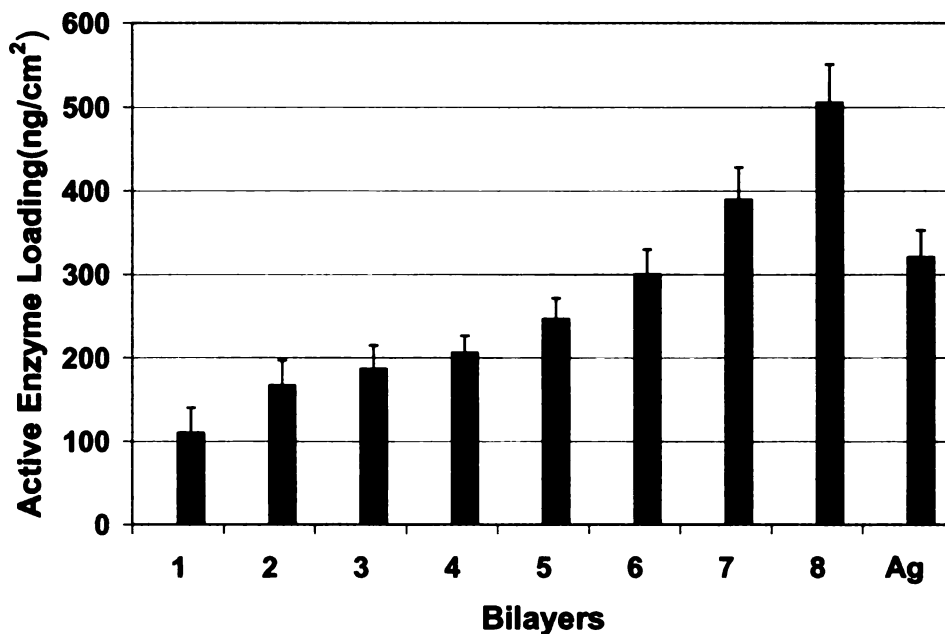
Enzyme loading for each bilayer was determined using UV-vis absorbance. Different amounts or units of tyrosinase were added to a fixed volume (2 ml) of 5 mM

catechol solution. The reaction was allowed to continue for 10 minutes, where catechol was oxidized to quinone and the absorbance was measured at 380 nm. The calibration plot was made by measuring absorbance for quinone with known quantity of enzymes added to catechol solution. This was followed by measuring absorbance for quinone for solution with various electrodes immersed in the catechol solution for 10 minutes. This gives the amount of equivalent active enzyme loading on the various electrodes. The plot of enzyme loading versus number of bilayers and on silver membrane is given by Figure 4.8b.

Figure 4.8b shows increase in enzyme loading as number of bilayers increased though the amount of enzyme loading increased beyond six bilayers but the current saturates, as was shown in Figure 4.3, after certain number of bilayers because of diffusion limitation of quinone that was produced in the enzymatic layer. It implies the catechol that is oxidized to quinone has to diffuse through the enzyme layer before it gets converted to catechol by the electrode. Though the amount of enzyme is increased at the interface the current saturates because of diffusion limitation of quinone to electrode.



(a)



(b)

Figure 4.8: (a) Cyclic voltammogram of a silver planar as a control electrode and porous silver membrane as electrode in 0.5M Na₂SO₄ purged with nitrogen at scan rate of 100 mV/s from -0.35V to +0.15V. (b) Amount of equivalent active enzyme loading on planar electrodes per unit area until 8 bilayers and on porous silver membrane. The amount of enzyme increased as number of bilayers increased.

Silver membrane electrode showed much larger enzyme loading than a planar electrode because of its porous nature, consequently showing maximum sensitivity as shown in Figure 4.10. This is due to higher enzyme loading as well as shorter diffusion distance for quinone to diffuse through to the electrode. The comparative current versus time response curve for most sensitive biosensor on planar electrode that corresponds to six bilayers of PLL-Tyr and sensor on silver membrane is given in Figure 4.9. The relative sensitivity plot for all the systems on planar electrode and silver membrane is given by Figure 4.10. The sensitivity for porous electrode was much higher than for six bilayers on planar electrode even though the tyrosinase loading was comparable. This is because 6 bilayers increases the distance between the site, where catechol is oxidized to quinone within the bilayers, and the electrode surface where actual potential is applied. Hence quinone has to diffuse larger distance before it could reach the electrode whereas on a porous electrode the diffusion distance is much lesser. This is illustrated in the scheme shown in Figure 4.11. Figure 4.11(a) shows the case where the enzyme loading is increased by increasing the number of bilayers and quinone (P) formed by catalysis of catechol (S) has to diffuse through the enzyme layer before it feels the potential applied on the electrode. Whereas in a higher surface area as shown in Figure 4.11(b) this diffusion distance is greatly reduced.

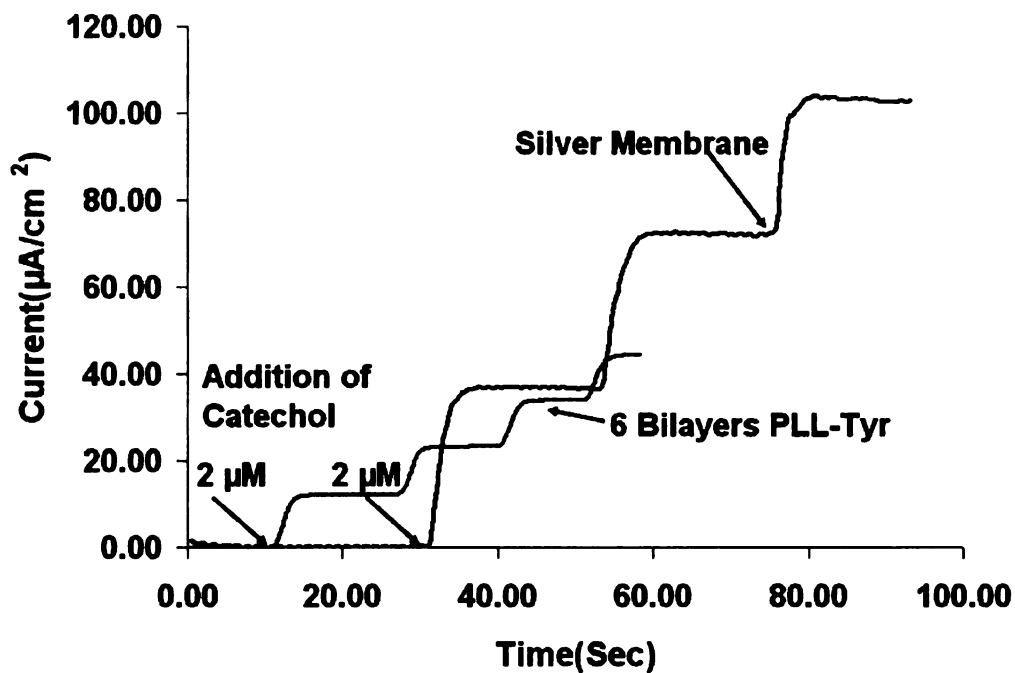


Figure 4.9: Comparative response curve for 6 Bilayer PLL-Tyr and catechol biosensor on porous silver membrane.

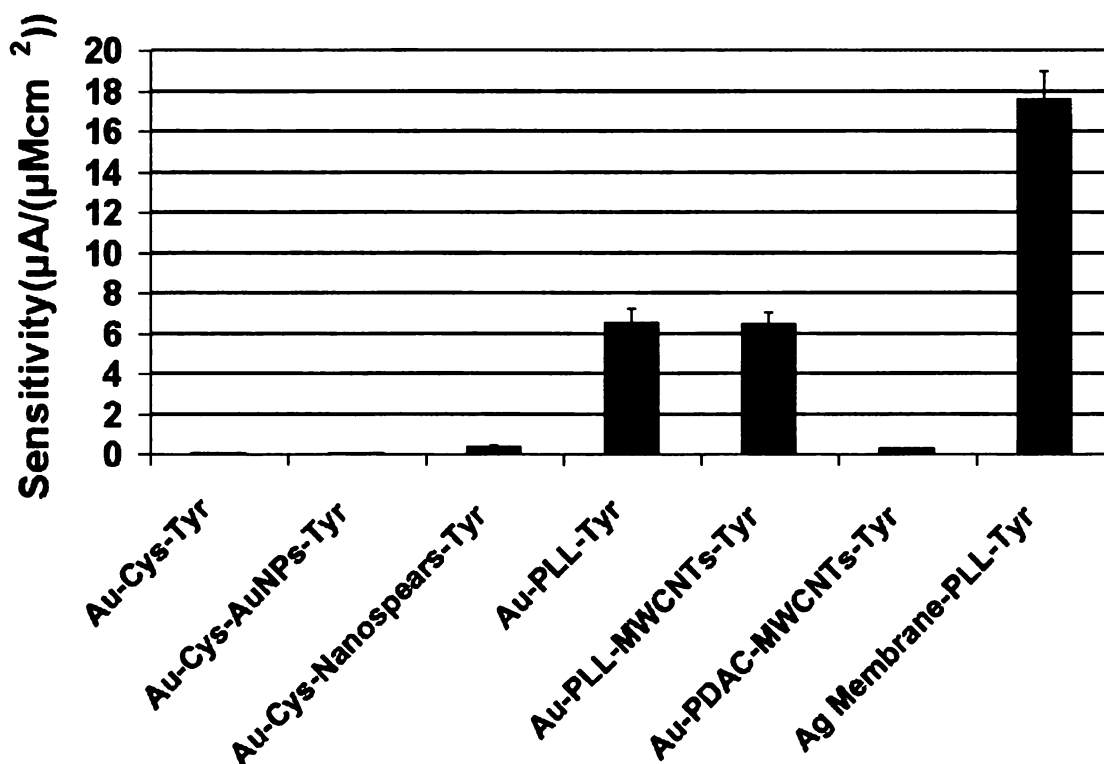
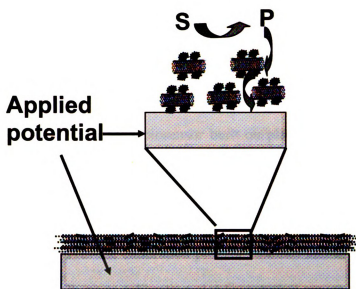
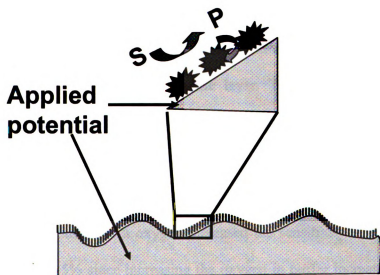


Figure 4.10: Comparative sensitivity plot for different architectures.



(a)



(b)

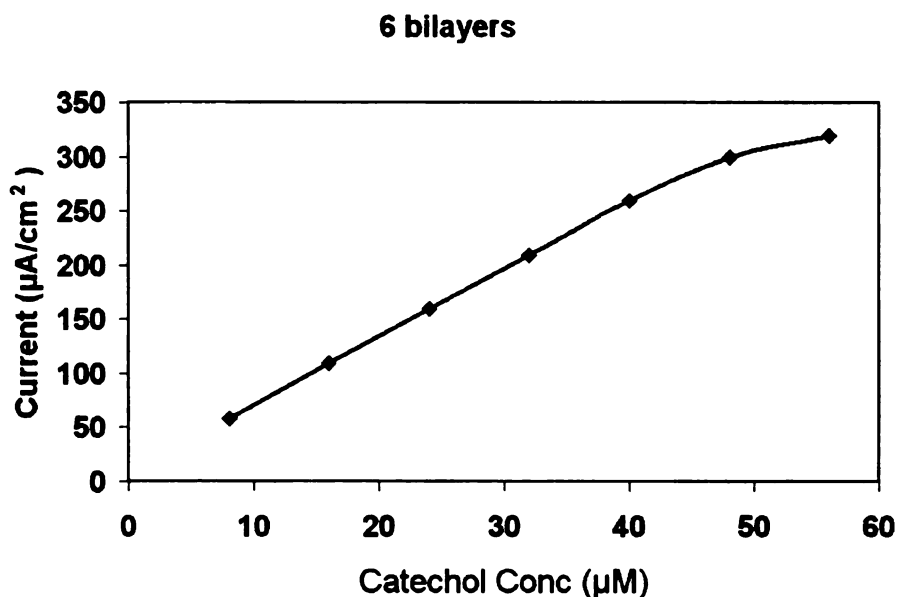
Figure 4.11: (a) Diffusion of quinone (P) through the enzyme layer on a planar electrode. The distance for quinone to diffuse to the electrode surface is much larger. (b) As compared to the other electrode, which has higher enzyme loading due the higher surface area while keeping the diffusion distance small (b).

It was also verified if the difference in sensitivity could be attributed to silver. It was done by making same biosensor by LBL deposition process on a planar silver electrode. Silver planar electrode was modified in the same manner as porous electrode and bilayers of PLL-Tyr were built. It was tested for its activity against catechol and sensitivity was found same as a biosensor built on planar gold electrode. Hence, there was no difference in sensitivity for a catechol sensor made on a planar silver or gold electrode.

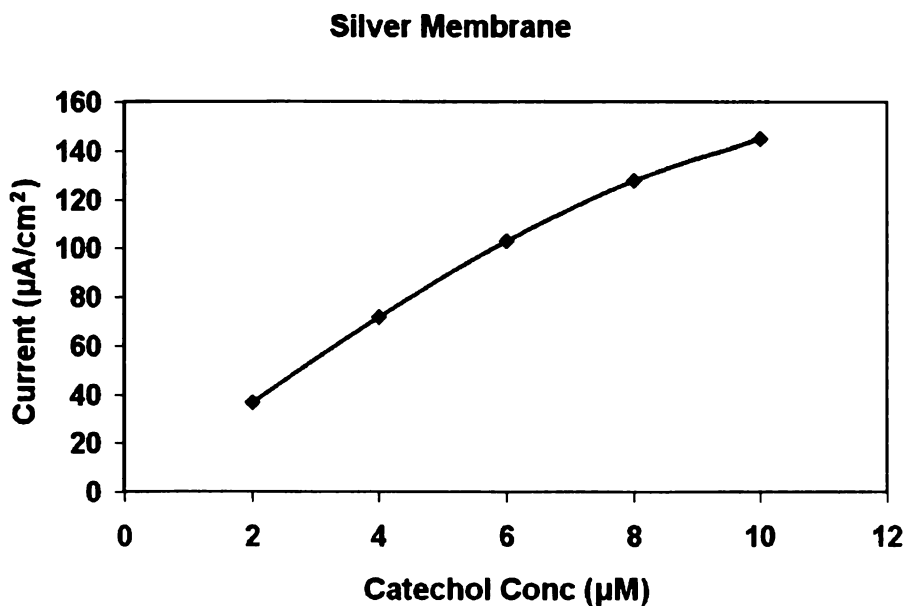
Figure 4.12a gives the calibration plot for catechol sensor for 6 bilayers PLL-Tyr sensor and Figure 4.12b gives calibration plot for catechol sensor on silver electrode. The calibration plot for 6 bilayer sensor had longer linear range from 8 μM to 40 μM and for sensor of silver electrode had linear range from 2 μM to 8 μM . This could be because the current density was very high at smaller concentration in silver membrane which could lead to depletion of oxygen in enzymatic layer. The number of bilayers on silver membrane was also increased but it did not increase the sensitivity (data not shown) possibly because of oxygen depletion in the enzymatic layer. As at such a high current, the rate the consumption of oxygen within the enzymatic layer is very high.

Purging the buffer with oxygen increased the sensitivity of biosensor on porous silver electrode by 25% since increasing the oxygen in buffer increased the oxygen flux to the electrode. Purging buffer with nitrogen decreased the sensitivity to negligible as tyrosinase could not be regenerated to oxy-tyrosinase state from the deoxy-tyrosinase state. This is because of absence of oxygen, retarding the regeneration of oxy-tyrosinase. Whereas on planar electrodes purging buffer with oxygen did not show any appreciable change in the sensitivity of the biosensor as sensitivity is governed more by diffusion of

quinone through the bilayers to the electrode. Oxygen is still present in sufficiently high concentration to not to limit the sensitivity.



(a)



(b)

Figure 4.12: Sensitivity plots for a) 6 bilayers of PLL-Tyr on planar gold and b) 1 layer of PLL-Tyr on porous silver electrode.

4.4 CONCLUSIONS AND FUTURE WORK

In this chapter we studied various architectures to fabricate catechol biosensor. A layer by layer approach was used which can easily be extended to various kinds of nanostructures. Poly-lysine-Tyr LBL self assembly architecture imparted highest sensitivity for biosensor response for planar electrodes and additional nanostructures did not impart better sensitivity. Though using high surface area supports like porous silver membrane can enhance higher sensitivity without making the whole response process diffusion limited. Also this process is versatile that can be extended to other form of electrodes like carbon based electrodes where this sensor was fabricated on a 96 well plate.

5 NEUROPATHY TARGET ESTERASE BIOSENSOR

5.1 INTRODUCTION

Neuropathy Target Esterase (NTE), is a membrane-bound proteins found in neurons of vertebrates [91-96], has been shown to be necessary for embryonic development in mice, and is believed to be involved in cell-signaling pathways and lipid trafficking. [91] NTE has serine esterase activity and can hydrolyze ester, peptide, and amide bonds. The nucleophilic serine residue (active site) of NTE attacks the carbonyl carbon atom of the substrate, forming a covalent acyl-enzyme intermediate, which is subsequently hydrolyzed. A consequence of this reaction mechanism is that the esterase activity of NTE is susceptible to covalent inhibition by Organophosphorus Esters (OPs) with which it forms an analogous phosphyl-enzyme intermediate. Irreversible binding of some OP compounds to the active serine site results in a debilitating neural disease known as (OP) Induced Delayed Neuropathy (OPIDN) [91]. Symptoms of OIPDN include flaccid paralysis of the lower limbs, which becomes evident two to three weeks after exposure to neuropathic OPs. Recovery from this disease is usually poor, and there is no specific treatment. Because NTE is difficult to produce for research purposes, research to study its esterase activity is typically done using a fragment of the NTE protein that contains the esterase activity and can be more easily produced. One such fragment, known as NEST,[93, 94, 97] reacts with esters and inhibitors in a manner very similar to NTE.

Because NTE plays a central role in both chemically induced and spontaneously occurring neurological diseases, approaches that can help measure its esterase activity

and inhibition are of tremendous scientific and commercial importance. Conventionally, the esterase activity of NTE (or NEST) is measured using two distinct steps. In the first step, a solution containing phenyl valerate is brought into contact with NEST or NTE protein solution, whose esterase activity reacts with a portion of the artificial substrate phenyl valerate to form phenol. In the second step, the concentration of phenol in the solution is determined either colorimetrically, in the presence of 4-amino antipyrine [98], or electrochemically, in the presence of tyrosinase enzyme [99, 100]. Tyrosinase converts phenol first to catechol and then to *o*-quinone, which can be measured electrochemically at an electrode [95]. The current generated by the electrode increases with the amount of *o*-quinone present, thus giving an indirect measurement of the amount of NTE esterase activity present during the first step. To test for esterase inhibition, this procedure is repeated both in the absence and presence of a putative inhibitor (e.g., an OP compound). A reduced signal indicates inhibition of the esterase activity. This method has the disadvantages of being slow, and requiring two steps, making it unsuitable for some important applications, such as high-throughput screening of compounds for NTE inhibition and continuous, on-line, environmental monitoring to detect chemical warfare agents that target NTE.

This work presents the first continuous, electrochemical biosensor for real-time, rapid measurement of NEST (or NTE) esterase activity. The biosensor was fabricated by co-immobilizing NEST protein and tyrosinase enzyme on an electrode using layer by layer assembly approach by Decher [27]. To our knowledge, this is the first time NEST has been immobilized in an active conformation on an electrode. Potential applications of this sensor include detecting the presence of chemical weapons that target NTE,

screening industrial and agricultural OP compounds for NTE inhibition, studying the fundamental reaction kinetics of NTE, and investigating the effect of NTE mutations found in Amyotrophic Lateral Sclerosis or Lou Gehrig's disease (ALS) patients on NTE's enzymatic properties.

5.2 EXPERIMENTAL SECTION

5.2.1 Materials

Thioctic acid, poly-L-lysine (PLL) (molecular weight ~ 15,000), tyrosinase (Tyr), sodium phosphate (monobasic and dibasic), ethylenediaminetetraacetic acid (EDTA), sodium chloride, 3-[(3-cholamidopropyl) dimethylammonio]-1-propanesulfonate (CHAPS) and isopropyl thiogalactoside (IPTG). Ultrapure water (18.2M Ω) was supplied by a Nanopure-UV four-stage purifier (Barnstead International, Dubuque, IA); the purifier was equipped with a UV source and a final 0.2 μ m filter.

5.2.2 NEST expression and purification

NEST was expressed and purified according to published procedures [93]. Briefly, DNA fragment encoding NEST was cloned into pET-21b vector, and the resulting expression vector was transformed into *E. coli* BL21 (DE3). An overnight culture of transformed *E. coli* was inoculated with M9 media containing ampicillin and grown in a fermentor. IPTG was added to the resulting cell culture after a day to induce the expression of NEST. The resulting cells were collected 4 h after induction by centrifugation and subjected to protein expression techniques. Briefly, 5 g of cell paste was suspended in 30 ml of PEN buffer (50mM sodium phosphate/0.3 M NaCl/0.5 mM EDTA, pH 7.8) containing 2% CHAPS and tip sonicated four times. The cell lysate was

These characteristics of tyrosinase were exploited by us to fabricate a NEST biosensor, capable of measuring the NEST's esterase activity and its inhibition, by co-immobilizing NEST and tyrosinase on a gold electrode using layer by layer assembly approach.

The molecular architecture of the biosensor interface is shown schematically in Figure 5.1. Gold electrodes cleaned in Piranha solution, were dipped in 5 mM solution of thiocetic acid in ethanol for 30 min. The electrodes were washed with ethanol, dried under nitrogen and dipped in PLL solution for 45 min. The PLL solution was prepared by adding 12 mg of poly-L-lysine in 50 mL of 20 mM phosphate buffer (pH 8.5). The electrodes were then rinsed with water and dipped in an aqueous solution of Tyrosinase (Tyr) (0.2 mg/ml) for 1 h. The last two steps were repeated varying number times to create PLL-Tyr bilayers with PLL being the topmost layer. The electrodes were washed with water and dipped in a solution of NEST protein (0.1 mg/ml) in 100 mM phosphate buffer, pH (7.0) for 1 h. The electrodes were then washed with water, dried under nitrogen and dipped in phosphate buffer (0.1 M, pH 7.0) for testing.

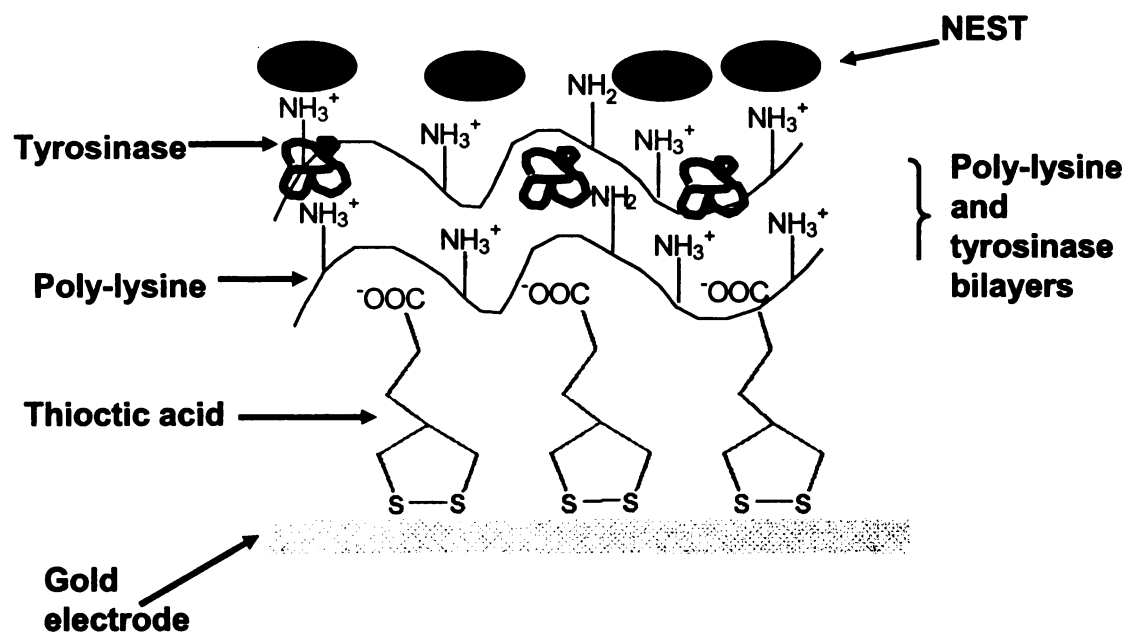


Figure 5.1: Molecular architecture of NEST biosensor

5.2.4 Preparation of phenyl valerate solution

To prepare phenyl valerate solution, 15 mg of phenyl valerate was dissolved in 1 mL of dimethylformamide (DMF), and 15 mL of water containing 0.03% Triton was added slowly under vigorous stirring. For potential step voltammetry experiments, small aliquots of the resulting phenyl valerate micellar solution (5.286 mM) were added to the phosphate buffer to obtain the desired concentrations.

5.2.5 Ellipsometry

Ellipsometric measurements were obtained with rotating analyzer ellipsometer (model M-44; J.A. Woollan Co. Inc., Lincoln, NE) using WVASE32 software. The thickness values for dried films were determined using 44 wavelengths between 414.0 and 736.1 nm. The angle of incidence was 75° for all experiments. Refractive indices of films containing PLL and proteins was assumed to be $n=1.5$, $k=0$. These optical constants

compare well with those determined for 4 bilayer films consisting of poly-L-lysine and tyrosinase using ellipsometry.

5.2.6 Potential step voltammetry and other measurements

The electrodes (sensors) were maintained at a potential of -100 mV (vs Ag/AgCl reference electrode) using a BAS CV-50W electrochemical analyzer. The esterase activity of NEST biosensor was monitored by measuring the output current for a variety of phenyl valerate concentrations, under stirred conditions. The NEST protein converts phenyl valerate to phenol, which gets converted to *o*-quinone by tyrosinase. The *o*-quinone gets reduced at the electrode's surface, resulting in the generation of current. The electroreduction of *o*-quinone produces catechol which again gets converted to *o*-quinone by tyrosinase, thus amplifying the signal.

To measure inhibition of the esterase activity, a known quantity of phenyl valerate was added to the phosphate buffer (pH 7.0), under stirred conditions. After the stabilization of current, a known amount of NEST inhibitor was added, and the resulting drop in current was measured.

5.3 RESULTS AND DISCUSSION

5.3.1 Ellipsometry

Ellipsometry were used to confirm the deposition of different layers that make up the NEST biosensor. As shown in Figure 5.2, the thickness increase following the addition of first PLL and Tyr bilayer was approximately 9.3 ± 0.4 nm. The thickness increase for the next two PLL-Tyr bilayers was the same and equal to approximately $7.2 \pm$

0.3 nm. The thickness increase following the addition of final PLL-NEST bilayer was approximately 6.6 ± 0.3 nm.

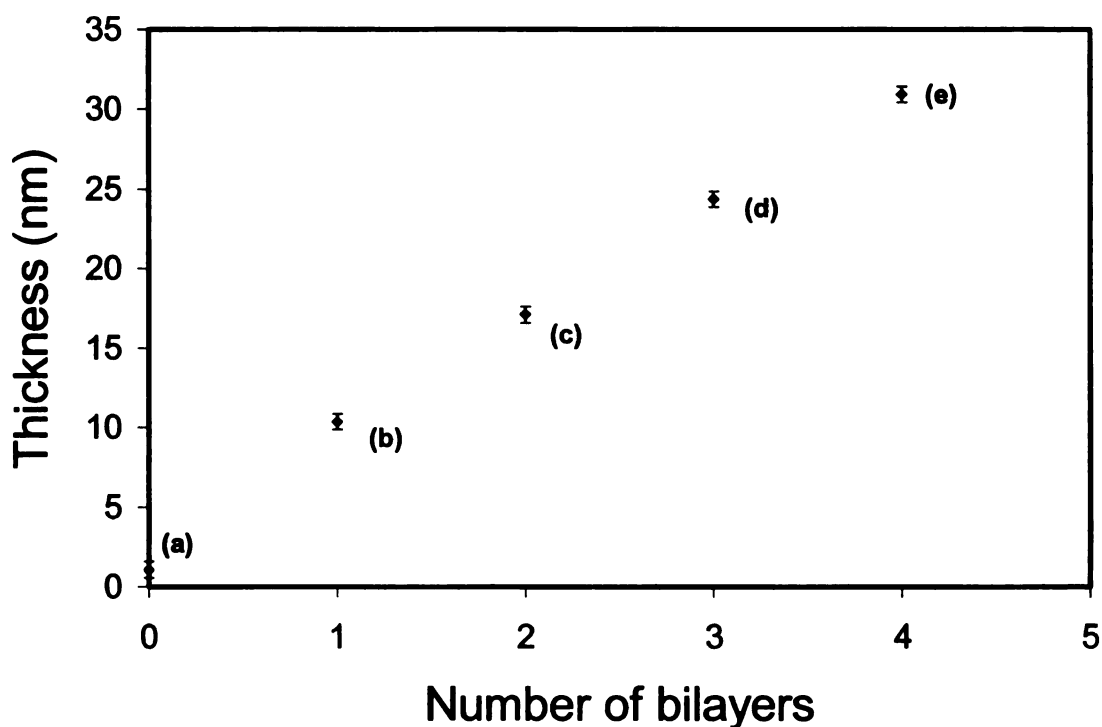


Figure 5.2: Ellipsometric thicknesses after the successive addition of following layers: thioctic acid (point a), PLL-Tyr first bilayer (point b), PLL-Tyr second bilayer (point c), PLL-Tyr third bilayer (point d), and PLL and NEST final bilayer (point e).

5.3.2 Dependence of current response on working potential and pH

The various experimental parameters (such as pH and applied potential), which can affect the amperometric determination of phenyl valerate, were optimized. The effect of applied potential on the amperometric response of the sensor was tested in the range between 0.05 and -0.20 V. Figure 5.3a illustrates the signal and background for the whole

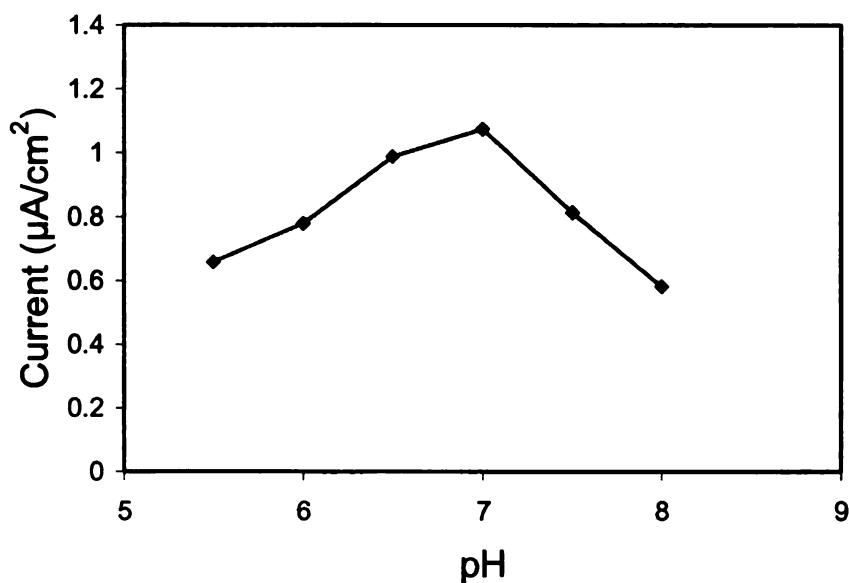
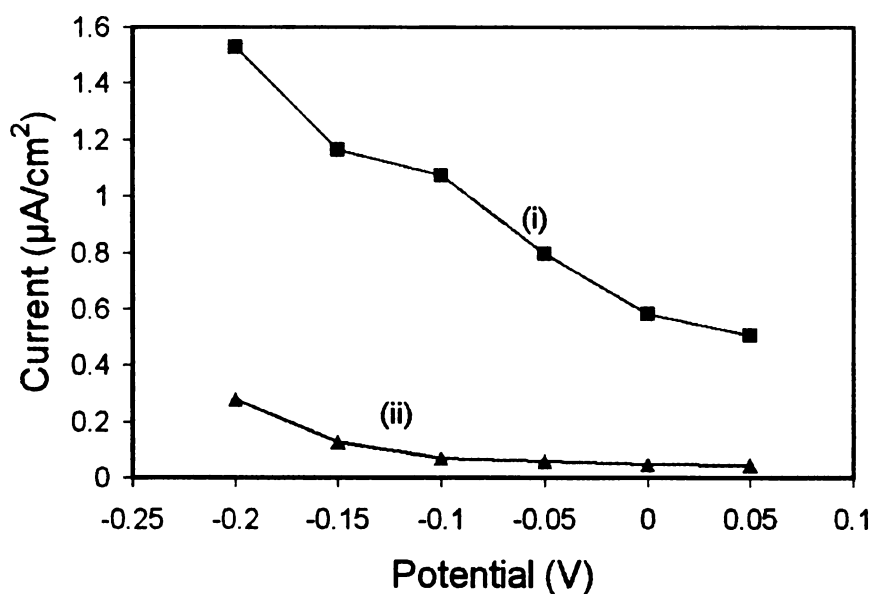
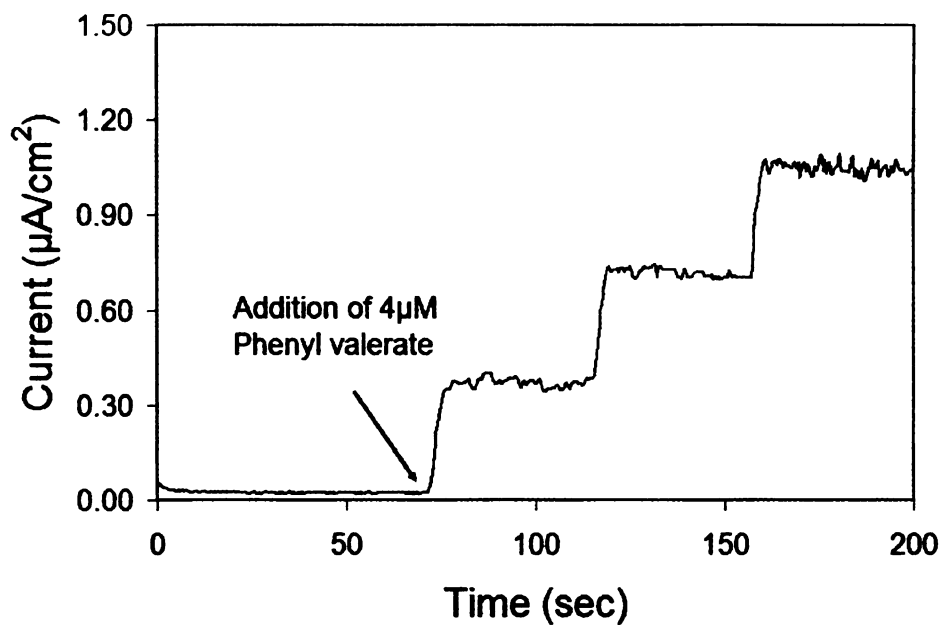


Figure 5.3: (a) Effect of working potential on the response current of the enzyme electrode in 0.1 M phosphate buffer (pH 7.0) with (i) and without (ii) 12 μ M phenyl valerate solution, in 0.1 M phosphate buffer at an applied potential of -0.1 V (vs Ag/AgCl). (b) Effect of pH on the response current of the electrode, in the presence of 12 μ M phenyl valerate solution, in 0.1 M phosphate buffer at an applied potential of -0.1V (vs Ag/AgCl).

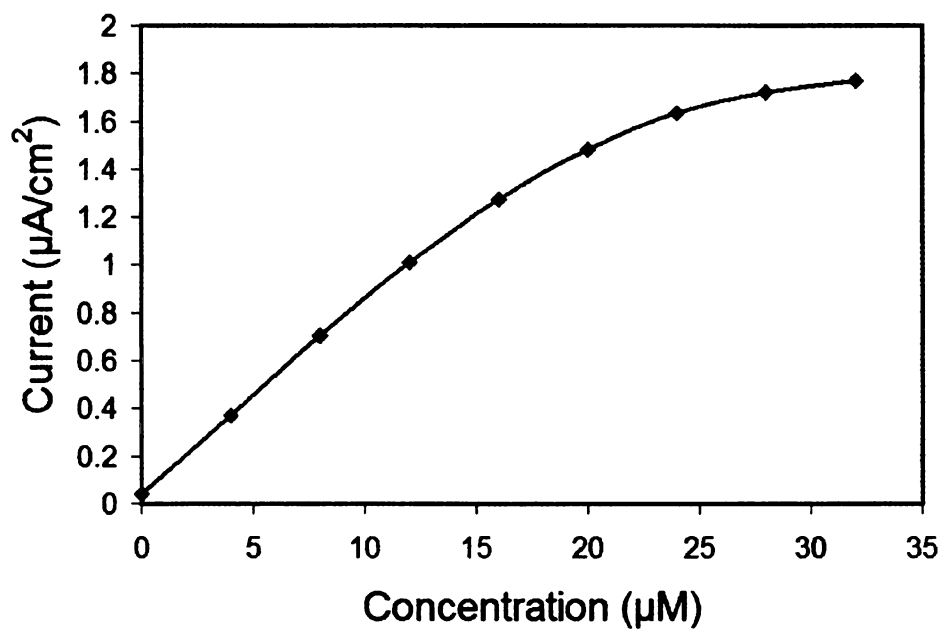
range. The highest signal-to background ratio, was obtained at -0.1 V. At working potential more negative than -0.1 V, higher signals were obtained, but the background current also increased distinctly. Therefore, a working potential of -0.1 V was used for further studies. The effect of pH was also studied in the pH range 5.5 to 8.0 in 0.1 M phosphate buffer at working potential of -0.1 V. As shown in Figure 5.3b, the response current attained a maximum value at pH 7.0. This pH was used for further studies.

5.3.3 Measurement of esterase activity using NEST biosensor

Figure 5.4a displays a typical current-time response under the optimal experimental conditions after the successive addition of aliquots of 4 μM phenyl valerate to the phosphate buffer. A well defined reduction current, proportional to the amount of phenyl valerate, was observed. The response time of the electrode was less than 20 s, due to the nano-scale thickness of the interface. The response to phenyl valerate was linear ($r=0.991$) in the range 0.5 μM to 12 μM , and it reached saturation at approx. 30 μM (Figure 5.4b). The limit of detection was 0.5 μM at a signal-to-noise ratio of 3. The reproducibility of the sensor was investigated at a phenyl valerate concentration of 4 μM ; the mean current was approximately 348 nAcm^{-2} , with a relative standard deviation of 9.9%. Figure 5.5 shows a control experiment which was done on an electrode containing only poly-L-lysine and tyrosinase bilayers. As expected, a relatively very small rise in steady state current was observed on the addition of phenyl valerate. The small rise can be attributed to the presence of small amount of phenol produced due to auto hydrolysis of phenyl valerate solution.



(a)



(b)

Figure 5.4: (a) Current time response of the NEST biosensor to the addition of aliquots of 4 μM phenyl valerate, in 0.1 M phosphate buffer, pH 7.0, at an applied potential of -0.1V (vs Ag/AgCl). (b) Calibration plot.

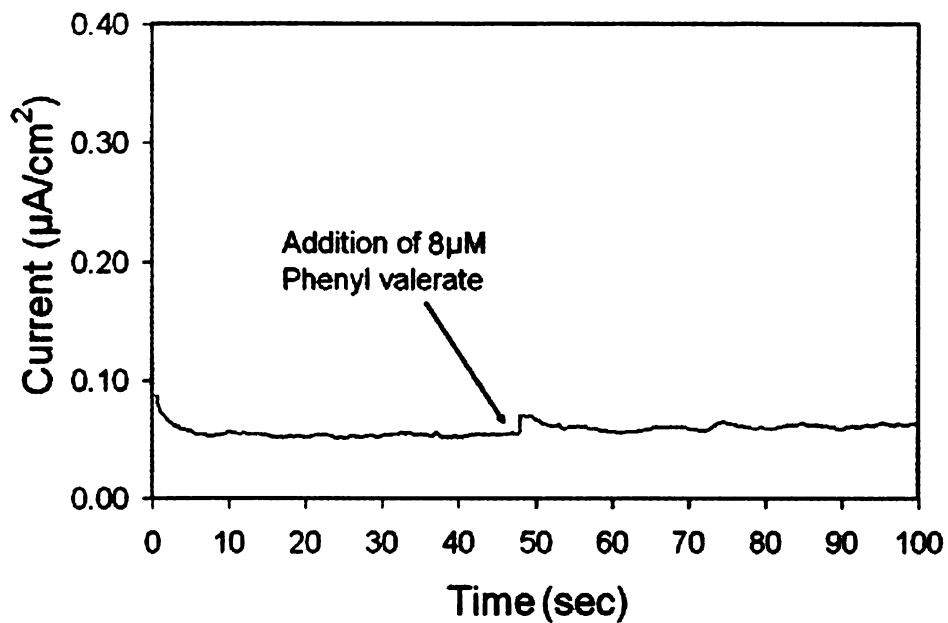


Figure 5.5: Control experiment: Current time response on an electrode containing only tyrosinase. The electrode was assembled in exactly the same way as NEST biosensor, except that the final NEST layer was not deposited.

5.3.4 Inhibition of esterase activity

To measure inhibition of the esterase activity, an aliquot of phenyl valerate was added to the phosphate buffer. After a steady biosensor signal was obtained, a known quantity of phenylmethylsulfonyl fluoride (PMSF), a non-neuropathic compound previously shown to inhibit NEST (or NTE) esterase activity, was added to the phosphate buffer solution, and the resulting drop in current was measured. At very low concentration there was not appreciable drop in signal as shown in Figure 5.6. As shown in Figures 5.7, a 20% ($\pm 3\%$) decrease in response on the addition of 100 μM PMSF and a 70% ($\pm 4\%$) decrease on the addition of 1000 μM PMSF was observed as shown in Figure 5.8. PMSF inhibition of NEST esterase activity reduces the amount of phenol and subsequently *o*-quinone produced. Therefore, less of *o*-quinone gets reduced at the electrode surface, leading to a drop in current. These results suggest that the NEST biosensor can be used for dose dependent detection of NEST inhibitors.

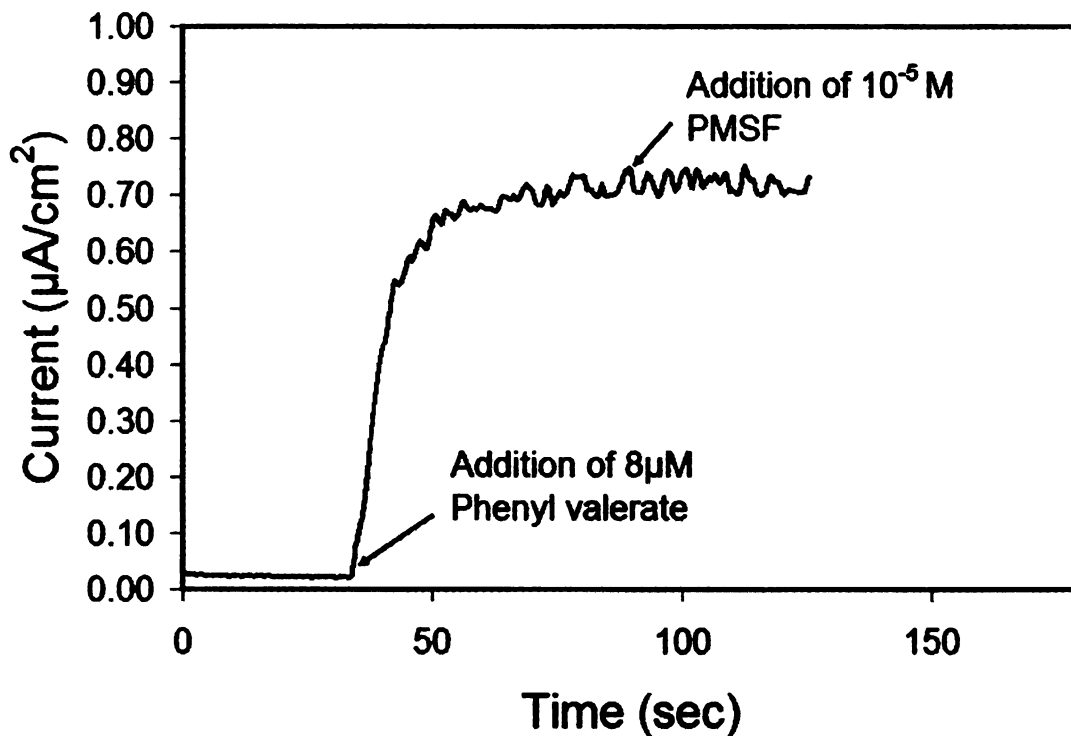


Figure 5.6: Current time response of NEST biosensor to the addition of phenyl valerate in phosphate buffer (0.1 M, pH 7.0) to obtain a final phenyl valerate concentration of 8 µM followed by the addition of NEST inhibitor PMSF to obtain a final PMSF concentration of 10 µM.

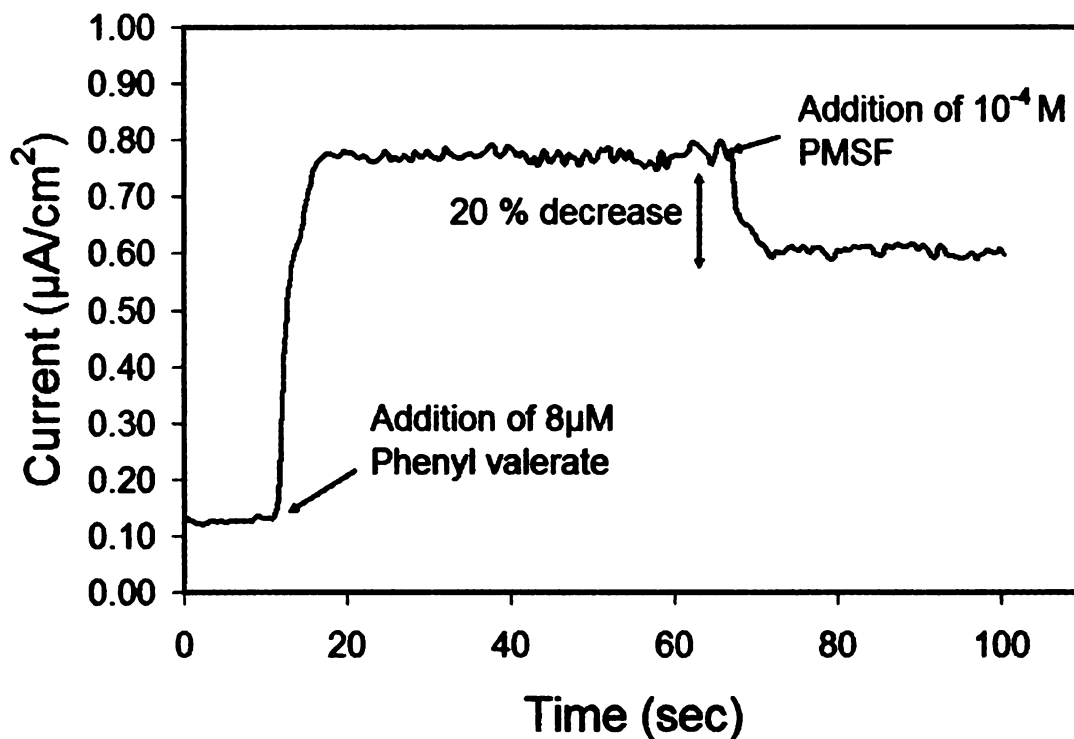


Figure 5.7: Current time response of NEST biosensor to the addition of phenyl valerate in phosphate buffer (0.1 M, pH 7.0) to obtain a final phenyl valerate concentration of 8 μM followed by the addition of NEST inhibitor PMSF to obtain a final PMSF concentration of 100 μM .

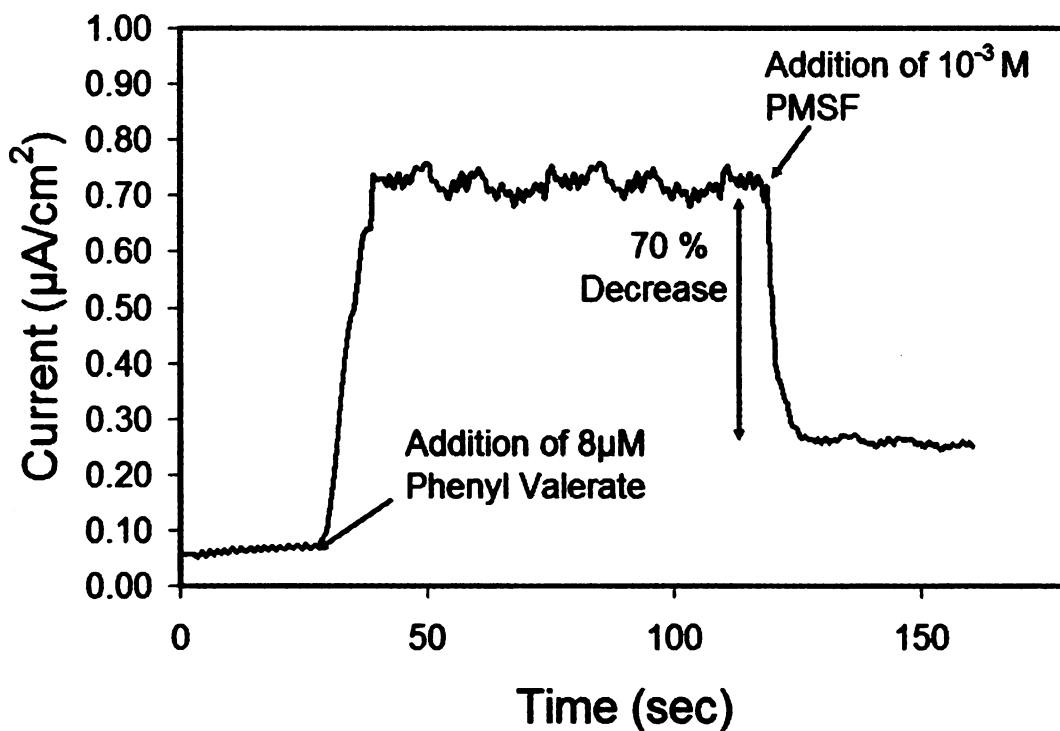


Figure 5.8: Current time response of NEST biosensor to the addition of phenyl valerate in phosphate buffer (0.1 M , pH 7.0) to obtain a final phenyl valerate concentration of 8 μM followed by the addition of NEST inhibitor PMSF to obtain a final PMSF concentration of 1000 μM .

5.3.5 Higher sensitivity NEST biosensor

NEST biosensor sensitivity could be increased by increasing the number of bilayers of PLL-Tyr to six. As discussed by Kohli *et. al* [103] in the mathematical model developed for the NEST biosensor, that the sensitivity can be improved more efficiently by increasing the amount of tyrosinase immobilized on the surface rather than increasing the amount of NEST. Hence, we developed a sensor by increasing the bilayers to six as the sensitivity of catechol sensor was maximized with 6 bilayers as discussed in previous chapter.

The same procedure was followed to fabricate biosensor. The gold electrode was first modified with thioctic acid followed by the deposition of PLL-Tyr bilayers. After addition of 6 bilayers a layer of NEST was added. The sensor was tested for NEST activity by phenyl valerate assay. The sensitivity went upto $847 \pm 158 \text{ nA cm}^{-2}\mu\text{M}^{-1}$ for the addition of phenyl valerate. The plot for phenyl valerate is shown in Figure 5.9. The NEST inhibition was also done by addition of 100 μM and 1mM of PMSF. The decrease in current was same as observed with 3 bilayers of NEST. The plots for inhibition of NEST on 6 bilayers of PLL-Tyr are shown in Figure 5.10 and 5.11 for 100 μM and 1 mM respectively. There was no remarkable decrease in current with 10 μM addition of PMSF (data not shown). Hence higher sensitivity NEST biosensor can be obtained by increasing the amount of Tyrosinase on the interface. It also implies that better sensors can be prepared with marginal increment to cost as tyrosinase is commercially available and can be easily deposited on to the electrode by using LBL deposition.

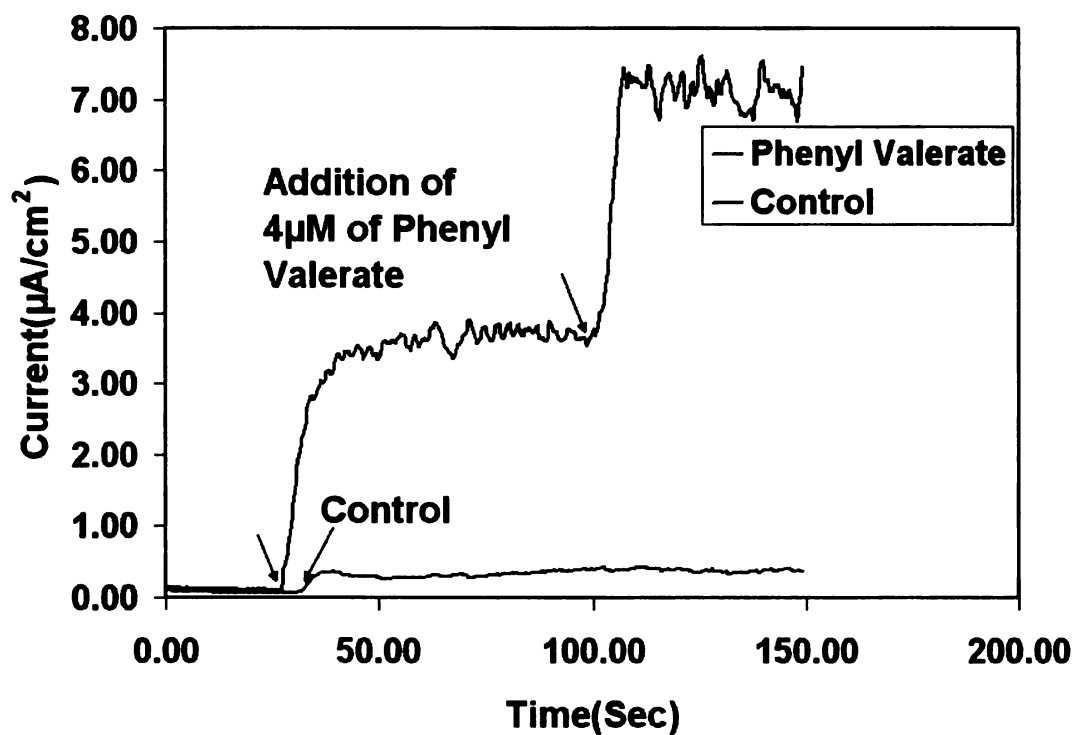


Figure 5.9: Current time response of NEST biosensor with 6 bilayers of PLL-Tyr underneath the NEST layer. The sensor was tested in phosphate buffer (0.1M) with electrode maintained -0.1V vs Ag/AgCl reference electrode. In control the electrode was prepared in exactly the same manner but NEST layer was not added.

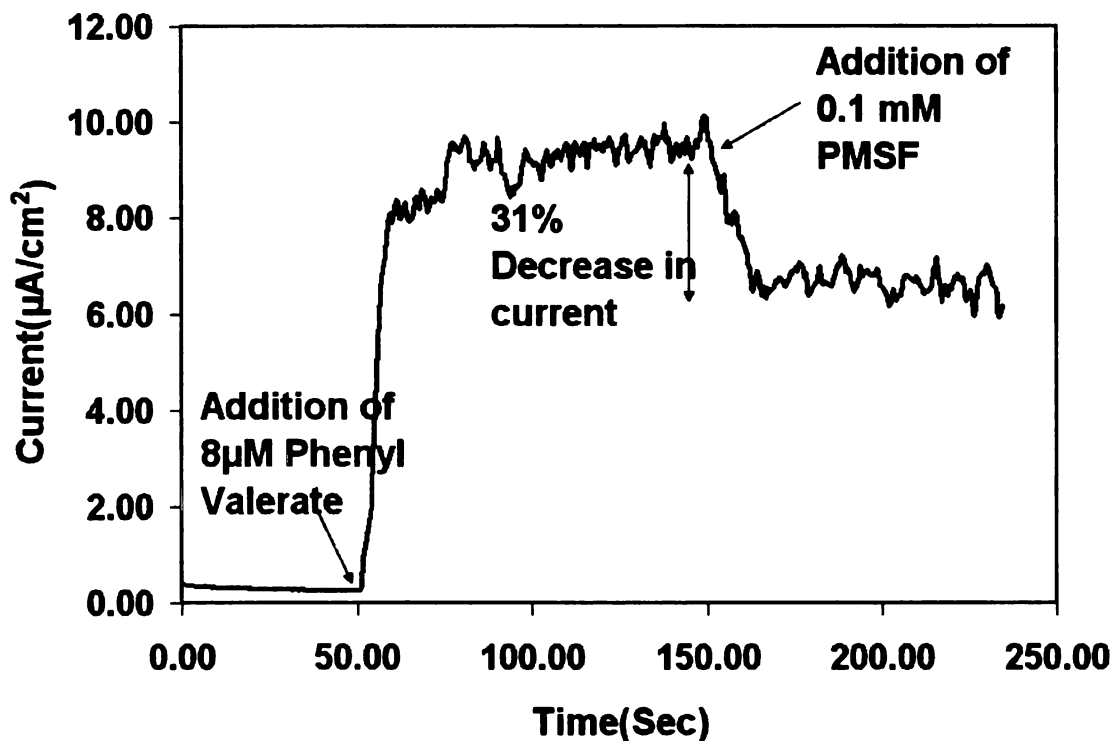


Figure 5.10: Current response of NEST biosensor with 6 layers of PLL-Tyr and followed by inhibition of NEST by addition of 0.1 mM PMSF. First phenyl valerate was added to get the final concentration of 8 μM in bulk solution. The current response was allowed to achieve steady state before addition of an aliquot of PMSF to get final concentration of 0.1 mM.

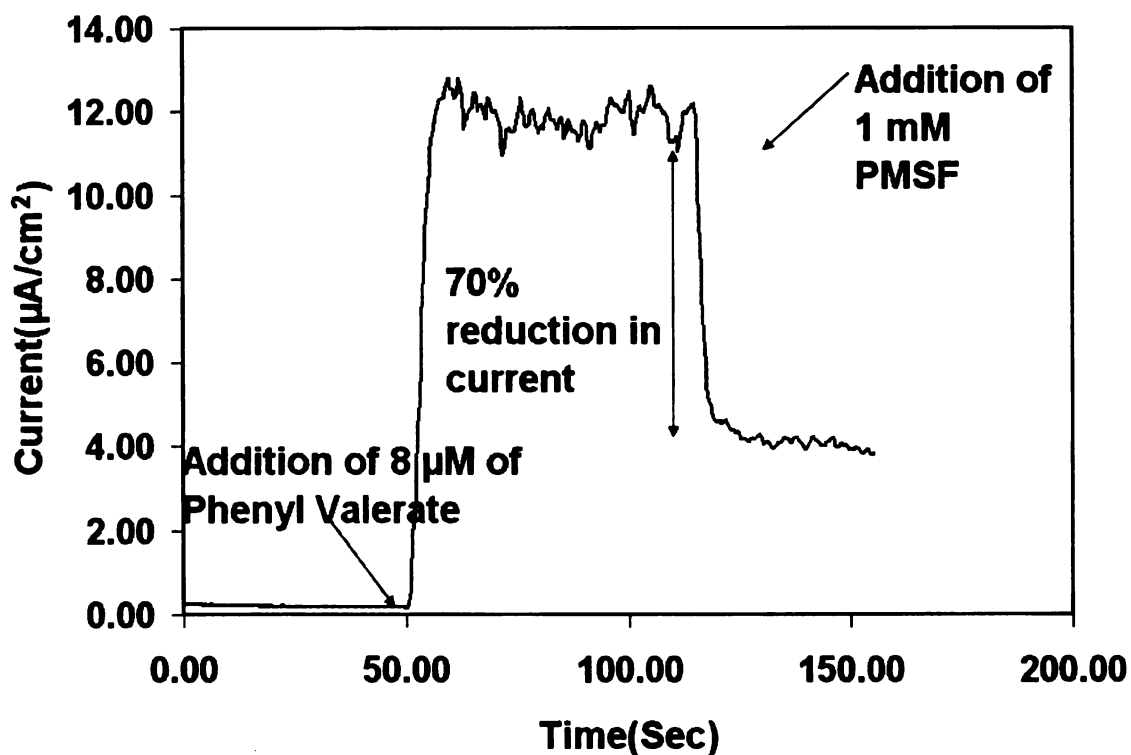


Figure 5.11: Current response of NEST biosensor with 6 layers of PLL-Tyr and followed by inhibition of NEST by addition of 1 mM PMSF. First phenyl valerate was added to get the final concentration of 8 μM in bulk solution. The current response was allowed to achieve steady state before addition of aliquot of PMSF to get final concentration of 1 mM.

5.3.6 Significance of NEST biosensor

This new biosensor approach to measuring NEST esterase activity and its inhibition can in principle easily be extended to full length NTE. The approach offers several advantages over the old two step method. First, it requires only a single step to measure NEST (or NTE) esterase activity. Because the NEST esterase activity is co-immobilized with tyrosinase on the sensor interface, the presence of phenyl valerate triggers sequential reactions that result in an electrical signal. Second, the nanometer-scale thickness of layers in the sensing interface provides a very short diffusion path giving a rapid response time (less than 10 seconds). Third, the biosensor is suitable for continuous, real-time measurements of esterase activity. Fourth, the biosensor is designed to achieve signal amplification via recycle of o-quinone to catechol, thus increasing the sensitivity of the sensor. Fifth, the biosensor interface is generated by flexible, layer-by-layer (LBL), molecular self-assembly methods that would allow it to be assembled on electrodes inside microfluidic channels, thus enabling the production of high-density biosensor arrays consisting of various esterases for high-throughput applications.

This combination of desirable properties makes this interface well suited for important applications, including studying the kinetic properties of esterases such as NEST protein, high-throughput screening of compounds for NEST (or NTE) inhibition and continuous, on-line, environmental monitoring to detect chemical warfare agents that target NEST (or NTE) and other esterases.

5.4 CONCLUSIONS AND FUTURE WORK

A biosensor has been developed that allows the activity of NEST to be measured continuously. The biosensor was fabricated by layer-by-layer assembly approach to co-immobilize NEST and tyrosinase on a gold electrode. Ellipsometry provided evidence for the sequential assembly of the multiple layers that make up the interface. Constant potential voltammetry allowed NEST enzyme activity to be measured with a rapid response time (< 10 s). The biosensor gave dose-dependent response to known non-neuropathic (PMSF) NEST inhibitors. As further studies, the NEST sensor can be fabricated on higher sensitivity sensors as discussed in previous chapter.

6 FABRICATION OF POLY-LACTIC ACID PARTICLES USING A HIGH SHEAR RATE MIXER

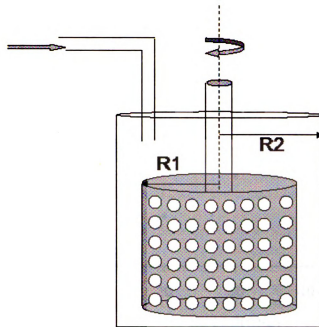
6.1 INTRODUCTION

Functionalized nanoparticles are used in a wide variety of biological application such as biosensors, biocatalysis, and drug delivery. Nanoparticles in drug delivery are gaining widespread interest due to their size, as the larger drug delivery vehicles can get opsonized in blood stream or taken up by the reticuloendothelial system [104, 105]. These nanoscale drug delivery vehicles can potentially circumvent this problem and can be more efficient for drug delivery. Nanoparticles can be loaded with drugs during formation of particles and/or the prefabricated particles can be functionalized using various surface treatment for anchoring site-specific molecules for target [106]. Fabrication of polymeric nanoparticles can be broadly classified in two schemes; one involves polymerization of monomers, whereas second involves starting from preformed polymers. Methods to form nanoparticles from preformed polymers include emulsion diffusion method [107, 108] and nanoprecipitation [3, 109].

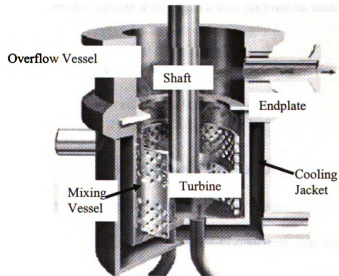
In emulsion diffusion, first polymer is dissolved in a solvent and the solution is added into a non-solvent, like water, containing some stabilizer (or surfactant) and then they are homogenized to form emulsion having tiny droplets of polymer solution dispersed in water. Then the solvent is allowed to diffuse into the non-solvent by adding excess amount of non-solvent phase and mixing for certain duration of time, thus leading to the formation of nanoparticles [110, 111]. In nanoprecipitation, solvent like acetone or ethanol is used to dissolve polymer and then the polymer solution is added to nonsolvent such as water. Nanoprecipitation differs from emulsion diffusion as there is no formal

emulsion formation. As polymer solution is added, acetone starts to diffuse out into nonsolvent with some polymer chain associated with it. As it diffuses further, the polymer chains aggregate to form nanoparticles [112].

This work involved fabrication of polymer nanoparticles using the thin-film spin system, “T.K. FILMICS® Model 80-50”, from PRIMIX Japan. A scheme of mixing chamber of the high shear rate mixer is shown in Figure 6.1. It consists of concentric cylinders (inner dia. 5.2 cm and outer dia. 5.8 cm) where inner cylinder can rotate at high speeds imparting high shear forces on the materials being mixed. This mixer can impart high shear force on the particles. Also mixing occurs in an open system as the mixer has an opening that is also used as injection port. The turbine can achieve high circumferential speed of 50m/s. Reynolds number equivalent to the circumferential speed with water as fluid is plotted in Figure 6.2. The non-linear trend can be explained by the heat generated inside the chamber which raises the temperature of the water. Higher temperature decreases the viscosity of water thereby changing the Reynolds number.



(a)



(b)

Figure 6.1: (a) Schematic of mixing chamber of the nanomixer. It has cylindrical turbine which rotates at peripheral speed of 10m/s to 50m/s. (b) A cross-sectional cartoon, it can have one or two injection port with continuous processing.

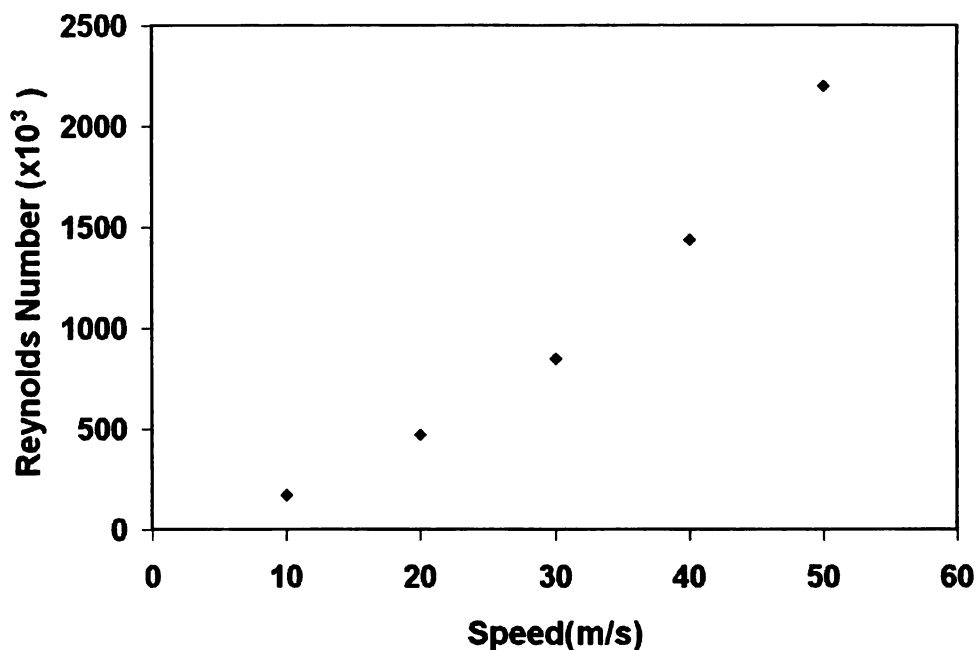


Figure 6.2: Turbine peripheral speed and equivalent Reynolds number for Couette-Taylor geometry flow.

6.2 THEORETICAL BACKGROUND

6.2.1 Nanoprecipitation

Nanoprecipitation is a process of spontaneous precipitation of polymer into a non-solvent phase giving rise to polymer nanoparticles. Polymer is dissolved in a solvent and the solution is added to a non solvent where solvent-nonsolvent are miscible and hence solvent diffuses into non-solvent and polymer chains associated with it precipitate out to form nanoparticles.

According to literature [110], the size of nanoparticles during nanoprecipitation is governed by solvent-nonsolvent solubility. A solubility parameter (δ) of solvent or nonsolvent is defined as

$$\delta = \sqrt{\frac{(\Delta H - RT)}{V_m}} \dots\dots\dots(6.1)$$

where ΔH is heat of vaporization (J mol^{-1}), R is gas constant ($\text{J K}^{-1} \text{mol}^{-1}$), T is temperature (K) and V_m is molar volume ($\text{m}^3 \text{mol}^{-1}$). Difference in solubility parameters ($\Delta\delta$ solvent-nonsolvent) of solvent and non-solvent is an important parameter. Lower the $\Delta\delta$, the smaller will be the nanoparticles.

At slow speeds smaller particles were prepared as the process is probably governed by nanoprecipitation mechanism. But at high shear rates we get particle size increase to microns scale. This could be because, as the smaller particles form during initial stages, they agglomerate or coalesce because of high shear rate. As the temperature in the mixer is beyond the glass transition temperature T_g , the sticky polymer particles can gel together to form larger particles.

6.2.2 Emulsion Diffusion

In this work we investigate the influence of mixing rates on the formation of polymeric particles and their possible agglomeration during mixing process. Some of the parameters that can influence particle size are viscosity, density of solvent and non-solvent, concentration of polymer in solvent phase and shear rate. Shear rate can cause dispersion of particles or enhance emulsion process but it can also cause agglomeration or coalescence of particles and emulsion droplets.

Role of shear rate can be more easily studied by using emulsion diffusion process for nanoparticles formation. As illustrated in Figure 6.3 in emulsion diffusion process,

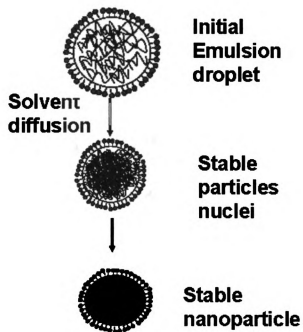
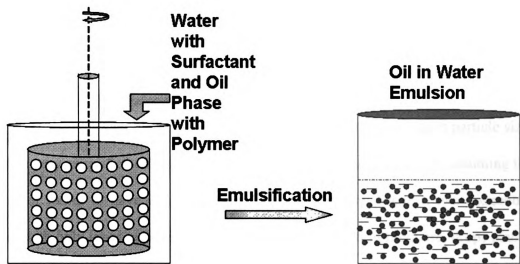


Figure 6.3: Emulsification is carried out in the nanomixer by adding water with surfactant and polymer in oil (solvent). This was followed by diffusion step in which emulsion was added to excess amount of water for solvent phase to diffuse out.

emulsion can be formed in the mixer and then the particles can be formed in second stage by diffusing out the solvent by addition of excess amount of non-solvent [107]. Hence we can possibly determine whether formed droplets agglomerate or coalesce due to high shear rate.

To analyze this problem and determine parameter that should affect particle size, we made a very simplified estimate for the turbulent flow at high speeds by assuming the geometry of mixer to have Couette-Taylor flow, that is flow between two concentric cylinders with only inner cylinder rotating [113]. As discussed in literature, drops placed in turbulent conditions could break upon the action of viscous or inertial stress [114, 115]. Either of the stress could be dominant depending on the size of the smallest turbulent eddies in the flow [116-118].

So called “Kolmogorov Scale” is used to approximate the size of smallest eddies [115], λ , given by equation 6.2

$$\lambda \approx \epsilon^{-1/4} \eta_c^{3/4} \rho_c^{-3/4} \dots\dots\dots(6.2)$$

where η_c is viscosity (Pa s^{-1}) and ρ_c is density of the fluid (kg m^{-3}) or continuous phase and ϵ is the rate of energy dissipation (m^2s^{-3}). Hence faster the rate of agitation, which correlates to rate of energy dissipation, smaller should be the size of the turbulent eddies.

Estimation of the diameter of droplets can be done, with emulsification in inertial turbulent regime, for drops with viscosity similar to that of water. Kolmogorov-Hinze theory gave an estimate of maximum stable drop [117], d_{KH} in inertial turbulent regime as given by equation 6.3.

$$d_{KH} = A_1 \varepsilon^{-2/5} \sigma^{3/5} \rho_c^{-3/5} \dots\dots\dots(6.3)$$

where A_1 is a constant of proportionality of the order of unity and σ is interfacial tension ($N m^{-1}$).

In case of viscous turbulent regime, the drop breakup occurs under the action of viscous stress inside the turbulent eddies. The maximum stable drop diameter [117] d_{KV} , was estimated as given by equation 6.4

$$d_{KV} = A_2 \varepsilon^{-1/2} \eta_c^{-1/2} \rho_c^{-1/2} \sigma \dots\dots\dots(6.4)$$

where $A_2 \sim 4$, is a numerical constant

Hence, these equations give an estimate about how the diameter of emulsion droplets should vary by varying different parameters like viscosity, density and interfacial tension. Though this theory does not account for viscosity of the dispersed phase but these equations are valid for dispersed phase viscosity less than the continuous phase's viscosity. There are modification of aforementioned equations to account for higher viscosity dispersed phase [117]. Hence, for the known value of energy dissipation, all the three values λ , d_{KV} , d_{KH} can be estimated. If equations predict, $\lambda < d_{KH}$ then the emulsification is in inertial turbulent regime. Whereas if $d_{KV} < \lambda$ then the emulsification occurs in the viscous regime. If all three values are approximately equal then emulsification occurs in transitional regime. If above conditions are not met, modified equations which accounts for viscosity of dispersed phase could be used.

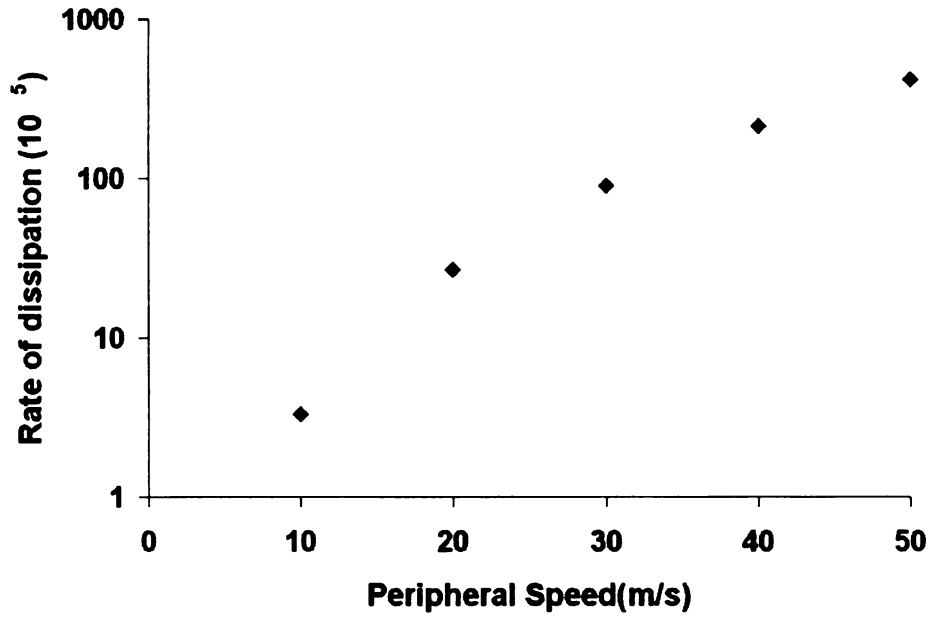
Experimentally the regime can be determined by changing the η_c , as changing η_c strongly affects λ and d_{KV} , but not d_{KH} . Hence if diameter changes by changing viscosity it is in viscous regime.

Rate of dissipation of energy per unit mass characterizes the hydrodynamic condition during emulsification. For very high Reynolds number and Couette-Taylor kind of flow, the rate of energy dissipation can be calculated by a simple approximation [119] as given by equation 6.5

$$\epsilon = (\Delta U)^3 / \Delta r \dots \dots \dots (6.5)$$

where ΔU is velocity difference across distance Δr . Δr is difference between inner and outer radii of cylinders. Approximate rate of energy dissipation as a function of peripheral speed is given by Figure 6.4a.

Substitution of values in above equations by assuming ethyl acetate as solvent and water as continuous phase we could estimate all the parameters. We got the drops to form in turbulent inertial regime as $\lambda < d_{KH}$ for all mixing speeds. Figure 6.4b gives the plot of λ and d_{KH} for each mixing speed. This simplified approximation of mixing in turbulent range, gives us the trend that the droplet sizes should follow by changing the mixing conditions. Smaller emulsion droplet sizes can be achieved by transiting to viscous turbulent regime by increasing viscosity of continuous phase or by bringing down the interfacial tension can be inferred from equation 6.4. Hence it provides us the parameters that can be varied to influence the mixing conditions and possibly the particle size.



(a)

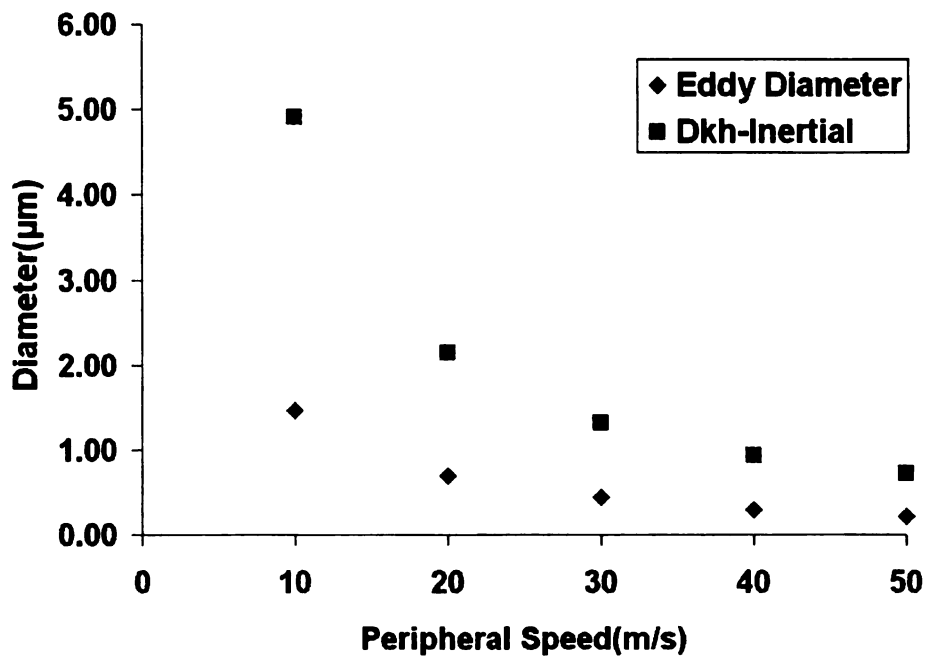


Figure 6.4: (a) Rate of energy dissipation as a function of peripheral speed and (b) Plot of eddy diameter, λ and droplet diameter for inertial turbulent regime d_{KH} , for each mixing speed assuming ethyl acetate and water system.

6.3 EXPERIMENTAL SECTION

6.3.1 Materials

Poly(DL)lactic Acid from LakeShore Biomaterials(California, USA), Poly(L)Lactic Acid from Sigma Aldrich, KCl (analytical Grade) and Acetone from Fluka. Pluronic F68, Cetyl Trimethyl Ammonium Bromide (CTAB), gold chloride trihydrate, hydroxylamine and sodium citrate dehydrate were purchased from Sigma and de-ionized (DI) water was used at 18.2 M Ω purity.

6.3.2 Experimental Details

For nanoprecipitation 15mg/ml of PLA was dissolved in acetone. 15mg/ml of Pluronic F68 and 10mM CTAB was dissolved in water. 60 ml of this surfactant solution was added in mixing chamber of FLIMICS from Primix Japan. Mixer was closed and set to run for certain time duration at different peripheral speeds varying from 10 m/s to 50m/s. Water in cooling jacket was maintained at 4^oC. Polymer solution was injected after mixer achieved its maximum speed.

For emulsion diffusion, ethyl acetate and water were mutually saturated to avoid any inter-diffusion during emulsion formation. 15mg/ml PLA solution was prepared using saturated ethyl acetate. 15 mg/ml solution of Pluronic F68 was prepared in saturated water. Emulsion was prepared by adding 20 ml PLA solution in 60 ml of F68 solution. It was emulsified at different speeds for specific preset time duration. The emulsion was collected and added to 300 ml of pure DI water, stirred at 600 rpm in a beaker for diffusion step to take place. Once the particles have formed the particle suspension was kept in partial vacuum for 2 hour to allow ethyl acetate to evaporate.

Gold nanoparticles (AuNPs) of mean diameter 18 nm were prepared using a standard procedure [120]. AuNPs suspension was mixed in nanomixer to study the effect on agglomeration of nanoparticles. AuNPs were mixed at different speeds inside the mixer and agglomeration was measured using UV-vis absorbance at 540 nm [121].

6.3.3 Dynamic Light Scattering (DLS)

DLS was used to estimate the mean size of the particles. DLS was done in 10mM KCL solution using DLS Analyzer (90Plus) from BrookHaven instruments. Average of mean diameter was obtained by 3 runs for each sample. The uniform sphere option was selected for measuring the particle size.

6.3.4 Microscopy

Electron microscopes were located at the Centre of Advanced Microscopy at MSU. Scanning Electron Microscope (SEM) was used to estimate mean size as well as coefficient of variation for particle size. SEM used for high resolution imaging was JEOL 6300F with field emission. PLA particles were coated with gold film to view under electron microscope. Transmission electron microscopy (TEM) was done on PLA nanoparticles using JEOL 2200FS 200 kV field emission TEM. Copper grids coated with carbon were used to support PLA nanoparticles. Optical Microscope was used to image fluorescent polystyrene particles which were subjected to high shear in the nanomixer along with PLA emulsion. A Nikon Eclipse E400 microscope was used to capture fluorescent images.

6.3.5 UV-vis absorbance spectroscopy

UV-vis absorbance spectroscopy was used to determine the AuNPs agglomeration. The spectrophotometer used was SP-890 UV-Vis Turner

Spectrophotometer. AuNPs solution mixed for 10 minutes at different peripheral speeds was collected and its absorbance was measured at 540 nm.

6.3.6 Zeta Potential

Zeta potential was measured using 90Plus Brookhaven Instrument. PLA particles were added to KCl solution of different ionic strengths. Zeta potential measured is an average of 3 runs for each sample.

6.3.7 Differential Scanning Calorimetry

Differential scanning calorimetry was done using TA Instruments Q100. Small quantity of polymer was weighed and placed inside the chamber with continuous flow of nitrogen. The temperature range was chosen from 25°C to 200°C with heating rate of 5°C/minute.

6.3.8 Thermogravimetric Analysis

Thermogravimetric analysis was done using 2950 TGA HR V5.4A from TA instruments. Small quantity was weighed and placed inside the chamber with the nitrogen flow rate of 60ml/minute. The samples were heated from 25°C to 200°C at the heating rate of 5°C/minute.

6.4 RESULTS AND DISCUSSION

6.4.1 Nanoprecipitation

Nanomixer had negligible influence on the particle size during the precipitation process at low mixing speeds of 10 m/s and 20m/s as shown in Figure 6.8. The particle size was similar to precipitation done in a beaker with moderate stirring. It complies with

the theoretical background where the particle size during precipitation is governed more by thermodynamic factors like solvent parameters which determine the miscibility between two solvents. Hence theoretically mixing rate should not have influence on particle size.

The application of high shear rate led to the formation of particles of larger mean diameter as shown in Figure 6.8. This observation was counter intuitive to what was expected as shear rate should bring down the particle size. In nanomixer with small mixing volume, high shear rate can lead to the increase in the temperature of solution. With the water/acetone mixture, the temperature inside the nanomixer can reach the temperature of $65 \pm 2^{\circ}\text{C}$ at the mixing speed of 50m/s. This is beyond the glass transition temperature of PLA which is around 55°C . Hence these particles are heated beyond their glass transition temperature and the nanomixer causes these sticky particles to collide. As these particles are beyond their T_g , they coalesce to form larger particles as shown in Figure 6.5.

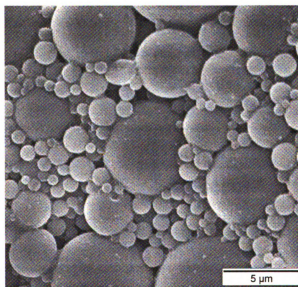


Figure 6.5: SEM image of PLA particles prepared at 50m/s mixing speed.

In the figure we observed very large particles with more than few microns in diameter whereas at 10m/s the mean diameter was around $151 \text{ nm} \pm 6 \text{ nm}$. We also observed the particles which were coalescing during the process of mixing at high speeds within the mixer as shown in Figure 6.6. As can be seen in the image the larger particles which are encircled appear to be coalescing and forming larger particles.

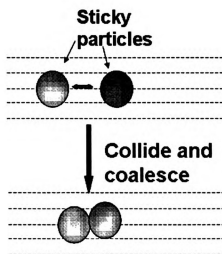
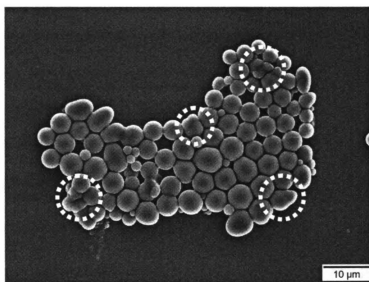


Figure 6.6: As can be seen in the SEM image the larger particles are heated above glass transition temperature and colliding and coalescing into larger particles.

The zeta potential for the particles formed by using Pluronic F68 as surfactant was measured in the presence of varying molar concentration of KCl. The zeta potential is a function of the ionic strength of the surrounding medium. According to Guoy-Chapman theory [122, 123] , as the charge on a surface of particle is counter balanced by the ions in the surrounding medium, it forms a compact static layer of oppositely charged ions called Stern Layer and then by loosely bound ions called diffuse layer. The zeta potential is considered as the potential at the end of stern layer. When the ionic strength is varied the zeta potential varies and is given by the following equation 6.6.

$$\tanh\left(\frac{e\zeta}{4kT}\right) = \tanh\left(\frac{e\Psi_o}{4kT}\right) \exp(-\kappa\Delta) \dots\dots\dots(6.6)$$

Where

e is the electronic charge (Coulombs); k: Boltzmann Constant (J K⁻¹);

T: Temperature (K); Ψ_o : Surface Potential (millivolts); κ : Reciprocal thickness of diffuse layer (m⁻¹); ζ : Zeta Potential (millivolts); Δ : Distance to the plane of zeta-potential from the surface (m).

Log of zeta potential function in equation 6.6 was plotted against the inverse of Debye length (data not shown). The intercept of that curve can be used to estimate surface potential on the surface of particle. Estimated surface potential was used to determine the surface charge density (σ_o) by using the following equation 6.7

$$\sigma_o = [(8kTn\epsilon_o\epsilon_r)^{\frac{1}{2}} \sinh\left(\frac{ze\Psi_o}{2kT}\right) \dots\dots\dots(6.7)$$

where ϵ_o and ϵ_r are permittivities (Farads/m); n number concentration of each ion in solution (m⁻³).

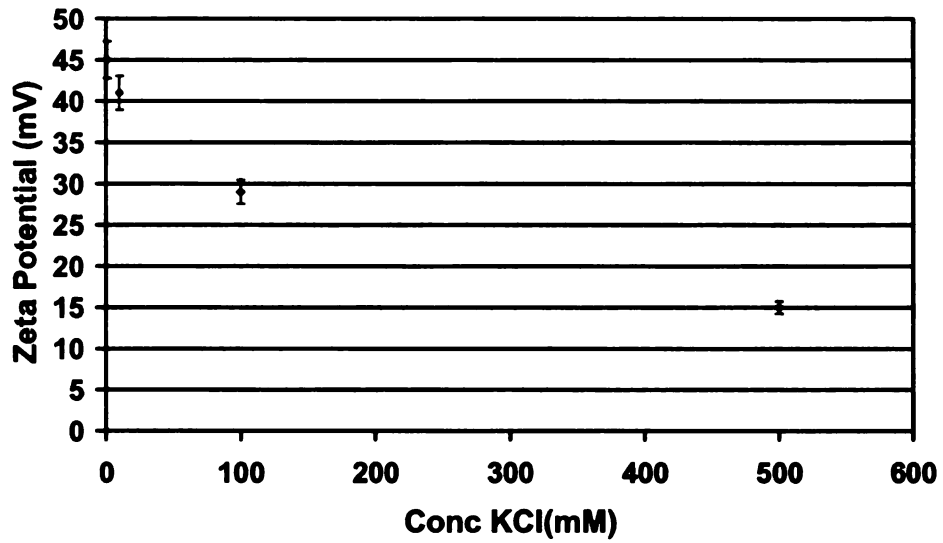
PLA particles were also fabricated by precipitation in presence of 10 mM CTAB. It is positively charged surfactant with amine groups providing the PLA particles a positive charge. The particles were formed by adding 15 mg/ml solution of PLA in acetone to 10mM solution of CTAB in DI water. PLA solution in acetone was injected in the nanomixer running at a set speed and solution was allowed to mix for 10 minutes.

Zeta potential for the particles fabricated using both the surfactants is plotted in Figure 6.7. As the ionic strength in the surrounding medium increases, the zeta potential decreases because there is more efficient screening of surface charge on the particles. The particles prepared with Pluronic F68 as surfactant had lower zeta potential in magnitude than the particle with CTAB as surfactant. CTAB has quaternary amine groups as polar head group which imparts strong charge to the particles. Log of zeta potential was also plotted as a function of ionic strength of solution for both the particles and intercept was used to determine surface potential and hence surface charge density. The surface charge density and surface potential calculated are tabulated in the Table 6.1.

Table 6.1 Effect of surfactant type on the surface charge and surface potential on nanoparticles formed

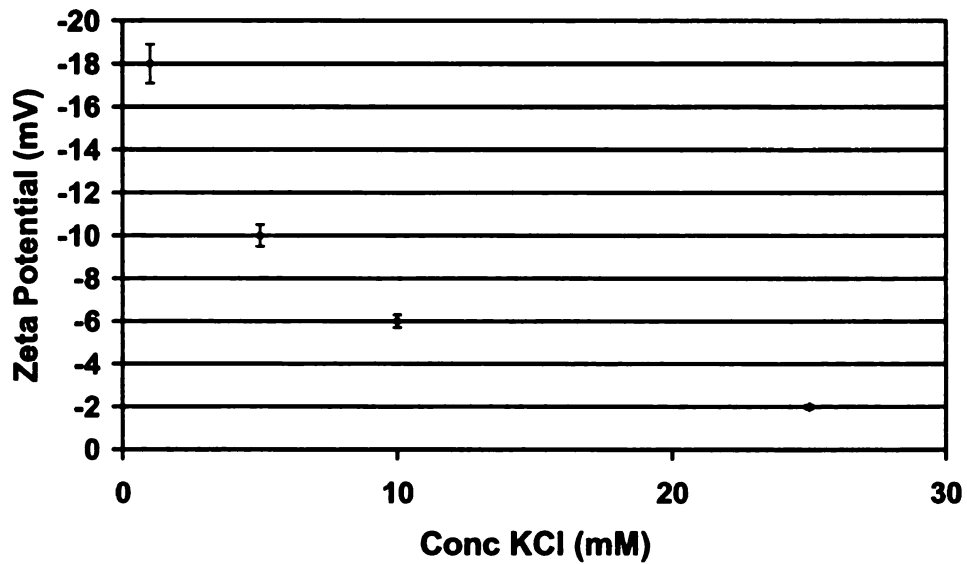
Surfactant	Surface Potential (mV)	Surface Charge ($\mu\text{ C/cm}^2$)
Pluronic F68	-34	-0.45
CTAB	48	1.57

CTAB as surfactant



(a)

Pluronic F68



(b)

Figure 6.7: Zeta potential of PLA particles (a) CTAB as surfactant; (b) Pluronic F68 as surfactant; as a function of varying ionic strength in DI water. Increasing the ionic strength decreases the zeta potential of the particles.

From the zeta potential measurement, an estimate of surface charge on particles can be made. The particle size for each surfactant is also plotted as function of mixing speed as shown in Figure 6.8. The particle size in both the cases went up as the mixing speed was increased. The temperature inside the vessel is also shown in the Figure 6.8. As the particles are mixed at higher speeds, the temperature inside the vessel rises beyond the glass transition temperature of PLA. Above T_g the softened particles impinge and coalesce to form larger particles. This agglomeration was also observed by mixing gold nanoparticles in the nanomixer. Gold nanoparticles were prepared by standard gold salt reduction using sodium citrate as catalyst and also stabilizer in solution under boiling conditions [120].

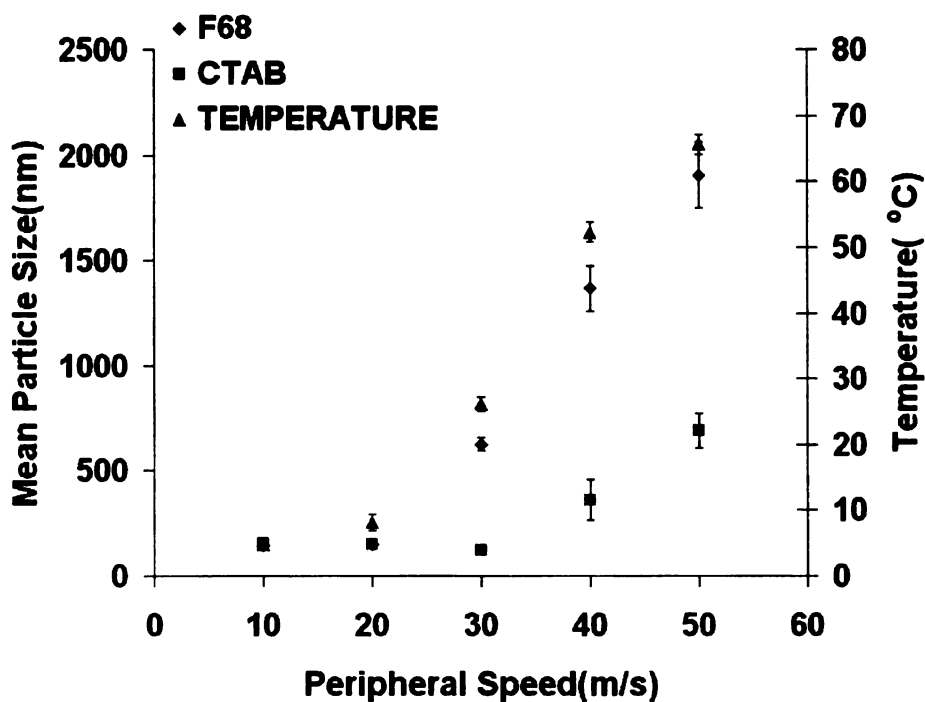


Figure 6.8: Mean particle size of PLA particles with Pluronic F68 and CTAB as surfactant. It also shows the temperature in the vessel at each mixing speed.

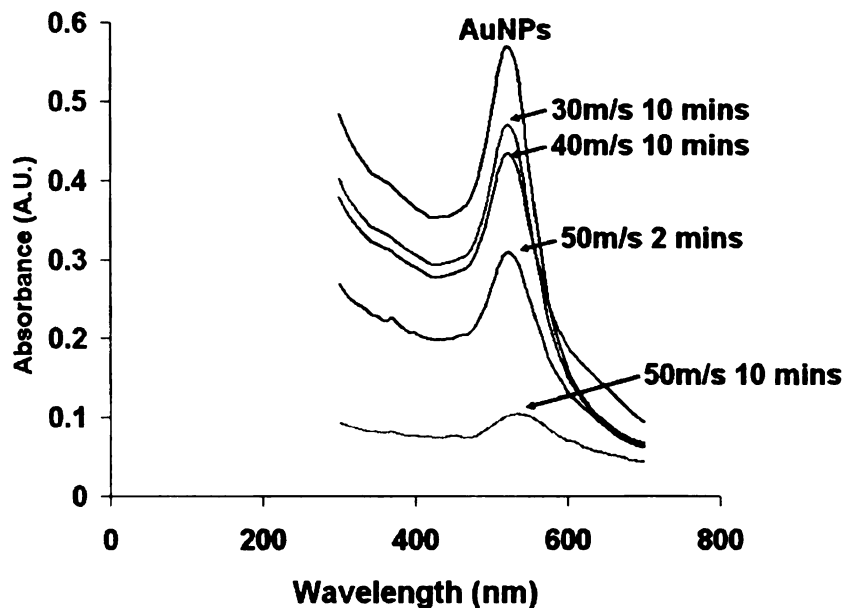


Figure 6.9: Decrease in the peak intensity at 540 nm after mixing gold nanoparticles inside the nanomixer.

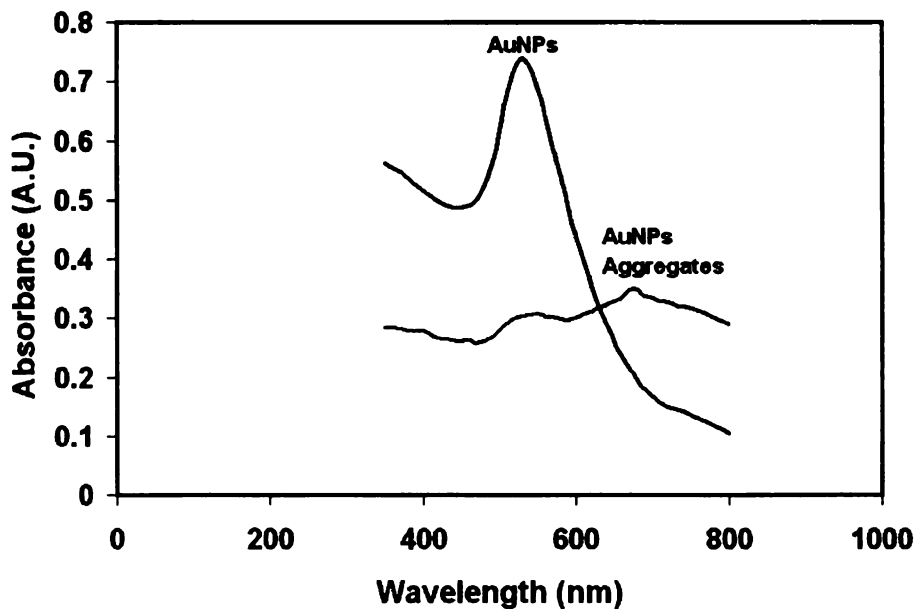


Figure 6.10: It shows the signature shift in the peak intensity from 540nm to 700 nm after agglomeration of gold nanoparticles.

The gold particles obtained before agglomeration had a mean diameter of 18 ± 2 nm. Free dispersed gold nanoparticles showed their characteristic absorption peak at 540 nm in UV-vis absorbance spectroscopy [56] as shown in Figure 6.9. As the particles were mixed, AuNPs agglomerated and collapsed out of the solution and the peak intensity went down with the mixing speed. There was no shift in the peak or a separate peak after AuNPs were mixed showing that there were no stable gold agglomerated in the solution and all the agglomerates precipitated out from the solution. The Figure 6.10 shows a typical shift in absorption peak to around 700 nm caused by agglomerated gold nanoparticles that are still suspended in solution. However when the AuNPs are subjected to high shear in the nanomixer they collide and form larger aggregates that eventually precipitate out of the solution.

Hence this gives us additional evidence that nanoparticles under high shear rate in nanomixer are subjected to two opposing phenomena. One is high shear force that would want to shear them apart. Whereas the same shear force also causes the dispersed particles to collide into each other and can lead to agglomeration and coalescence. In case of PLA particles, it formed larger particles as was observed directly when the speed was increased.

6.4.2 Emulsion Diffusion

Emulsion was prepared by first saturating ethyl acetate with water and vice versa. Polylactic acid was dissolved in saturated ethyl acetate and Pluronic F68 was dissolved in water saturated with ethyl acetate. The saturation of solvents is done to avoid any precipitation of polymer during emulsification. The emulsion was added to excess DI water for ethyl acetate to diffuse out. Ethyl acetate has solubility of around 10% in DI

water. So, 300 ml of DI water was taken for diffusion step as emulsion is added to pure DI water. During this step most of the ethyl acetate can diffuse out of the particles into the water phase. The particles were characterized by dynamic light scattering and scanning electron microscopy.

As the temperature rises up close to glass transition temperature at 40m/s mixing speed and further beyond the glass transition temperature at the mixing speed of 50m/s. The mixing times were varied for different speeds. For initial results the mixing time was 10 minutes for 10m/s to 30 m/s and 2 minutes for 40m/s and 1 minute for 50m/s. The mean particle diameter after diffusion step and the size of emulsion droplets was measured by dynamic light scattering and is plotted as a function of speed in Figure 6.11. As expected the particle size went down by increasing the mixing speed. High shear rate resulted in smaller droplet size in emulsion as shown in Figure 6.11. It can also be followed from the equations as discussed in section 6.2 where high shear rate leads to higher rate of energy dissipation. The droplet size that is stable under that turbulent condition gets smaller. Hence increasing mixing rate leads to decrease in droplet size that eventually leads to smaller particle size.

The emulsion droplet size, hence the particle size went down with the speed. Figure 6.12 shows a simple digital photograph with particles from 10m/s mixing speed up to 50m/s mixing speed. The suspension turned clearer from whitish appearance due to the decrease in the size of particles. Larger particles appear milky as they interfere with light passing through the solution whereas small particles size <100 nm appears clear because their size is much smaller than the wavelength of visible light. It gives us qualitative indication of particle size gets smaller with increasing mixing speed.

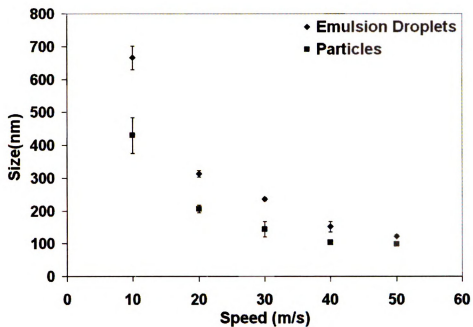


Figure 6.11: Mean particle size as obtained by dynamic light scattering for particles prepared at different mixing speeds in Nanomixer.

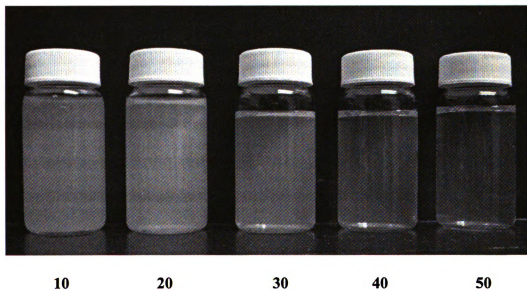
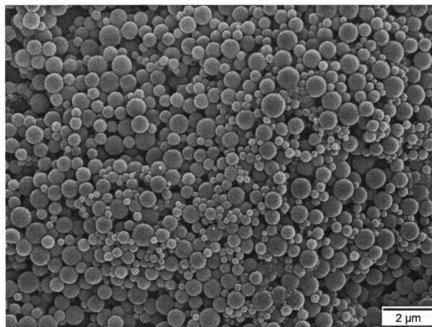
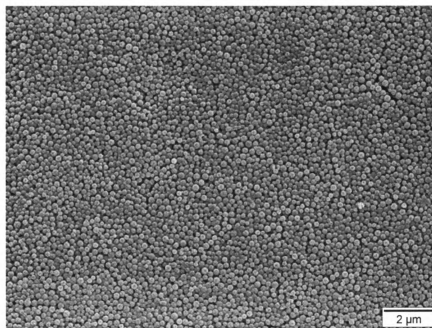


Figure 6.12: Emulsions were made at different speeds and then added to excess amount of water for particle formation.

Scanning electron micrographs of particles were obtained by drying particle suspension on a glass slide and coating it with a 7 nm layer of gold. Gold coating was required as PLA is not conducting. The scanning electron micrographs were obtained at working distance of 8 mm and accelerating voltage of 3 KV as higher accelerating voltage led to the damage of particles as discussed later in the chapter. Figure 6.13 show scanning electron micrograph of the particles obtained when emulsification was carried out at 10m/s (ED10) and 20m/s (ED20) mixing speed with the mixing time of 10 minutes. It is clearly seen that the particle size decreased as the mixing speed was increased. Higher magnification images in Figure 6.14 show particles are not that uniform at both the mixing speeds of 10m/s and 20 m/s. The coefficients of variation are 18% and 11% at the speeds of 10 m/s and 20m/s respectively.

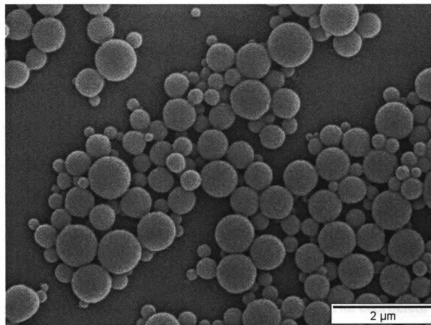


(a)

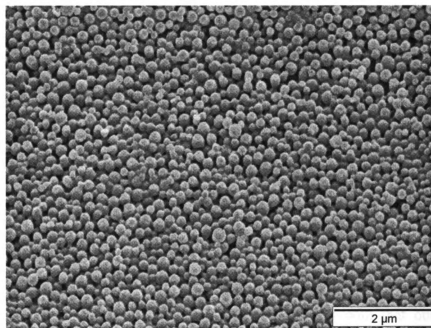


(b)

Figure 6.13: Scanning electron micrographs at 7500X of PLA nanoparticles obtained by emulsifying a) 10 m/s and b) 20m/s for 10 minutes.



(a)

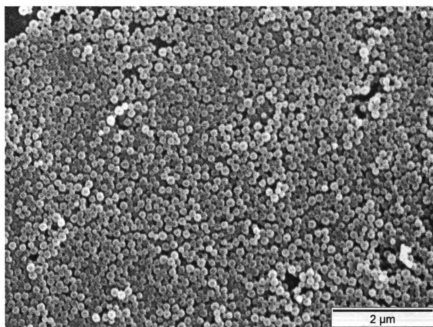


(b)

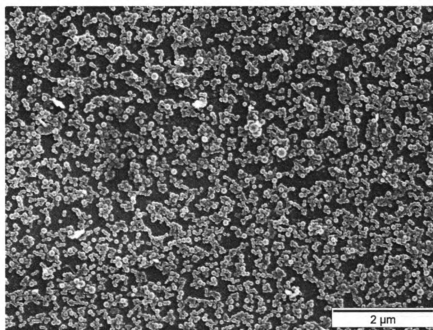
Figure 6.14: Higher magnification (15000X) scanning electron micrographs of PLA nanoparticles obtained by emulsifying a) 10 m/s and b) 20m/s for 10 minutes. Illustrates PLA particles at 10m/s are more polydisperse than particles at 20m/s.

In another set of experiments when the mixing speed was increased to 30m/s (ED30), the particle size reduced further. At 40m/s (ED40) and 50 m/s (ED50) mixing speed the time of mixing had to be reduced to 2 minutes and 1 minute respectively as the particle size grew larger at longer mixing time due to coalescence of PLA particles. The temperature in vessel also reached around or beyond the glass transition temperature of PLA causing particles to coalesce. Scanning electron micrographs shown for particles in Figure 6.15 are at same magnification as Figure 6.14 to illustrate particle size is much smaller than at slower emulsification speed. The following Figure 6.16 illustrates the particles at ED30 and ED40 at higher magnification. The particles appear polydisperse at higher magnification images especially in the case of ED30. The coefficient of variation for ED30 was 15% and ED40 was 10%.

At 50m/s (ED50) the particle size was slightly smaller than ED40 but with slightly higher coefficient of variation of 11%. This trend of small decrease in particle size from 40 to 50 m/s was similar to what we observed in theoretical treatment of droplet in turbulence. At higher turbulence conditions, the rate of decrease of particle size gets smaller. Therefore, we observe a faster reduction in particle size at slower speeds as in the case of ED10 to ED20 as compared to ED40 to ED50. The TEM and SEM images of particles obtained at 50m/s are shown in Figure 6.17. The mean diameter for each method was also approximated by actual measurement of particle diameters from the images. The mean diameter from SEM images was in good agreement with that obtained from dynamic light scattering experiment as shown in Figure 6.18.

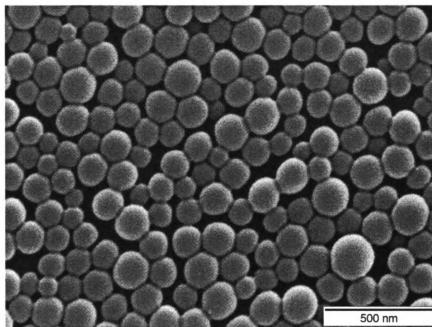


(a)

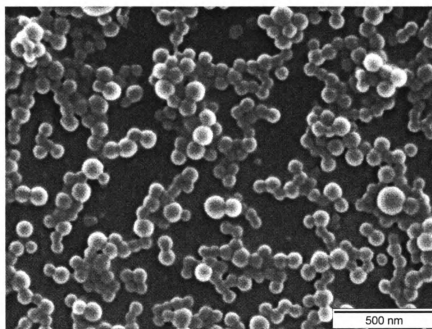


(b)

Figure 6.15: Scanning electron micrographs (15000X) of PLA nanoparticles obtained by emulsifying at a) 30 m/s for 10 minutes and b) 40m/s for 2 minutes.

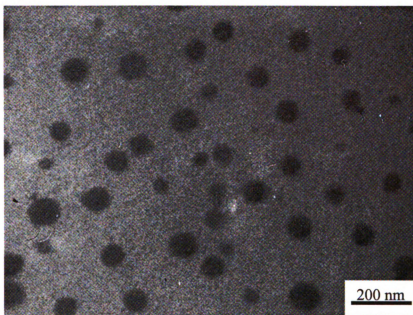


(a)

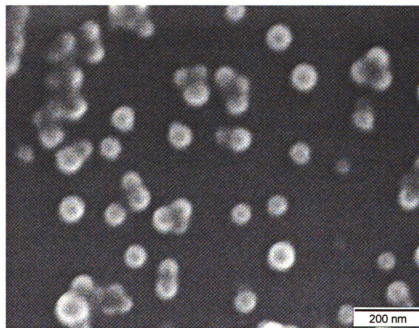


(b)

Figure 6.16: Scanning electron micrographs (65000X) of PLA nanoparticles obtained by emulsifying a) 30 m/s for 10 minutes and b) 40m/s for 2 minutes.



(a)



(b)

Figure 6.17: TEM (a) and SEM image (b) of PLA nanoparticles obtained by emulsifying at 50m/s for 1 minute.

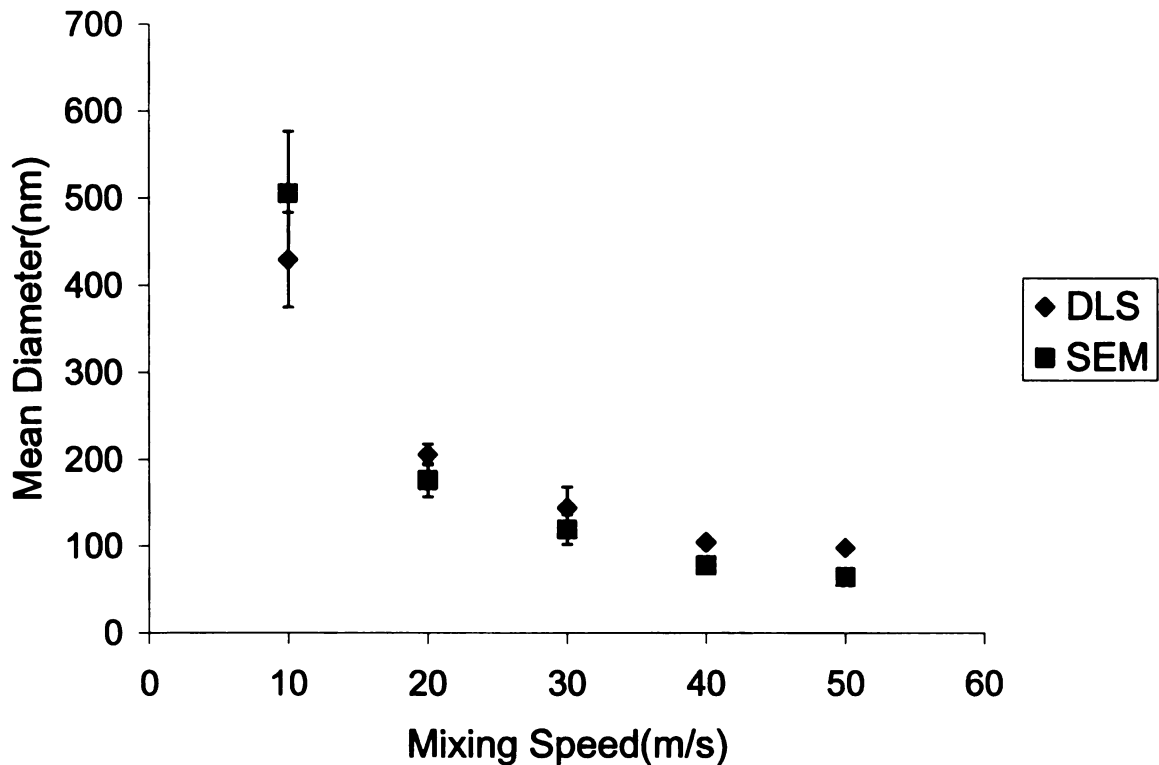


Figure 6.18: Mean diameter of the particles as obtained from DLS and as calculated from SEM images.

As discussed in previous section the particles obtained from emulsion diffusion had large coefficient of variation and after observing the SEM images it can be inferred that particle size distribution is bimodal in nature. Particles can be divided into set of two particle size distribution with different means.

The particle sizes that were measured from images were divided into two set of particle size distributions. The particles were categorized by simply putting particles with diameter greater than an arbitrary choice of border diameter in larger particle size category and the rest in smaller size category. The mean and standard deviation for each set was calculated and are plotted in Figure 6.19.

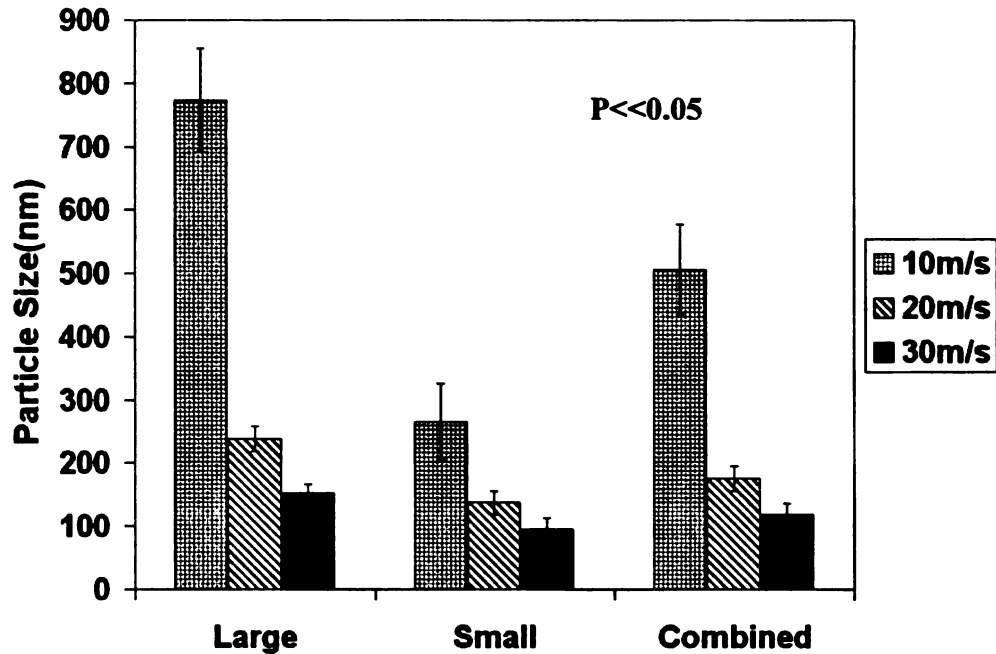


Figure 6.19: The particle sizes can be divided into two categories as large and small. The mean diameter of each categories is plotted at mixing speeds of 10m/s to 30m/s.

It was difficult to divide particles prepared at 40m/s and 50m/s as two set of particle distribution as the particle did not appear to be distinctively separable. But in 10m/s, 20m/s and 30 m/s it was more evident and particles were easily separable.

The emulsification was carried for varying time duration followed by diffusion step. Mean particle size was estimated by dynamic light scattering experiment. It was found that the particle size decreased with increasing mixing time at mixing speeds of 10 m/s to 30 m/s as shown in Figure 6.20. At higher mixing speeds of 40m/s and 50m/s, particle size increased sharply as emulsification time was increased. This phenomenon is similar to as observed in nanoprecipitation where higher mixing speeds led to the impingement and coalescence of PLA particles due to the increase in temperature beyond glass transition temperature of the PLA.

As illustrated in Figure 6.20 the particle size went down as the mixing time was increased ($P < 0.05$). It was most clear in the case of mixing speed of 10m/s. The emulsion was made by mixing ethyl acetate and water mix in nanomixer for different time period varying from 1 minute to 60 minutes. The mean particle size dropped from around 800 nm to 250 nm. Also the mean diameter of large particle size distribution and small particle size distribution from SEM image data match well with the mean diameter at 1 minute and 60 minutes (30 minutes for 30m/s) respectively.

Hence it shows that the mixing in nanomixer have different mixing zones with different flow conditions as illustrated in Figure 6.21. These different zones can have different turbulent conditions. As discussed in Section 6.2.2 the difference in turbulence conditions can lead to difference in the rate of energy dissipation in that zone. This difference in rate of energy dissipation can then affect the droplet size that is stable in that zone. Therefore, as the time is increased the percentage of droplets that passes through the zone with smaller droplet as stable diameter increases. Hence the particle size is reduced with increasing mixing time which as clearly evident at the mixing speed of 10m/s.

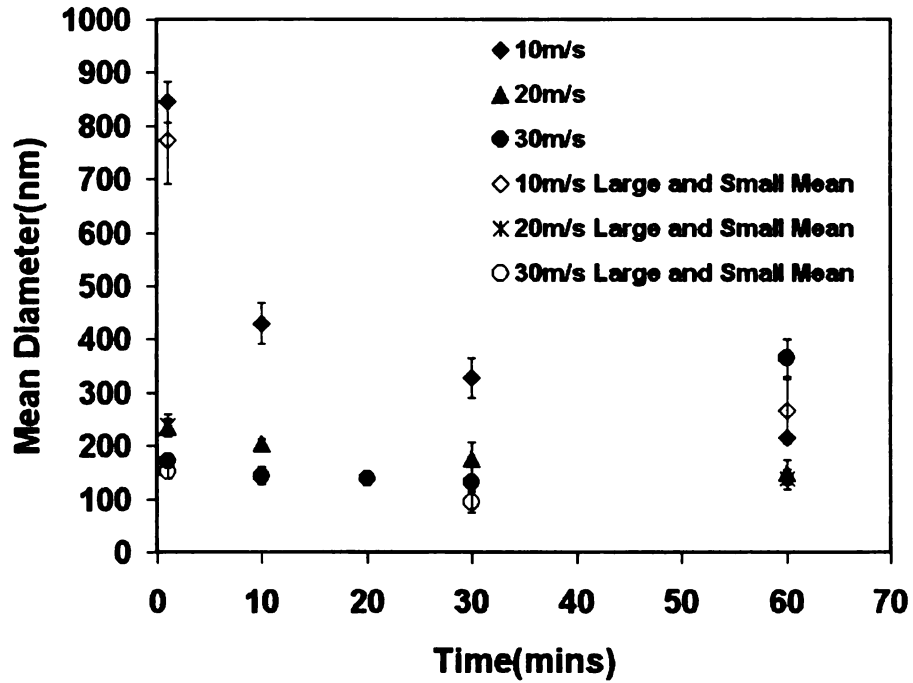


Figure 6.20: The mean diameter of particles at the different mixing times. Hollow legends are used to mark the large particle diameter and small particle diameter as observed in SEM images.

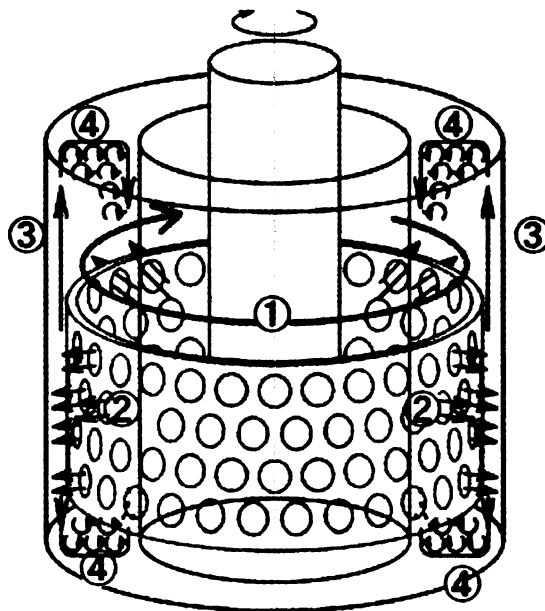
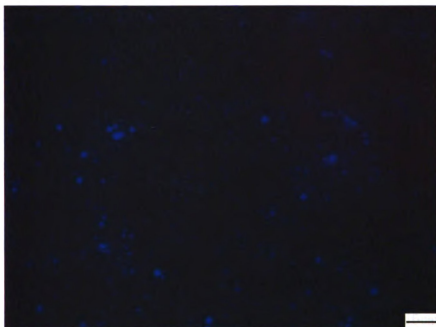


Figure 6.21: Illustrates the fluid motion inside the mixer and how emulsion droplet can encounter different turbulent conditions giving rise to difference in stable droplet size.

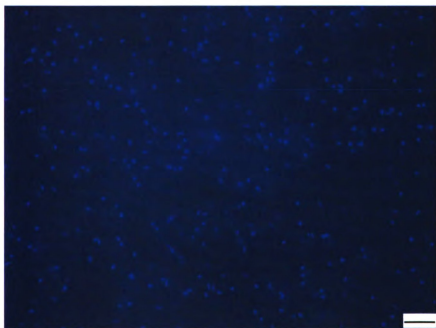
At the mixing speeds of 20m/s and 30m/s, the particle size decreased with increase in the mixing time from 1 minute to 60 minutes. But the decrease in particle size was not as remarkable as in the case of 10m/s. At 30m/s there was also increase in the particles size as they start to collide and coalesce together to form larger particles. With 40 m/s and 50m/s the particle size went up dramatically due to higher collision rate and coalescence of PLA particles (data not shown).

The coalescence of emulsion droplets at higher mixing speed was also qualitatively studied by addition of commercially available fluorescently tagged polystyrene particles of 1 micron mean diameter. The emulsion at 50 m/s second was prepared for 1 minute. Then the fluorescently tagged polystyrene particles were added to the emulsion. It was further mixed for 2 minutes at 50m/s and the diffusion step was carried out as described in experimental section. As a control pure fluorescently tagged polystyrene particles were mixed in nanomixer for 2 minutes at 50m/s. Both particles were taken and observed under optical microscope for signature fluorescence of polystyrene particles.

PLA emulsion with fluorescent particles and pure particles were imaged and are shown in Fig 6.22. As expected the pure polystyrene particles looked uniform in size under microscope whereas the particles mixed with emulsion appeared much larger in size. As there was random collision of particles inside the nanomixer, the emulsion droplets collided with fluorescent polystyrene particles and coalesced to give rise to larger fluorescent particles. Whereas in case of pure polystyrene particles as T_g of polystyrene is around 105°C [59] they collide but did not coalesce to form larger particles as the process was well below the T_g of polystyrene.



(a)



(b)

Figure 6.22: a) Optical image of fluorescent particles: PLA emulsion prepared at 50m/s for 1 minute followed by addition of 1 micron fluorescently tagged pure polystyrene particles and further mixing for 2 minutes at 50m/s. b) Pure 1 micron fluorescently tagged pure polystyrene particles mixed at 50m/s for 2 minutes. The length of scale bar in both the images is 20 μm .

6.4.3 Effect of addition of glycerol

Effect of addition of glycerol at the mixing speed of 50 m/s was also studied in the nanomixer. As discussed in section 6.2.2 changing viscosity has affect on the various parameters. Inertial diameter (d_{KH}) is independent of viscosity whereas eddy diameter (λ) and viscous diameter (d_{KV}) are a function of viscosity. Hence we can move from inertial regime ($\lambda < d_{KH}$) to viscous regime ($d_{KV} < \lambda$) by changing the viscosity of the continuous phase.

Different volume fraction of glycerol was added along with water. The particles were prepared by adding PLA solution in ethyl acetate to various volume fraction of water/glycerol mixture with 15mg/ml of Pluronic F68. The emulsification step was carried out at 50m/s for 1 minute and then the emulsion was added to pure water for diffusion step. The particle size was estimated by dynamic light scattering and is plotted in Figure 6.23.

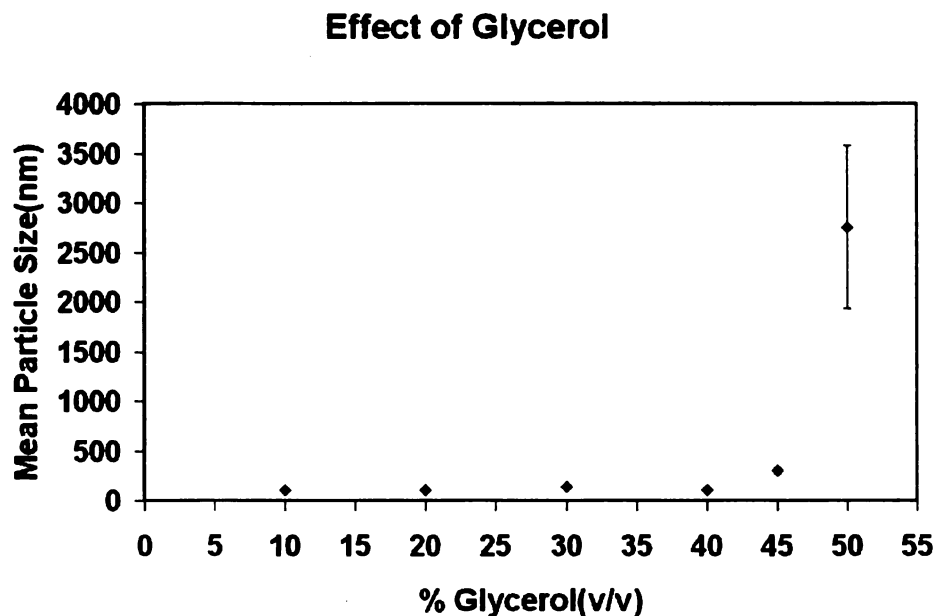


Figure 6.23 :The mean particle size as a function of glycerol volume fraction at mixing speed of 50 m/s.

The particle size remained constant until 40% volume fraction of glycerol and went up suddenly beyond that point. In the following Figure 6.24, all the three parameters: eddy diameter (λ) inertial diameter (d_{KH}) and viscous diameter (d_{KV}) are plotted along with mean diameter of particles as a function of glycerol volume fraction mixed at the mixing speed of 50m/s for 1 minute. The interfacial tension was calculated by using the theory of interfacial tension for partial miscible liquids where one liquid is mixture of water/glycerol and second liquid is ethyl acetate. For the case of partial miscible liquid, the formulation developed by Girifalco and Good [124] was used and is given in equation 6.28.

$$\gamma = \gamma_A + \gamma_B - 2(\gamma_A \gamma_B)^{1/2} \dots\dots\dots(6.28)$$

Where γ is the interfacial tension (N/m), γ_A is the surface tension of liquid A (N/m), γ_B is the surface tension of liquid B (N/m),.

For ethyl acetate, the literature value of surface tension at room temperature was used [124]. Water/glycerol system the surface tension was used from the plot as published by Connor et al [125]. Density and viscosity data was used from the physical properties of glycerol-water solution available in literature [126]. The values obtained were used to calculate the eddy diameter, inertial stable diameter (d_{KH}) and viscous stable diameter (d_{KV}).

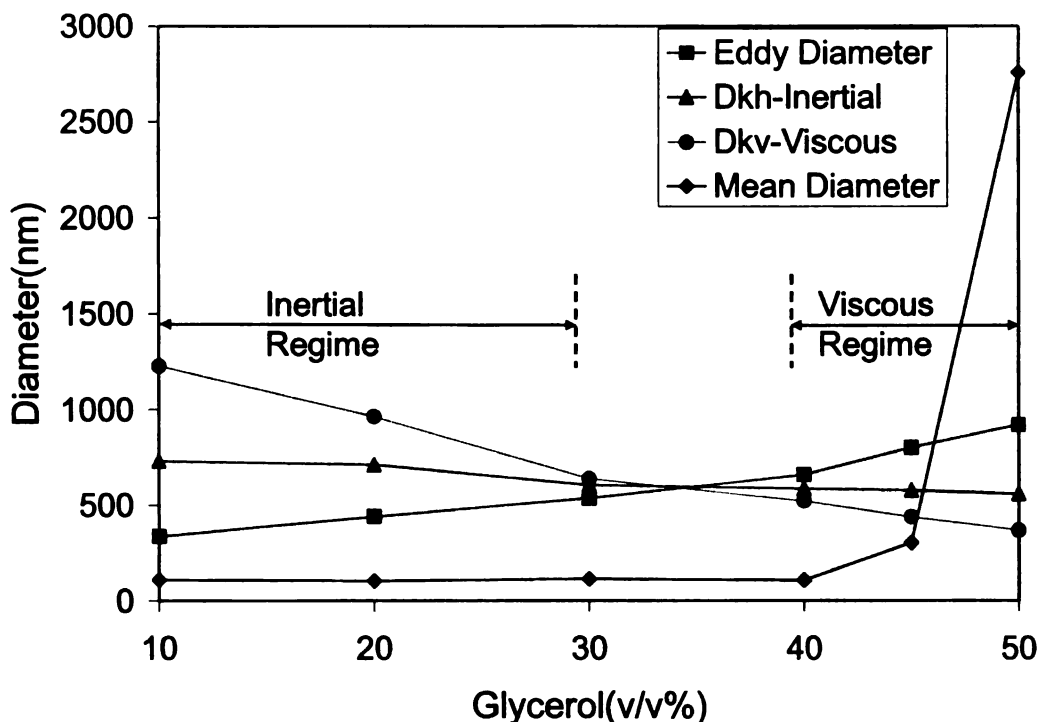


Figure 6.24: The above figure illustrates how the eddy diameter increases and is greater than both d_{KH} and d_{KV} at glycerol volume percentage greater than 35%. The mean diameter of particles for emulsion prepared at 50m/s for 1 minute also increased beyond 40%.

As shown in the Figure 6.24, eddy diameter is less than the d_{KH} for solution with glycerol volume percentage less than 30%. Hence the mixing is in the inertial turbulent regime. As discussed in section 6.2.2, the emulsion droplet size is governed by the equation which is independent of the viscosity. Therefore we do not observed a large change in particle size with increasing viscosity. But beyond 40% volume fraction of glycerol there was a sudden increase in the particle size with large standard deviation in mean. Also at 50% viscosity at 50m/s the temperature inside the vessel reaches $78 \pm 2^\circ\text{C}$ which is close to the boiling point of ethyl acetate. Hence it becomes an extremely complex system where the droplets are caught in eddies along with ethyl acetate

evaporating from the droplets. To determine whether mixing at high viscosity alone was the main reason for the particle size to increase, the emulsion step at 50m/s with 50% glycerol was done for 20 seconds. The particle size went down and is plotted in Figure 6.25. Figure 6.25 illustrates that the mixing time plays a critical role in controlling the particle size. As increasing the mixing time led to heating and it influenced the size of the particles as observed at 50% glycerol at 50 m/s.

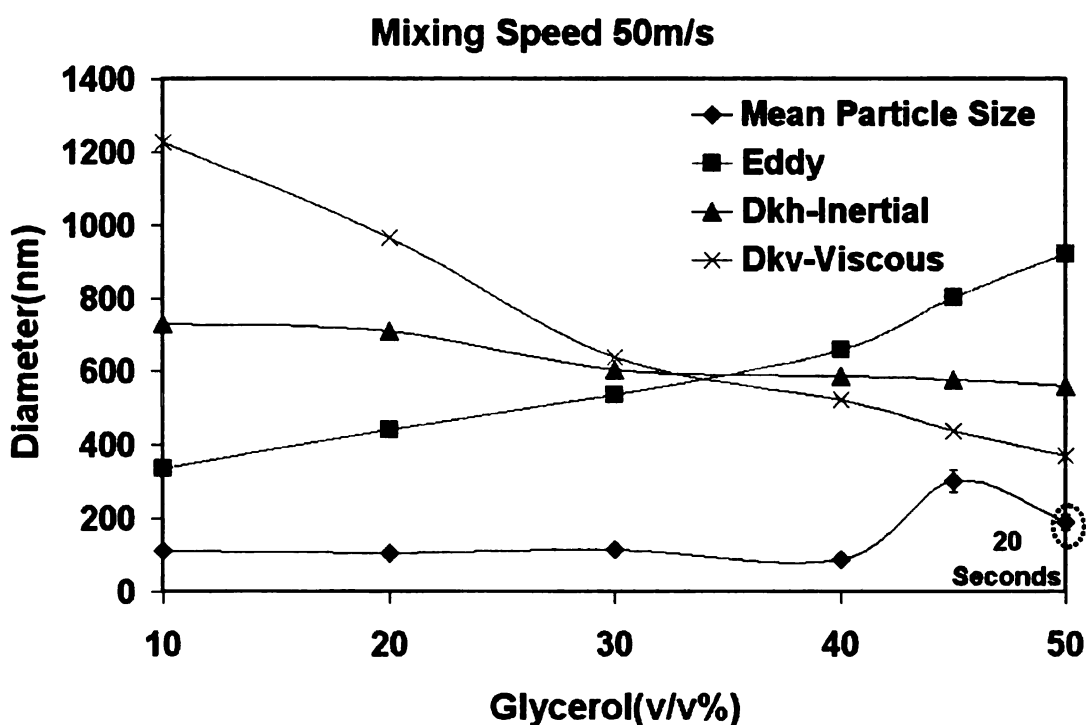
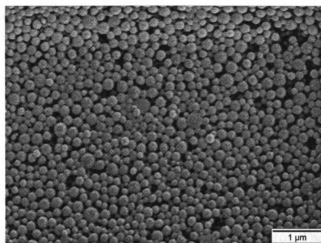


Figure 6.25: Mean particle size as a function of glycerol percentage. The mixing time at 50% glycerol was brought down to 20 seconds to avoid heating of the emulsion to 78°C.

Particle shape was also affected by the viscosity which in turn affects the heating inside the nanomixer. At 50% viscosity, the particles stayed spherical with 20 seconds of mixing time but when the mixing time was increased to 1 minute the particle shape changed from spherical to large hollow shells as shown Figure 6.26.



↓
From 20 sec
to 1 min

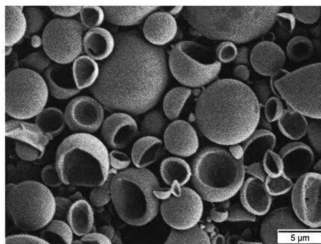


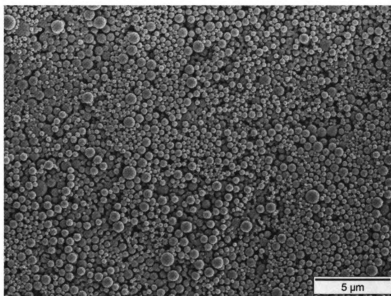
Figure 6.26: Effect of time on the particle size and shape at 50% glycerol at 50m/s mixing speed. Particles changed from solid nanospheres to micron sized hollow hemispherical shells.

The effect of glycerol leads to two simultaneous changes in condition: firstly it increases the viscosity of the continuous phase and secondly, it also increases the temperature inside the vessel. The temperature inside the vessel increased to $78\pm 2^{\circ}\text{C}$ which is close to boiling temperature of ethyl acetate. Hence to distinguish between two

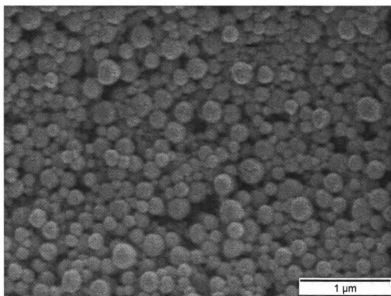
cases a series of experiments were done. The mixer has a cooling jacket, where the water is circulated to cool the vessel. The temperature in the outside jacket was maintained at 4°C for all the previous experiments. In first case the coolant temperature in the jacket around the mixing vessel was increased to 17°C for the 40% glycerol as continuous phase, so the temperature inside the vessel increases to the same temperature as $78 \pm 2^\circ\text{C}$. If it is only the heating that is causing particles to agglomerate into the shell structure we should observe similar particles as obtained with 50% glycerol. The particles obtained at 40% glycerol remained spherical and did not change shape to open shells. The image for particles obtained at 40% glycerol is shown in Figure 6.27a.

The other experiment was done where the emulsion was prepared at 20m/s for 10 minutes and was added to the heated mixture of 50% water and 50% glycerol by volume at 78°C, while it is being stirred in a beaker. The particles obtained remained spherical in shape as shown in Figure 6.27b illustrating heating alone itself does not cause particles to take shell shape. This also confirms that the nanomixer imparting high shear rate in viscous turbulent regime plays a critical role in particles taking the shape of shells. Transmission electron microscopy of particles, as shown in Figure 6.28a, before forming the shell shaped particles revealed that particles are not hollow and are solid particles.

Hence the change shape occurs because of combined influence of high temperature and high shear rate in viscous turbulent regime. It causes the particles to take peculiar shape as they are mixed in viscous turbulent regime. The viscous turbulent regime is illustrated in the Figure 6.28b, where the droplets are caught inside eddies.

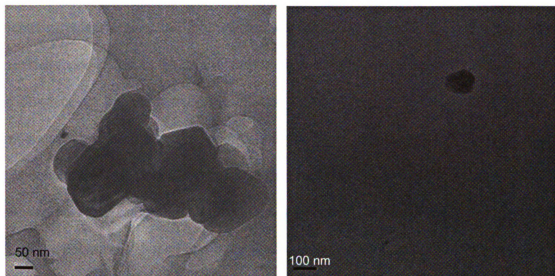


(a)

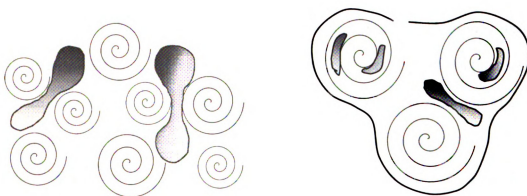


(b)

Figure 6.27: a) SEM image of particles formed at 40% glycerol when the internal temperature was raised to 78^oC. b) Particles formed by adding emulsion prepared at 20m/s for 10 minutes to water/glycerol (50% v/v) mixed in a beaker at 78^oC.



(a)



Inertial Regime

Viscous Regime

(b)

Figure 6.28: a. TEM image of PLA nanoparticles showing that the particles are not hollow. b) Illustrating the mixing condition in inertial and viscous turbulent regimes, in inertial turbulent regime droplets are outside eddies and in viscous turbulent regime they are trapped inside the eddies.

In inertial regime as discussed in Section 6.2.2 the eddy diameter is less than the stable droplet diameter and the droplets are located outside the eddies whereas in the viscous turbulent regime the droplets are located inside the eddies. As the viscosity is increased there is shift in the mixing regime from inertial to viscous turbulent regime and the droplets are caught inside eddies. Also involved is the heating of the system to temperatures around the boiling point of ethyl acetate that causes these droplets to lose ethyl acetate and this polymer containing droplets coalesce and grow larger as has been observed in other cases as well. But as this coalescing droplets are caught inside the eddies the polymer is shaped into open shell due to combined effect of evaporating ethyl acetate and sustained shape due to rotational motion of the surrounding eddy. Figure 6.29 illustrates the possible process where droplets are caught in the eddy and coalesce to form bowl shaped particle. Hence the final shape of open bowl is obtained. Similar shapes have also been obtained just by evaporation of solvent by Xia et al [127]. In their set-up they freeze dried the emulsion to form hollow spherical shell. The emulsion of poly-methyl metha acrylate was made and froze it in liquid nitrogen. Toluene was evaporated under vacuum at temperature below 0°C . Temperature below zero was needed to prevent collapse of hollow particles from pressure exerted by liquid water [127].

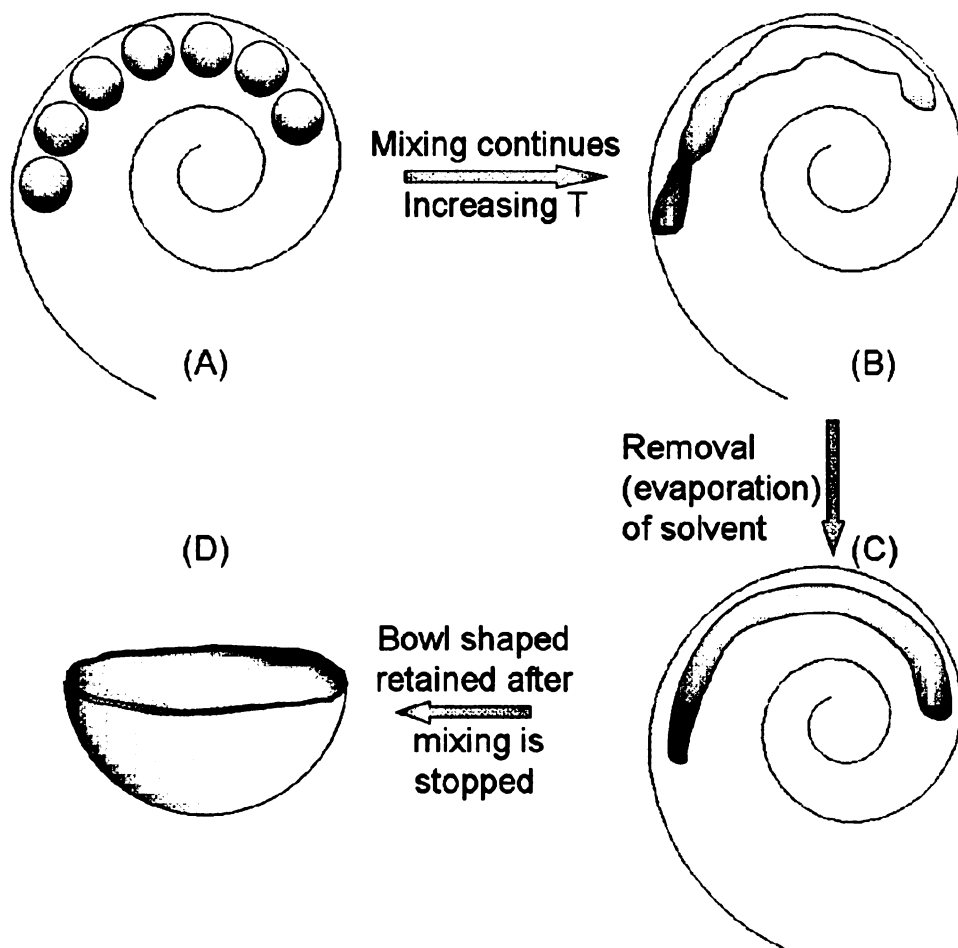


Figure 6.29: Scheme of the fabrication of bowl-shaped polymer particles in a turbulent eddy. At a short mixing time emulsion droplets caught in an eddy. Flow induced self-assembly of nanoparticles in an eddy. (B) At a long mixing time, emulsion droplets start coalescing in an eddy. (C) Solid form after loss of solvent. (D) Bowl shaped polymer particle.

In our case the particles retained the shape because droplets were caught in eddies and rotation caused particles to maintain its shape while the ethyl acetate was evaporating away from the emulsion. This was not true in the case where the emulsion was added to the glycerol water mixture in a beaker and spherical particles were observed. So the nanomixer unique ability to have turbulent conditions inside the vessel caused the emulsion droplets to coalesce and give rise to these unique shapes of polymer shells. We

also looked at the 60% glycerol system and mixing speed of 40m/s. We observed, as shown in Figure 6.30, similar trend where particles under viscous turbulent conditions combined to form open shell structure as was observed in with 50% glycerol.

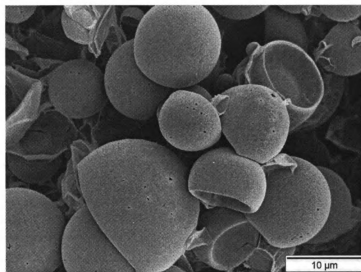


Figure 6.30: Scanning electron micrograph of poly-lactic acid open shells obtained by mixing at 40m/s at 60% glycerol by volume for 4 minutes.

The effect of mixing speed at 50% glycerol was also studied. As the mixing is in viscous turbulent regime at the speeds from 10m/s to 50m/s and if we substitute the viscosity at the maximum temperature that is measured inside the vessel in the equations discussed in section 6.2.2 we observe that the droplet size is unchanged beyond the mixing speed of 30m/s. The particle size should be constant from 30 m/s to 50 m/s. But at 50m/s, even with smaller mixing times, the particle size was slightly greater than that of the particle size obtained at 30m/s. This could be because at 50m/s at 50% glycerol the temperature reaches 78°C; this remarkably brings down the viscosity of the whole

continuous phase and also the temperature is slightly above the boiling point of ethyl acetate.

The particle size, the eddy diameter and the stable viscous diameter- d_{KV} are shown in Figure 6.31 and it can be seen that the d_{KV} is almost steady from mixing speed of 30m/s to 50 m/s. The measured particle size using DLS is also shown in the plot and they seemed to follow similar trend as expected. Hence we obtained smaller particles without running the mixer at maximum speed as the particle size is affected by a combination of various parameters like viscosity and rate of energy dissipation. Therefore, smallest size can be obtained by not operating at maximum mixing speed.

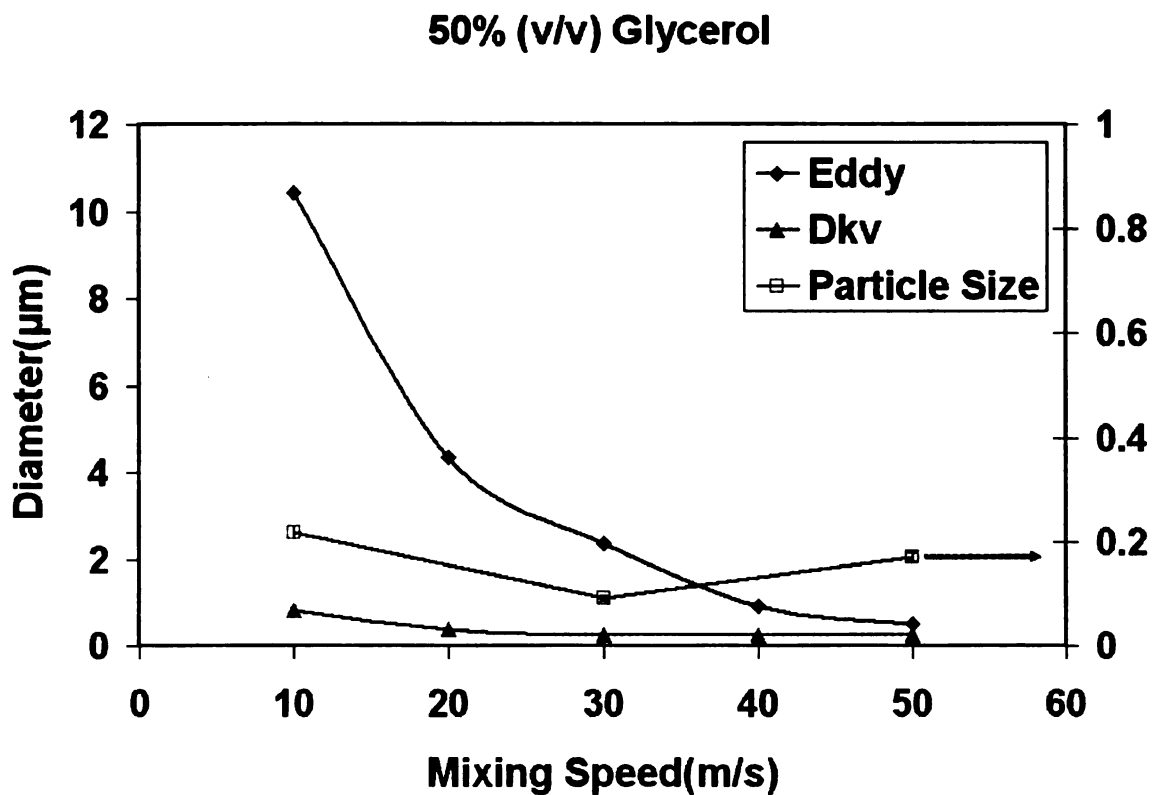
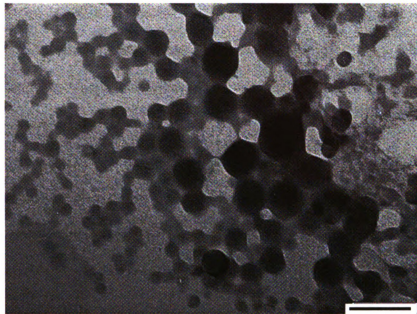


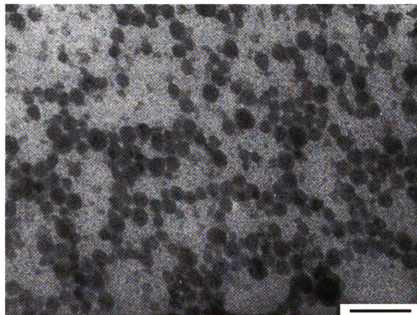
Figure 6.31: Effect of mixing speed on particle size at 50% glycerol volume percent. At all the speeds it is in viscous turbulent regime and the droplet size achieves a stable size at 30m/s. The mean particle size also reached minima at 30m/s and slightly increased at 50m/s.

Transmission electron microscopy of PLA particles obtained at 30m/s with 50% glycerol is shown in Figure 6.32. Significant portion of particles looked smaller than $87 \text{ nm} \pm 4 \text{ nm}$ mean diameter as measured by dynamic light scattering experiment in solution. The mean diameter of these smaller particles as measured from TEM images was around $32 \text{ nm} \pm 6 \text{ nm}$. As the whole mixing in nanomixer is a dynamic process with continually changing temperature and viscosity initially. When the mixer is started it takes 10 to 30 seconds for the solution to achieve a steady state in terms of temperature. As viscosity is a strong function of temperature viscosity keeps on changing initially. Also at 50% glycerol, the mixing is in viscous turbulent regime and the droplet diameter is a function of viscosity. Therefore, during that initial time period, droplets might feel higher viscous drag due to higher viscosity. Hence we get a portion of particles with small diameter. It was not as evident at lower glycerol percentages as the mixing is in inertial turbulent regime and the diameter of droplets is independent of the viscosity and by increasing mixing time the particle size can be made smaller.

We calculated theoretically, if the values to viscosity are chosen at the initial temperature of 4°C , the stable droplet diameter is 60% of what it would be if the droplet diameter was calculated using the maximum temperature reached inside the mixer. Hence in viscous turbulent regime there is significant portion of particle size that stays much smaller than the larger particles. Also the coefficient of variation at 30m/s, 50% glycerol is much larger at 46% whereas the coefficient of variation at 30m/s, no glycerol present, is 15%. The coefficient of variation for just the smaller particles as seen in Figure 6.32 B is 22%.



(A)



(B)

Figure 6.32: TEM images of PLA nanoparticles prepared at 30 m/s with 50% glycerol. A) Shows the particles images with relatively larger particles. B) PLA nanoparticles with mean diameter around 30 nm. The scale bar in both the images is 100 nm.

6.5 EFFECT OF ELECTRON BEAM ON PLA PARTICLES

6.5.1 Poly-Lactic Acid and Beam Damage

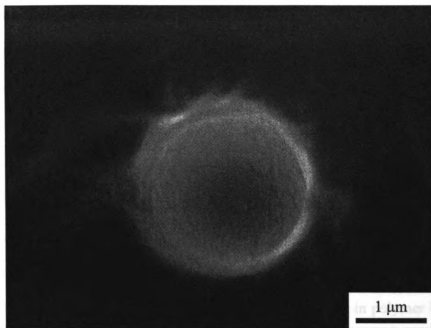
Poly-lactic acid (PLA) is extensively used as biomaterial for its biocompatibility and biodegradability. Poly-lactic acid, though insoluble in water, is hydrolyzed by water and can be degraded by ester hydrolysis [128]. The rate of hydrolysis is conventionally governed by glass transition temperature, crystallinity and molecular weights. Recently, studies have been done to understand the behavior of biopolymers under the influence of radiations. Poly-lactic acid and other biopolymers like Poly(lactide-co-glycolide) (PLGA) can have their properties altered by exposing the polymer to high energy electron beam [129]. Boey et.al. showed that PLA and PLGA can have their properties altered by exposing them to the electron beam.

The main mechanism of polymer degradation as given by radiation chemistry is as follows. The polymer materials get excited under the exposure of radiation to form active species, such as cations, anions or radicals [130]. These active species are able to react among the polymeric chains or can react with one another giving rise to changes in the material properties. The combination of two radicals leads to cross-linking, while the chain transfer and subsequent splitting lowers the molecular weight [129, 130]. The electron beam energy can directly disrupt the attractive forces the atoms, thus disrupting the molecules [129, 130]. This radiation energy breaks the chemical bonds causing chain scission. As a result, a radiation source of shorter wavelength and higher frequency or energy, often packs sufficient energy to cause chain scission through the breaking of these chemical bonds.

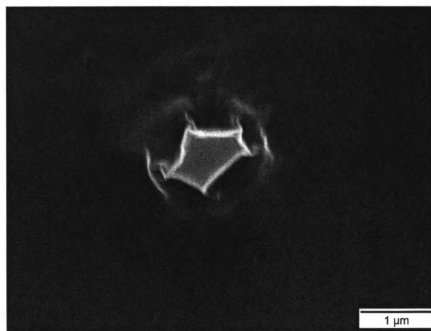
6.5.2 Deformation of PLA Particles by Electron Beam

The electron beam has dramatic effect on the poly-lactic acid particles. As mentioned in the previous section the electron beam can cause polymer chains to break down and they can undergo transformation giving rise to different thermal and morphological properties. As shown in Figure 6.33a, the poly-lactic acid particle is shown before beam damage and Figure 6.33b shows particles after damage. The particles were imaged under a field emission scanning electron microscope with 10KV of accelerating voltage at a working distance of 15 mm.

As PLA particles can not be viewed directly under electron microscope, the particles were also coated with 7 nm of gold for imaging. The particles were imaged at a low magnification so large area was scanned and the exposure of particle to beam was limited. The particle was imaged at low magnification at a scan rate of 20 sec/frame and then the particle was exposed to electron beam for 30 seconds by increasing the magnification 3-4 times. The PLA particle was damaged and deformed due to the high energy electron beam. As discussed in previous section it has been observed that poly-lactic acid can get damaged by electron beam because of chain scission by high energy electrons. As the energy of electron is sufficiently high it can simply break the atom-atom bonds. It can cause molecular weight of polymer to go down. The morphology of polymer can change as amorphous region in polymer can become more crystalline due to rearrangement of these shorter polymer chains as was observed by Boey *et. al.* Boey *et al* also observed that breaking of poly-lactic acid can also lead to release of carbon dioxide from the polymer.



(a)



(b)

Figure 6.33. Polylactic acid (a) before and (b) after exposure to 10KeV electron beam.

A control experiment was conducted by dissolving polylactic acid in acetone and drop coating a film on a glass slide. It was done to confirm if the deformation was enhanced due to the processing in high shear rate nanomixer. The drop coated polymer film was again coated with a 7 nm film of gold and was investigated using a FESEM at an accelerating voltage of 10KV. The drop coated polymer film was also damaged due to the electron beam confirming that the deformation is because of beam damage to polymer and processing with nanomixer did not induce any change to polymer physical properties. We also carried out differential scanning calorimetry (DSC) and thermal gravimetric analysis (TGA) for PLA particles and did not find any difference in polymer before and after processing in nanomixer. DSC did not show any change in the glass transition temperature of PLA or any change in physical properties of PLA. Whether there is any residual solvent that might be getting released during electron beam damage was tested by TGA. TGA also was exactly the same as for pure PLA and had no evidence of any trapped mass within the polymer that could cause the deformation in particles.

Figure 6.34 shows the image of polymer film formed by drying PLA solution in acetone before and after the electron beam damage. It is visible that the PLA film deforms on the exposure of electron beam. As it is evident from comparison of images (a) before damage and (c) after damage that the film is damaged and has sagged where it was exposed to the beam. It also provides indirect evidence that nanomixer processing does not have any influence on the deformation behavior and is induced by the high energy carried by the electrons as evident clearly from images (b) and (d).

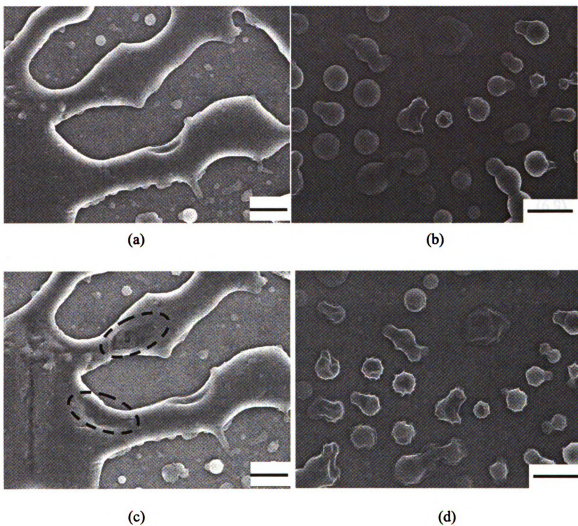


Figure 6.34: The effect electron beam damage on PLA film dried on a glass slide coated with 7 nm gold film. (a) and (b) is an image of PLA film before damage and (c) and (d) are the images of same area after electron beam damage. The length of scale bar in each image is 5 μm .

6.5.3 Effect of Gold Coating on the Poly-Lactic Acid Deformation

As discussed in previous section the electron beam is causing the poly-lactic acid particles to deform. We studied the influence of gold film that is used to view the poly-lactic acid in the SEM. Electron beam has a certain penetration depth depending on the material property and beam energy. For a bulk sample the beam penetration depth (D) can be estimated by an approximation developed by Kanaya Okayama [131] and is given by following equation.

$$D (\mu\text{m}) = 0.0276AE_0^{1.67}Z^{-0.89}\rho^{-1} \dots\dots\dots(6.9)$$

Where: A is the atomic weight (g/mole), Z is the atomic number, ρ is the density (g/cm³), E₀ is electron beam energy (KeV) .The depth of penetration for gold and PLA is tabulated in the following table for different accelerating voltages.

Table 6.2: Beam penetration depth for PLA and gold as a function of accelerating voltage

Accelerating Voltage (KV)	Beam penetration Depth(nm)	
	Gold	PLA
10	270	2500
3	36	330

If the thickness of the materials is less than the beam penetration depth then the electron beam interaction with that material can be divided into three parts, fraction absorbed (f_A), fraction transmitted (f_T) and fraction back scattered (f_B). In case of polylactic acid coated with a thin layer of gold, the fraction of transmitted beam would cause damage to the underlying polymer film. Hence we studied the effect of varying the gold film thickness by coating 7 nm, 35 nm and 70 nm gold film on polylactic acid.

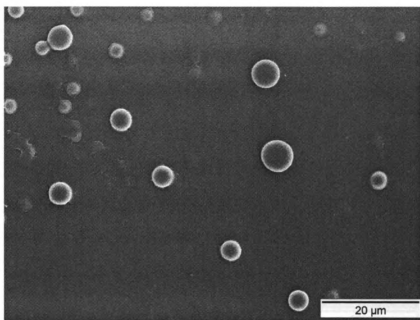
As the thickness of gold is increased it should reduce the effect of beam damage on the polylactic acid. This was observed on poly-lactic acid during SEM. Figures 6.35, 6.36 and 6.37 illustrates the effect of beam damage of poly-lactic acid that has been coated with 7nm, 35 nm and 70 nm of gold films.

As can be seen, the damaging effect of electron beam with 10KeV of energy is reduced as the thickness of the film is increased. This is because the fraction of electrons that can pass through the gold film reduces as the thickness is increased, as discussed by Dapor *et. al.* Dapor developed a model to quantify the fraction of beam that can pass through any materials by doing an iteration scheme that estimates f_A , f_T and f_B [132]. It assumes a certain thickness of material (ξ) and adds a small thickness ($\Delta\xi$) to existing thickness and estimate the change in the three fractions.

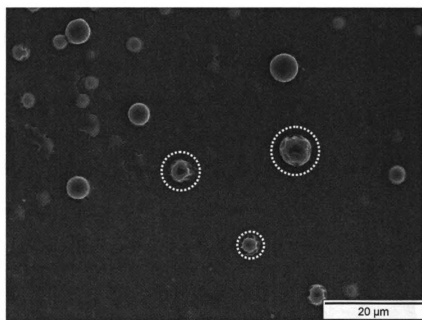
The beam damage is reduced because more electrons are either back scattered or absorbed by the gold film as the thickness is increased as illustrated in Figure 6.38. The beam has exaggerated tapering though typical angle is $\sim 0.3^\circ$. The fraction of beam transmitted at different thicknesses at accelerating voltage of 10KV is given in Table 6.3. As seen from the table, the fraction of electrons transmitted is very low at 70nm that there is not sufficient damage to observe drastic change in the particle shape and size.

Table 6.3 Fraction of beam (10 KV) transmitted at different gold film thicknesses [132]

Gold Film Thickness(nm)	Fraction Transmitted (%)
7	98%
35	62%
70	20%

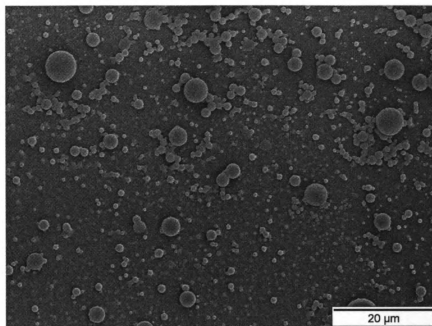


(a)

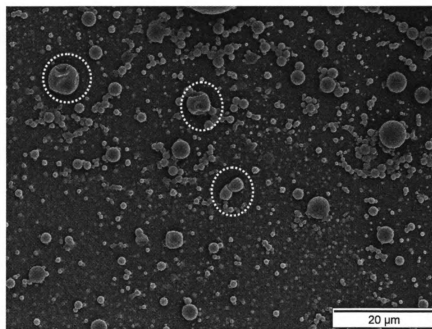


(b)

Figure 6.35: SEM image of PLA particles coated with 7 nm of gold film (a) before damage and (b) after damage by 10KeV electron beam.

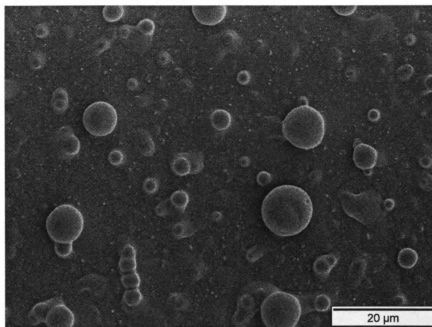


(a)

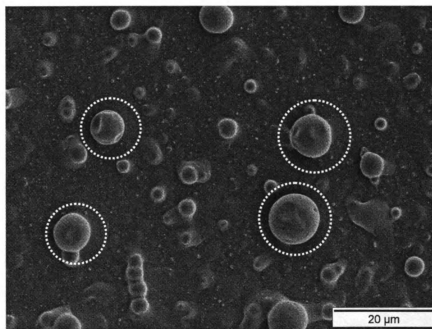


(b)

Figure 6.36: SEM image of PLA particles coated with 35 nm of gold film (a) before damage and (b) after damage by 10KeV electron beam.

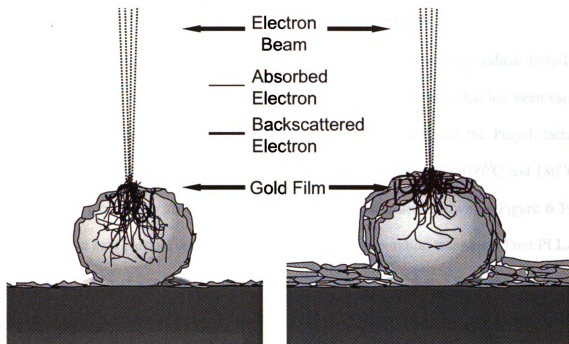


(a)

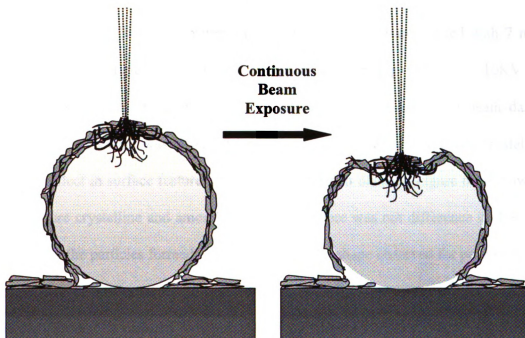


(b)

Figure 6.37: SEM image of PLA particles coated with 70 nm of gold film (a) before damage and (b) after damage by 10KeV electron beam.



(a)



(b)

Figure 6.38: a) Illustrates how beam damage is reduced with increasing thickness of gold film over polylactic acid particle. b) Illustrates the shrinking of particles during electron beam damage.

6.5.4 Effect of Structure of Poly-Lactic Acid on Deformation

Effect of PLA structure on damage by electron beam was also studied. Poly-L-lactic acid (PLLA) has more crystallinity than the poly-DL-lactic acid that has been used for previous studies. Differential scanning calorimetry revealed that the Poly-L-lactic acid has a recrystallization peak and melting point peak present at the 100°C and 180°C respectively which was absent in the case of poly-L-lactic acid shown in Figure 6.39. Poly-L-lactic acid particles were prepared by emulsion evaporation technique. First PLLA was dissolved in chloroform at the concentration of 15 mg/ml and then emulsion was formed by adding 2 ml of PLLA solution in 6 ml of DI water with 15mg/ml of surfactant, Pluronic F68. Emulsification was done in bath sonicator for 1 hour. This was followed by evaporation step under partial vacuum for 2 hours.

The particles were again drop coated on a glass slide and coated with 7 nm of gold film. The particles were imaged under the accelerating voltage of 10KV. The particle before and after beam damage are shown in Figure 6.40. The beam damage appears similar to what was observed for amorphous poly-lactic acid hence crystallinity does not reflect in surface feature that change with beam damage. Figure 6.41 shows the TGA of pure crystalline and amorphous PLA and there was not difference in the TGAs obtained for the particles formed. Hence the change in shape observed for poly-lactic acid particles can be attributed to the beam damage done by high energy electrons in SEM. This damage can be reduced by coating PLA particles with thicker layer of gold or by imaging the particles at low accelerating voltage in SEM.

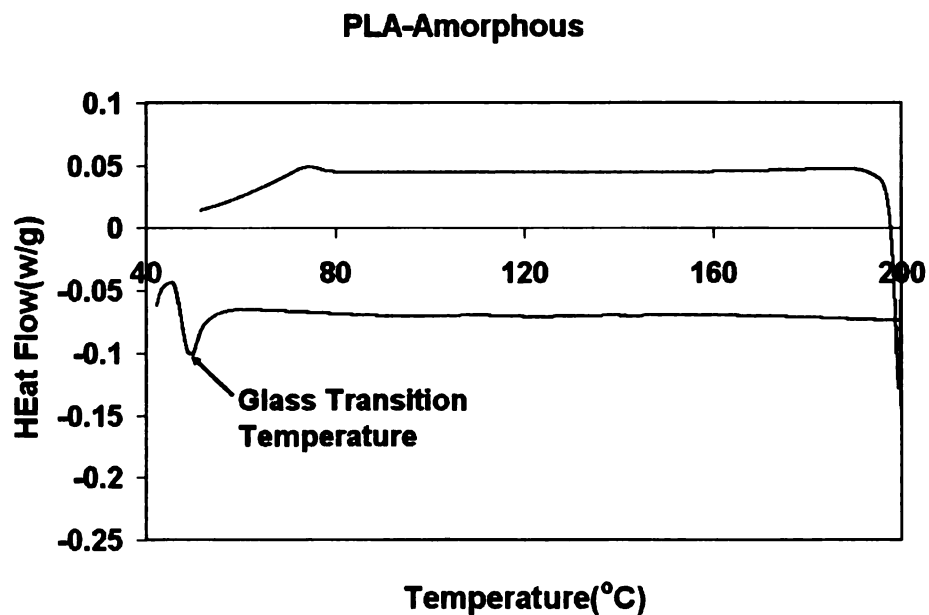
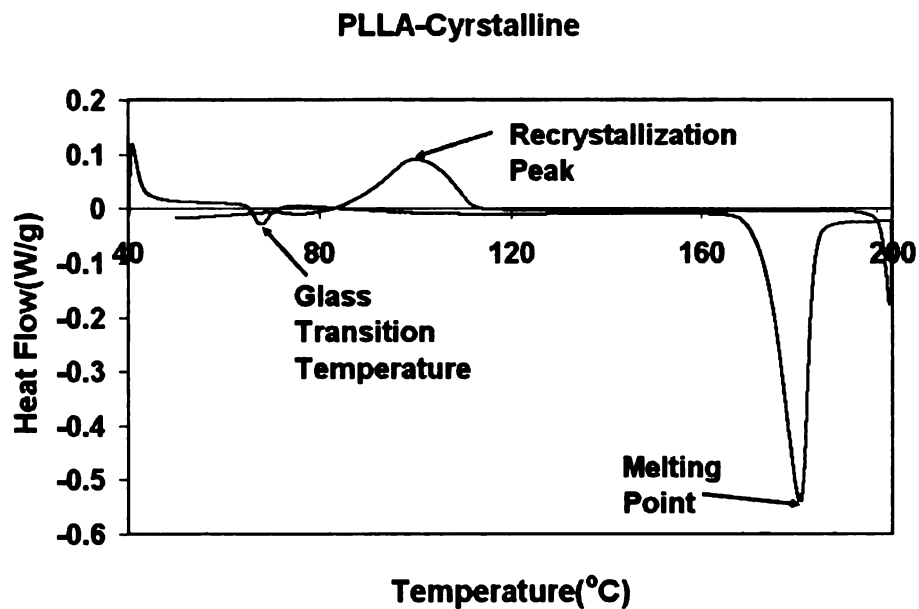
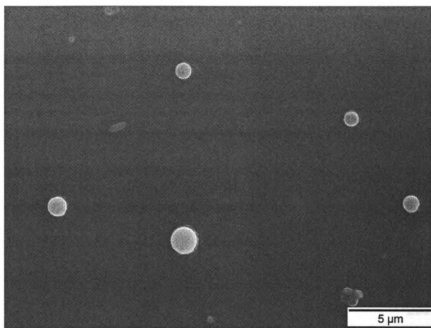
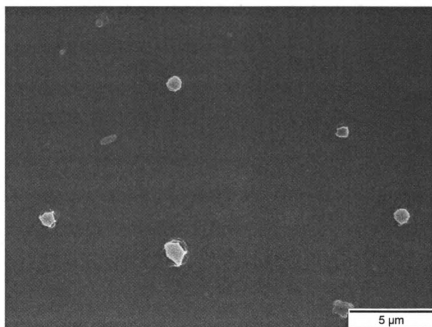


Figure 6.39: DSC curves for poly-lactic acid: a) Crystalline and b) Amorphous.



(a)



(b)

Figure 6.40: SEM images of PLLA particles coated with 7 nm of gold film a) before and b) after damage.

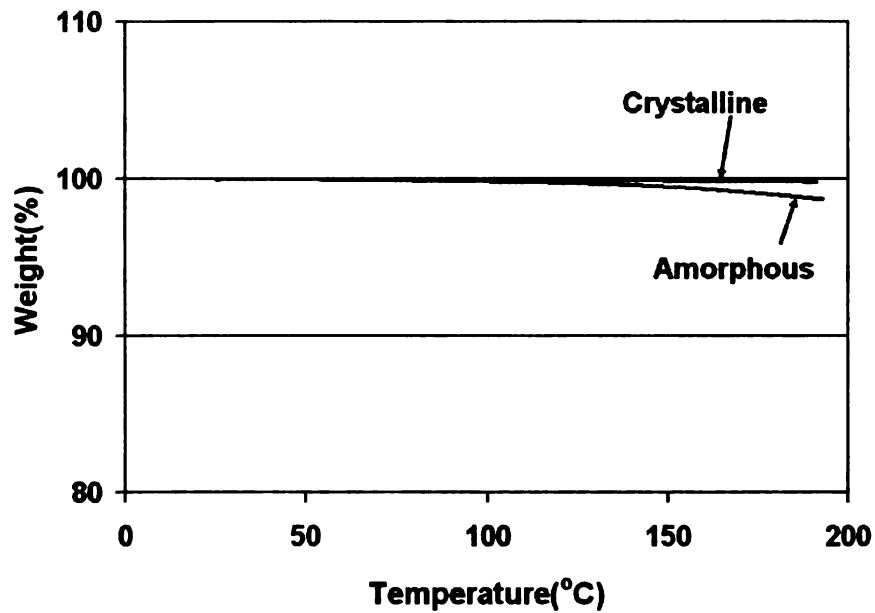


Figure 6.41: Thermogravimetric Analysis of crystalline and amorphous poly-lactic acid revealed that there was not significant mass loss in the PLA particles fabricated in the nanomixer and the shape change is due to the beam damage caused by the electron beam.

6.6 CONCLUSIONS AND FUTURE WORK

In this chapter we have developed a fast and efficient way to fabricate poly-lactic acid nanoparticles using the high shear rate nanomixer. The influence of shear rate is evident in both nanoprecipitation as well as emulsion diffusion. High shear rate can form smaller particles in case of emulsion diffusion process but can also lead to agglomeration and coalescence of particles due to high temperatures inside the mixer. In emulsion diffusion the particle size went down with increasing mixing speeds but is controlled by mixing time. Longer mixing time led to the coalescence of droplets to form larger particles and is true for different kinds of particles as shown with gold nanoparticles and polystyrene fluorescent particles.

Varying the viscosity also can influence the shape and size of the particles by shifting from inertial to viscous turbulent regime. It was also evident that the coalescence of droplets can be completely different at high viscosities. The droplets at high viscosity can lead to shell shaped structures that are formed by droplets getting caught inside the eddy and coalescing at the same time. The PLA particles are also influenced by the electron beam under SEM. This happens because the electrons in the beam can have sufficient energy to damage the PLA chains and deform the particle shape. It can be reduced by increasing the gold coating that needs to be done on PLA particles before imaging them under SEM. The increasing gold thickness dramatically reduces the transmitted beam fraction, hence reducing the extent of the damage done to the PLA particles.

There is a lot of scope for future work while studying the influence of nanomixer in nanoprecipitation and emulsion diffusion. As the particles have tendency to

agglomerate or coalesce in the mixer, two different kinds of phases or materials can be mixed to form biphasic or composite particles. Also in the emulsion diffusion method, the influence of deuterated water on the emulsion formation can be studied. Further experiment to study the influence of particles shape in viscous turbulent regime can be carried out by controlling the viscosity and mixing conditions inside the vessel.

REFERENCES

1. Briseno, A.L., et al., *Patterning organic single-crystal transistor arrays*. Nature, 2006. **444**(7121): p. 913-917.
2. Arumugam, P., et al., *'Bricks and mortar' nanoparticle self-assembly using polymers*. Polymer International, 2007. **56**(4): p. 461-466.
3. Betancourt, T., B. Brown, and L. Brannon-Peppas, *Doxorubicin-loaded PLGA nanoparticles by nanoprecipitation: preparation, characterization and in vitro evaluation*. Nanomedicine, 2007. **2**(2): p. 219-232.
4. Ganachaud, F. and J.L. Katz, *Nanoparticles and nanocapsules created using the Ouzo effect: Spontaneous emulsification as an alternative to ultrasonic and high-shear devices*. Chemphyschem, 2005. **6**(2): p. 209-216.
5. Chaudret, B. and K. Philippot, *Organometallic nanoparticles of metals or metal oxides*. Oil & Gas Science and Technology-Revue De L Institut Francais Du Petrole, 2007. **62**: p. 799-817.
6. Liao, H.W., C.L. Nehl, and J.H. Hafner, *Biomedical applications of plasmon resonant metal nanoparticles*. Nanomedicine, 2006. **1**(2): p. 201-208.
7. Alekseeva, A.V., et al., *Gold nanorods: Synthesis and optical properties*. Colloid Journal, 2006. **68**(6): p. 661-678.
8. Murphy, C.J., et al., *Anisotropic metal nanoparticles: Synthesis, assembly, and optical applications*. Journal of Physical Chemistry B, 2005. **109**(29): p. 13857-13870.
9. Bauer, L.A., N.S. Birenbaum, and G.J. Meyer, *Biological applications of high aspect ratio nanoparticles*. Journal of Materials Chemistry, 2004. **14**(4): p. 517-526.
10. Ai, S.F., et al., *Highly flexible polyelectrolyte nanotubes*. Journal of the American Chemical Society, 2003. **125**(37): p. 11140-11141.
11. Baughman, R.H., A.A. Zakhidov, and W.A. de Heer, *Carbon nanotubes - the route toward applications*. Science, 2002. **297**(5582): p. 787-792.
12. Lutkenhaus, J.L. and P.T. Hammond, *Electrochemically enabled polyelectrolyte multilayer devices: from fuel cells to sensors*. Soft Matter, 2007. **3**(7): p. 804-816.

13. Hussain, F., et al., *Review article: Polymer-matrix nanocomposites, processing, manufacturing, and application: An overview*. Journal of Composite Materials, 2006. **40**(17): p. 1511-1575.
14. Guo, M.L., et al., *Carbon nanotubes-based amperometric cholesterol biosensor fabricated through layer-by-layer technique*. Electroanalysis, 2004. **16**(23): p. 1992-1998.
15. Carrillo, A., et al., *Noncovalent functionalization of graphite and carbon nanotubes with polymer multilayers and gold nanoparticles*. Nano Letters, 2003. **3**(10): p. 1437-1440.
16. Nie, Z.H. and E. Kumacheva, *Patterning surfaces with functional polymers*. Nature Materials, 2008. **7**(4): p. 277-290.
17. Diegoli, S., et al., *Engineering nanostructures at surfaces using nanolithography*. Proceedings of the Institution of Mechanical Engineers Part G-Journal of Aerospace Engineering, 2007. **221**(G4): p. 589-629.
18. Gimzewski, J.K. and C. Joachim, *Nanoscale science of single molecules using local probes*. Science, 1999. **283**(5408): p. 1683-1688.
19. Hendricks, T.R., et al., *Intact pattern transfer of conductive exfoliated graphite nanoplatelet composite films to polyelectrolyte multilayer platforms*. Advanced Materials, 2008. **20**(10): p. 2008-+.
20. Wilbur, J.L., et al., *Microfabrication by Microcontact Printing of Self-Assembled Monolayers*. Advanced Materials, 1994. **6**(7-8): p. 600-604.
21. Xia, Y.N., et al., *Complex optical surfaces formed by replica molding against elastomeric masters*. Science, 1996. **273**(5273): p. 347-349.
22. Luo, G., et al., *Nanoimprint lithography for the fabrication of interdigitated cantilever arrays*. Nanotechnology, 2006. **17**(8): p. 1906-1910.
23. Maury, P., et al., *Directed assembly of nanoparticles onto polymer-imprinted or chemically patterned templates fabricated by nanoimprint lithography*. Advanced Materials, 2005. **17**(22): p. 2718-+.
24. Zhang, F.X. and H.Y. Low, *Ordered three-dimensional hierarchical nanostructures by nanoimprint lithography*. Nanotechnology, 2006. **17**(8): p. 1884-1890.
25. Cui, H.G., et al., *Block copolymer assembly via kinetic control*. Science, 2007. **317**(5838): p. 647-650.

26. Hales, K., et al., *Nanoparticles with tunable internal structure from triblock copolymers of PAA-b-PMA-b-PS*. *Nano Letters*, 2008. **8**(7): p. 2023-2026.
27. Decher, G., *Fuzzy nanoassemblies: Toward layered polymeric multicomposites*. *Science*, 1997. **277**(5330): p. 1232-1237.
28. Jiang, C.Y. and V.V. Tsukruk, *Freestanding nanostructures via layer-by-layer assembly*. *Advanced Materials*, 2006. **18**(7): p. 829-840.
29. Wang, Y., A.S. Angelatos, and F. Caruso, *Template synthesis of nanostructured materials via layer-by-layer assembly*. *Chemistry of Materials*, 2008. **20**(3): p. 848-858.
30. Srivastava, D. and I. Lee, *Nanorice and nanospears from polymer nanospheres*. *Advanced Materials*, 2006. **18**(18): p. 2471-+.
31. Srivastava, D., T.R. Hendricks, and I. Lee, *Step-edge like template fabrication of polyelectrolyte supported nickel nanowires*. *Nanotechnology*, 2007. **18**(24).
32. Kohli, N., et al., *Nanostructured biosensor for measuring neuropathy target esterase activity*. *Analytical Chemistry*, 2007. **79**(14): p. 5196-5203.
33. Wang, H., et al., *Nanorice: A hybrid plasmonic nanostructure*. *Nano Letters*, 2006. **6**(4): p. 827-832.
34. Zhou, L.S., et al., *All-organic active matrix flexible display*. *Applied Physics Letters*, 2006. **88**(8).
35. Ozaki, M., S. Kratochvil, and E. Matijevic, *Formation of Monodispersed Spindle-Type Hematite Particles*. *Journal of Colloid and Interface Science*, 1984. **102**(1): p. 146-151.
36. Steinhart, M., et al., *Polymer nanotubes by wetting of ordered porous templates*. *Science*, 2002. **296**(5575): p. 1997-1997.
37. Zheng, R.K., H.L.W. Chan, and C.L. Choy, *A simple template-based hot-press method for the fabrication of metal and polymer nanowires and nanotubes*. 2005. **16**(9): p. 1928-1934.
38. Kohli, N., et al., *Nanostructured crosslinkable micropatterns by amphiphilic dendrimer stamping*. *Macromolecular Rapid Communications*, 2004. **25**(9): p. 935-941.
39. Steinhart, M., et al., *Nanotubes by template wetting: A modular assembly system*. *Angewandte Chemie-International Edition*, 2004. **43**(11): p. 1334-1344.

40. Wirtz, M. and C.R. Martin, *Template-fabricated gold nanowires and nanotubes*. *Advanced Materials*, 2003. **15**(5): p. 455-458.
41. Wirtz, M., et al., *Template-synthesized nanotubes for chemical separations and analysis*. 2002. **8**(16): p. 3573-3578.
42. Tokuda, N., et al., *Fabrication of Cu nanowires along atomic step edge lines on Si(111) substrates*. *Applied Surface Science*, 2004. **237**(1-4): p. 528-531.
43. Hernandez, J., et al., *Characterization of the surface structure of gold nanoparticles and nanorods using structure sensitive reactions*. *Journal of Physical Chemistry B*, 2005. **109**(26): p. 12651-12654.
44. Nair, S., S. Natarajan, and S.H. Kim, *Fabrication of electrically conducting polypyrrole-poly(ethylene oxide) composite nanofibers*. *Macromolecular Rapid Communications*, 2005. **26**(20): p. 1599-1603.
45. Aussawasathien, D., J.H. Dong, and L. Dai, *Electrospun polymer nanofiber sensors*. *Synthetic Metals*, 2005. **154**(1-3): p. 37-40.
46. Paramonov, S.E., V. Gauba, and J.D. Hartgerink, *Synthesis of collagen-like peptide polymers by native chemical ligation*. *Macromolecules*, 2005. **38**(18): p. 7555-7561.
47. Zhang, S.G., *Fabrication of novel biomaterials through molecular self-assembly*. *Nature Biotechnology*, 2003. **21**(10): p. 1171-1178.
48. Wang, J.G., et al., *Microstructure and interdiffusion of template-synthesized Au/Sn/Au junction nanowires*. *Nano Letters*, 2004. **4**(7): p. 1313-1318.
49. Liang, Z.J., et al., *Nanotubes prepared by layer-by-layer coating of porous membrane templates*. *Advanced Materials*, 2003. **15**(21): p. 1849-1853.
50. Johansson, A., et al., *Fabrication of high-aspect-ratio Prussian blue nanotubes using a porous alumina template*. *Nano Letters*, 2005. **5**(8): p. 1603-1606.
51. Mitchell, D.T., et al., *Smart nanotubes for bioseparations and biocatalysis*. *Journal of the American Chemical Society*, 2002. **124**(40): p. 11864-11865.
52. Steinle, E.D., et al., *Ion channel mimetic micropore and nanotube membrane sensors*. *Analytical Chemistry*, 2002. **74**(10): p. 2416-2422.
53. Zheng, R.K., et al., *A simple and convenient route to prepare poly(vinylidene fluoride trifluoroethylene) copolymer nanowires and nanotubes*. *Chemical Communications*, 2005(11): p. 1447-1449.

54. Han, W.Q., et al., *Formation and structure of boron nitride conical nanotubes*. Applied Physics a-Materials Science & Processing, 2000. **71**(1): p. 83-85.
55. Li, N.C., et al., *Conical nanopore membranes. Preparation and transport properties*. Analytical Chemistry, 2004. **76**(7): p. 2025-2030.
56. Grabar, K.C., et al., *Preparation and Characterization of Au Colloid Monolayers*. Analytical Chemistry, 1995. **67**(4): p. 735-743.
57. Qin, D., et al., *Fabrication of ordered two-dimensional arrays of micro- and nanoparticles using patterned self-assembled monolayers as templates*. Advanced Materials, 1999. **11**(17): p. 1433-1437.
58. Song, G.J., et al., *Preparation of good mechanical property polystyrene nanotubes with array structure in anodic aluminum oxide template using simple physical techniques*. Journal of Materials Research, 2004. **19**(11): p. 3324-3328.
59. Zhang, M.F., et al., *Wetting transition in cylindrical alumina nanopores with polymer melts*. Nano Letters, 2006. **6**(5): p. 1075-1079.
60. Piner, R.D., et al., *"Dip-pen" nanolithography*. Science, 1999. **283**(5402): p. 661-663.
61. Hersee, S.D., X.Y. Sun, and X. Wang, *The controlled growth of GaN nanowires*. Nano Letters, 2006. **6**(8): p. 1808-1811.
62. Bruinink, C.M., et al., *Stamps for submicrometer soft lithography fabricated by capillary force lithography*. Advanced Materials, 2004. **16**(13): p. 1086-+.
63. Helt, J.M., C.M. Drain, and J.D. Batteas, *A benchtop method for the fabrication and patterning of nanoscale structures on polymers*. Journal of the American Chemical Society, 2004. **126**(2): p. 628-634.
64. Li, Q.G., J.B. Olson, and R.M. Penner, *Nanocrystalline alpha-MnO₂ nanowires by electrochemical step-edge decoration*. 2004. **16**(18): p. 3402-3405.
65. Xiao, Y.K., et al., *Electrodeposition of Pd-Ag alloy nanowires on highly oriented pyrolytic graphite*. Journal of Applied Electrochemistry, 2006. **36**(7): p. 807-812.
66. Gelves, G.A., et al., *Multigram synthesis of copper nanowires using ac electrodeposition into porous aluminium oxide templates*. Journal of Materials Chemistry, 2006. **16**(30): p. 3075-3083.
67. Gerein, N.J. and J.A. Haber, *Effect of ac electrodeposition conditions on the growth of high aspect ratio copper nanowires in porous aluminum oxide templates*. Journal of Physical Chemistry B, 2005. **109**(37): p. 17372-17385.

68. Riveros, G., et al., *Silver nanowire arrays electrochemically grown into nanoporous anodic alumina templates*. *Nanotechnology*, 2006. **17**(2): p. 561-570.
69. Bhattacharyya, S., S.K. Saha, and D. Chakravorty, *Silver nanowires grown in the pores of a silica gel*. *Applied Physics Letters*, 2000. **77**(23): p. 3770-3772.
70. Hangarter, C.M. and N.V. Myung, *Magnetic alignment of nanowires*. *Chemistry of Materials*, 2005. **17**(6): p. 1320-1324.
71. Ren, Q., et al., *Biological application of multi-component nanowires in hybrid devices powered by F-1-ATPase motors*. *Biomedical Microdevices*, 2006. **8**(3): p. 201-208.
72. Bao, J.C., et al., *Template synthesis of an array of nickel nanotubules and its magnetic behavior*. *Advanced Materials*, 2001. **13**(21): p. 1631-+.
73. Nielsch, K., et al., *Uniform nickel deposition into ordered alumina pores by pulsed electrodeposition*. *Advanced Materials*, 2000. **12**(8): p. 582-586.
74. Walter, E.C., et al., *Noble and coinage metal nanowires by electrochemical step edge decoration*. *Journal of Physical Chemistry B*, 2002. **106**(44): p. 11407-11411.
75. Gu, Q., et al., *DNA-templated fabrication of nickel nanocluster chains*. *Physica E-Low-Dimensional Systems & Nanostructures*, 2006. **33**(1): p. 92-98.
76. Lee, I.S., P.T. Hammond, and M.F. Rubner, *Selective electroless nickel plating of particle arrays on polyelectrolyte multilayers*. *Chemistry of Materials*, 2003. **15**(24): p. 4583-4589.
77. Parks, G.A., *Isoelectric Points of Solid Oxides Solid Hydroxides and Aqueous Hydroxo Complex Systems*. *Chemical Reviews*, 1965. **65**(2): p. 177-&.
78. Kidambi, S., C. Chan, and I.S. Lee, *Selective depositions on polyelectrolyte multilayers: Self-assembled monolayers of m-dPEG acid as molecular template*. *Journal of the American Chemical Society*, 2004. **126**(14): p. 4697-4703.
79. Kim, H.-J., et al., *Dynamic Sequential Layer-by-Layer Deposition Method for Fast and Region-Selective Multilayer Thin Film Fabrication*. *Langmuir*, 2005. **21**: p. 8532-8538.
80. Shleev, S., et al., *Direct electron transfer between copper-containing proteins and electrodes*. *Biosensors & Bioelectronics*, 2005. **20**(12): p. 2517-2554.

81. Land, E.J., C.A. Ramsden, and P.A. Riley, *Tyrosinase autoactivation and the chemistry of ortho-quinone amines*. Accounts of Chemical Research, 2003. **36**(5): p. 300-308.
82. Seo, S.Y., V.K. Sharma, and N. Sharma, *Mushroom tyrosinase: Recent prospects*. Journal of Agricultural and Food Chemistry, 2003. **51**(10): p. 2837-2853.
83. Duran, N., et al., *Applications of laccases and tyrosinases (phenoloxidases) immobilized on different supports: a review*. Enzyme and Microbial Technology, 2002. **31**(7): p. 907-931.
84. Sanz, V.C., et al., *Development of a tyrosinase biosensor based on gold nanoparticles-modified glassy carbon electrodes - Application to the measurement of a bioelectrochemical polyphenols index in wines*. Analytica Chimica Acta, 2005. **528**(1): p. 1-8.
85. Montereali, M.R., et al., *Tyrosinase biosensor based on modified screen printed electrodes: measurements of total phenol content*. International Journal of Environmental Analytical Chemistry, 2005. **85**(9-11): p. 795-806.
86. Liu, Z.M., et al., *Amperometric tyrosinase biosensor using enzyme-labeled an colloids immobilized on cystamine/chitosan modified gold surface*. Analytical Letters, 2004. **37**(6): p. 1079-1091.
87. Liu, Z.M., et al., *A mediator-free tyrosinase biosensor based on ZnO sol-gel matrix*. Electroanalysis, 2005. **17**(12): p. 1065-1070.
88. Zhang, T., et al., *A sensitive mediator-free tyrosinase biosensor based on an inorganic-organic hybrid titania sol-gel matrix*. Analytica Chimica Acta, 2003. **489**(2): p. 199-206.
89. Serra, B., et al., *Rapid and highly sensitive electrochemical determination of alkaline phosphatase using a composite tyrosinase biosensor*. Analytical Biochemistry, 2005. **336**(2): p. 289-294.
90. Pardo-Yissar, V., et al., *Layered polyelectrolyte films on Au electrodes: Characterization of electron-transfer features at the charged polymer interface and application for selective redox reactions*. Langmuir, 2001. **17**(4): p. 1110-1118.
91. Glynn, P., *Neuropathy target esterase*. Biochemical Journal, 1999. **344**: p. 625-631.
92. Li, Y., D. Dinsdale, and P. Glynn, *Protein domains, catalytic activity, and subcellular distribution of neuropathy target esterase in mammalian cells*. Journal of Biological Chemistry, 2003. **278**(10): p. 8820-8825.

93. Atkins, J. and P. Glynn, *Membrane association of and critical residues in the catalytic domain of human neuropathy target esterase*. Journal of Biological Chemistry, 2000. **275**(32): p. 24477-24483.
94. Kropp, T.J., P. Glynn, and R.J. Richardson, *The mipafox-inhibited catalytic domain of human neuropathy target esterase ages by reversible proton loss*. Biochemistry, 2004. **43**(12): p. 3716-3722.
95. Makhaeva, G.F., et al., *Biosensor detection of neuropathy target esterase in whole blood as a biomarker of exposure to neuropathic organophosphorus compounds*. Journal of Toxicology and Environmental Health-Part A, 2003. **66**(7): p. 599-610.
96. van Tienhoven, M., et al., *Human neuropathy target esterase catalyzes hydrolysis of membrane lipids*. Journal of Biological Chemistry, 2002. **277**(23): p. 20942-20948.
97. Forshaw, P.J., et al., *The catalytic domain of human neuropathy target esterase mediates an organophosphate-sensitive ionic conductance across liposome membranes*. Journal of Neurochemistry, 2001. **79**(2): p. 400-406.
98. Kayyali, U.S., et al., *Neurotoxic Esterase (Nte) Assay - Optimized Conditions Based on Detergent-Induced Shifts in the Phenol/4-Aminoantipyrine Chromophore Spectrum*. Journal of Analytical Toxicology, 1991. **15**(2): p. 86-89.
99. Sigolaeva, L.V., et al., *Bioelectrochemical analysis of neuropathy target esterase activity in blood*. Analytical Biochemistry, 2001. **290**(1): p. 1-9.
100. Sokolovskaya, L.G., et al., *Improved electrochemical analysis of neuropathy target esterase activity by a tyrosinase carbon paste electrode modified by 1-methoxyphenazine methosulfate*. Biotechnology Letters, 2005. **27**(16): p. 1211-1218.
101. Coche-Guerente, L., P. Labbe, and V. Mengeaud, *Amplification of amperometric biosensor responses by electrochemical substrate recycling. 3. Theoretical and experimental study of the phenol-polyphenol oxidase system immobilized in Laponite hydrogels and layer-by-layer self-assembled structures*. Analytical Chemistry, 2001. **73**(14): p. 3206-3218.
102. Forzani, E.S., V.M. Solis, and E.J. Calvo, *Electrochemical behavior of polyphenol oxidase immobilized in self-assembled structures layer by layer with cationic polyallylamine*. Analytical Chemistry, 2000. **72**(21): p. 5300-5307.
103. Kohli, N., *Polyelectrolytes Based Biomimetic Interfaces for Bioelectronic Applications*. Chemical Engineering, Michigan State University, 2007: PhD Thesis.

104. Lassalle, V. and M.L. Ferreira, *PLA nano- and microparticles for drug delivery: An overview of the methods of preparation*. *Macromolecular Bioscience*, 2007. **7**(6): p. 767-783.
105. Allen, T.M. and P.R. Cullis, *Drug delivery systems: Entering the mainstream*. *Science*, 2004. **303**(5665): p. 1818-1822.
106. Jilek, S., H.P. Merkle, and E. Walter, *DNA-loaded biodegradable microparticles as vaccine delivery systems and their interaction with dendritic cells*. *Advanced Drug Delivery Reviews*, 2005. **57**(3): p. 377-390.
107. Guinebretiere, S., et al., *Study of the emulsion-diffusion of solvent: Preparation and characterization of nanocapsules*. *Drug Development Research*, 2002. **57**(1): p. 18-33.
108. Choi, S.H. and T.G. Park, *G-CSF loaded biodegradable PLGA nanoparticles prepared by a single oil-in-water emulsion method*. *International Journal of Pharmaceutics*, 2006. **311**(1-2): p. 223-228.
109. Zavisova, V., et al., *Encapsulation of indomethacin in magnetic biodegradable polymer nanoparticles*. *Journal of Magnetism and Magnetic Materials*, 2007. **311**(1): p. 379-382.
110. Galindo-Rodriguez, S., et al., *Physicochemical parameters associated with nanoparticle formation in the salting-out, emulsification-diffusion, and nanoprecipitation methods*. *Pharmaceutical Research*, 2004. **21**(8): p. 1428-1439.
111. Desgouilles, S., et al., *The design of nanoparticles obtained by solvent evaporation: A comprehensive study*. *Langmuir*, 2003. **19**(22): p. 9504-9510.
112. Fessi, H., et al., *Nanocapsule Formation by Interfacial Polymer Deposition Following Solvent Displacement*. *International Journal of Pharmaceutics*, 1989. **55**(1): p. R1-R4.
113. Lathrop, D.P., J. Fineberg, and H.L. Swinney, *Transition to Shear-Driven Turbulence in Couette-Taylor Flow*. *Physical Review A*, 1992. **46**(10): p. 6390-6405.
114. Hinze, J.O., *Fundamentals of the Hydrodynamic Mechanism of Splitting in Dispersion Processes*. *Aiche Journal*, 1955. **1**(3): p. 289-295.
115. Kolmogorov, A.N., *On the breaking of drops in turbulent flow*. *Doklady Akademii Nauk, URSS*, 1949. **66**(5): p. 825-828.
116. Tcholakova, S., et al., *Emulsification in turbulent flow: 3. Daughter drop-size distribution*. *Journal of Colloid and Interface Science*, 2007. **310**(2): p. 570-589.

117. Vankova, N., et al., *Emulsification in turbulent flow 1. Mean and maximum drop diameters in inertial and viscous regimes*. Journal of Colloid and Interface Science, 2007. **312**(2): p. 363-380.
118. Vankova, N., et al., *Emulsification in turbulent flow 2. Breakage rate constants*. Journal of Colloid and Interface Science, 2007. **313**(2): p. 612-629.
119. Lathrop, D.P., J. Fineberg, and H.L. Swinney, *Turbulent-Flow between Concentric Rotating Cylinders at Large Reynolds-Number*. Physical Review Letters, 1992. **68**(10): p. 1515-1518.
120. Supriya, L. and R.O. Claus, *Solution-based assembly of conductive gold film on flexible polymer substrates*. Langmuir, 2004. **20**(20): p. 8870-8876.
121. Weisbecker, C.S., M.V. Merritt, and G.M. Whitesides, *Molecular self-assembly of aliphatic thiols on gold colloids*. Langmuir, 1996. **12**(16): p. 3763-3772.
122. Chapman, D.L., *A contribution to the theory of electrocapillarity*. Philos. Mag, 1913. **25**: p. 475.
123. Guoy, G., *Constitution of the Electric Charge at the Surface of an Electrolyte*. J. Phys. Theor. Appl. , 1910. **9**(4): p. 455-468.
124. Girifalco, L.A. and R.J. Good, *A Theory for the Estimation of Surface and Interfacial Energies .1. Derivation and Application to Interfacial Tension*. Journal of Physical Chemistry, 1957. **61**(7): p. 904-909.
125. Khossravi, D. and K.A. Connors, *Solvent Effects on Chemical Processes .3. Surface-Tension of Binary Aqueous Organic-Solvents*. Journal of Solution Chemistry, 1993. **22**(4): p. 321-330.
126. Cheng, N.S., *Formula for the viscosity of a glycerol-water mixture*. Industrial & Engineering Chemistry Research, 2008. **47**(9): p. 3285-3288.
127. Im, S.H., U.Y. Jeong, and Y.N. Xia, *Polymer hollow particles with controllable holes in their surfaces*. Nature Materials, 2005. **4**(9): p. 671-675.
128. Garlotta, D., *A literature review of poly(lactic acid)*. Journal of Polymers and the Environment, 2001. **9**(2): p. 63-84.
129. Loo, S.C.J., C.P. Ooi, and Y.C.F. Boey, *Radiation effects on poly(lactide-co-glycolide) (PLGA) and poly(L-lactide) (PLLA)*. Polymer Degradation and Stability, 2004. **83**(2): p. 259-265.

MICHIGAN STATE UNIVERSITY LIBRARIES



3 1293 03062 4195